②

NAVAL POSTGRADUATE SCHOOL
Monterey, California

THESIS

COMPUTATIONAL INVESTIGATION OF
INCOMPRESSIBLE AIRFOIL FLOWS
AT HIGH ANGLES OF ATTACK

by

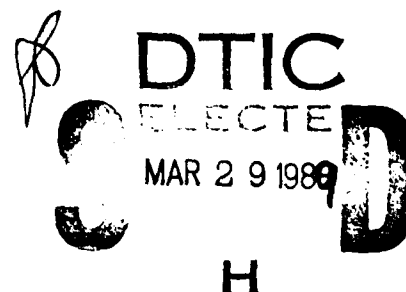John Mark Mathre

December 1988

Thesis Advisor: M. F. Platzer

DTIC
ELECTE
MAR 2 9 1989
S   D
H

89 3 28 040

REPORT DOCUMENTATION PAGE

1a REPORT SECURITY CLASSIFICATION	1b RESTRICTIVE MARKINGS
Unclassified	

2a. SECURITY CLASSIFICATION AUTHORITY	3 DISTRIBUTION/AVAILABILITY OF REPORT
	Approved for public release; distribution is unlimited
2b. DECLASSIFICATION/DOWNGRADING SCHEDULE	

4. PERFORMING ORGANIZATION REPORT NUMBER(S)	5 MONITORING ORGANIZATION REPORT NUMBER(S)

6a NAME OF PERFORMING ORGANIZATION	6b OFFICE SYMBOL (If applicable)	7a NAME OF MONITORING ORGANIZATION
Naval Postgraduate School	Code 67	Naval Postgraduate School

6c. ADDRESS (City, State, and ZIP Code)	7b. ADDRESS (City, State, and ZIP Code)
Monterey, California 93943-5000	Monterey, California 93943-5000

8a. NAME OF FUNDING/SPONSORING ORGANIZATION	8b OFFICE SYMBOL (If applicable)	9 PROCUREMENT INSTRUMENT IDENTIFICATION NUMBER

8c. ADDRESS (City, State, and ZIP Code)	10 SOURCE OF FUNDING NUMBERS			
	PROGRAM ELEMENT NO	PROJECT NO	TASK NO	WORK UNIT ACCESSION NO

11. TITLE (Include Security Classification)
Computational Investigation of Incompressible Airfoil Flows at High Angles of Attack

12 PERSONAL AUTHOR(S)
Mathre, John M.

13a TYPE OF REPORT	13b TIME COVERED	14. DATE OF REPORT (Year, Month, Day)	15 PAGE COUNT
Master's Thesis	FROM _____ TO _____	December, 1988	158

16 SUPPLEMENTARY NOTATION The views expressed in this thesis are those of the author and do not reflect the official policy or position of the Department of Defense or the U. S. Government.

17. COSATI CODES			18 SUBJECT TERMS (Continue on reverse if necessary and identify by block number)
FIELD	GROUP	SUB-GROUP	Computational Analysis of Inviscid, Viscous and Interaction Schemes.

19. ABSTRACT (Continue on reverse if necessary and identify by block number) Cebeci's viscous/inviscid interaction program was applied to the analysis of steady, two dimensional, incompressible flow past four airfoils, the NACA 66_3-018, 0010 (Modified), 4412 and the Wortmann FX 63-137. Detailed comparisons with the available experimental results show that the essential features are correctly modelled, but that significant discrepancies are found in regions of flow separations.

20 DISTRIBUTION/AVAILABILITY OF ABSTRACT	21 ABSTRACT SECURITY CLASSIFICATION
☒ UNCLASSIFIED/UNLIMITED ☐ SAME AS RPT ☐ DTIC USERS	Unclassified

22a NAME OF RESPONSIBLE INDIVIDUAL	22b TELEPHONE (Include Area Code)	22c OFFICE SYMBOL
Max F. Platzer	(408) 646-2944	Code 67PL

DD FORM 1473, 84 MAR | 83 APR edition may be used until exhausted. All other editions are obsolete | SECURITY CLASSIFICATION OF THIS PAGE

☆ U.S. Government Printing Office 1986—606-243

Approved for public distribution; distribution is unlimited.

Computational Investigation of
Incompressible Airfoil Flows
at High Angles of Attack

by

John Mark Mathre
Lieutenant, United States Navy
B.S., United States Naval Academy, 1978

Submitted in partial fulfillment of the
requirements for the degree of

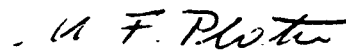MASTER OF SCIENCE IN AERONAUTICAL ENGINEERING

from the

NAVAL POSTGRADUATE SCHOOL
December 1988

Author: _____
John Mark Mathre

Approved by: _____
M. F. Platzer, Thesis Advisor

_____
R. M. Howard, Second Reader

_____
E. Roberts Wood, Chairman
Department of Aeronautics and Astronautics

_____
Gordon E. Schacher
Dean of Science and Engineering

ii

ABSTRACT

Cebeci's viscous/inviscid interaction program was applied to the analysis of steady, two dimensional, incompressible flow past four airfoils, the NACA 66_3-018, 0010 (Modified), 4412 and the Wortmann FX 63-137. Detailed comparisons with the available experimental results show that the essential features are correctly modelled, but that significant discrepancies are found in regions of flow separations.

TABLE OF CONTENTS

LIST OF TABLES

LIST OF FIGURES

TABLE OF SYMBOLS

FLR	Finite difference "on-off switch"
GY_{TR}	Empirical constant for transition
h	Box height
K	Iterations counter
m	Mass
n	Normal to surface
P	Local static pressure
R	Reynolds number based on chord
R_θ	Reynolds number based on momentum thickness
S	Surface area
u	Velocity in x direction
U_e	Velocity at edge of boundary layer
v	Velocity component in y direction
Y_{tr}	Intermittancy factor for transition
δ	Boundary layer thickness, $u = .99U_e$
$\delta*$	Displacement thickness
η	Y transformation
Θ	Momentum thickness
μ	Viscosity
ν	Kinematic viscosity
ν_t	Eddy viscosity
ρ	Density
σ	Stress
τ	Shear stress

τ_w	Wall (body) shear stress
$\emptyset$	Velocity potential
ψ	Stream function
Ω	Relaxation parameter

ACKNOWLEDGEMENTS

I. INTRODUCTION

Understanding of the characteristics of the airflow over an airfoil is of paramount importance to the airfoil designer. Two methods are currently available which give accurate results. The first is the use of wind tunnel tests. The drawbacks to this method are cost and time consumption. The second is the processing of the Navier-Stokes equations. This method's drawbacks are the requirements and expense of using supercomputers due to the extensive calculations and storage requirements. There is still a need to come up with an inexpensive, fast and accurate engineering tool to compute airfoil flows.

Several methods have been derived to accomplish this end. But the most promising is the Viscous-Inviscid Interaction method. The outer flow is computed using inviscid flow equations, and the inner flow is computed using Prandtl's boundary layer equations. The key to this method is the extent of interaction between the inner and outer flows.

The purpose of this thesis is to evaluate the capability of the viscous-inviscid interactive aircode developed by Tuncer Cebeci and associates at the Douglas Aircraft Company [Ref. 1]. This computer program was applied to four airfoils with various angles of attack and Reynolds numbers. The computer results were then compared to previously reported experimental results.

1

The conservation of mass and momentum are summarized in Chapter 2, inviscid flow calculations are discussed in Chapter 3, and viscous flow equations are described in Chapter 4. Viscous calculations are presented in Chapter 5, and the specific interaction methods are shown in Chapter 6. Finally, in Chapter 7 computer and experimental results are compared for the NACA 66_3-018, 0010 (Modified) and 4412 airfoils as well as the Wortmann FX 63-137 airfoil.

II. FUNDAMENTAL EQUATIONS

The conservation of mass and conservation of momentum provide the foundation for incompressible flow analysis. With these fundamental concepts along with appropriate assumptions and approximations, working relations for two-dimensional, incompressible flow are obtained.

A. CONSERVATION OF MASS (CONTINUITY)

The conservation of mass principle states that mass cannot be created nor destroyed. Equating this statement to a fixed control volume the net mass flow rate into and out of the control volume equals the time rate of change of mass within the control volume [Ref. 2:p. A-1].

Given a control volume, the mass flow rate through one of its surfaces is equal to the product of the fluid density, the fluid velocity normal to the surface and the area of the surface [Ref. 3:p. 29].

$$\frac{d \text{ mass}}{dt} = V \cdot n \, s \tag{2.1}$$

In 2-D flow the x-component of the mass flow rate at the center of the positive x-face, position dx/2 and side length dy, is represented by Taylor series expansion [Ref. 2:p. A-2]

3

$$\left[\rho u + \frac{\partial}{\partial x}(\rho u)\frac{dx}{2} + \frac{\partial^2}{\partial x^2}(\rho u)(\frac{dx}{2})^2 \frac{1}{2!} + \ldots \right] dy. \qquad (2.2)$$

As dx approaches zero all higher order terms disappear leaving

$$\left[\rho u + \frac{\partial}{\partial x}(\rho u)\frac{dx}{2} \right] dy. \qquad (2.3)$$

Similarly, the x-component of the mass flow rate at the center of the negative x-face, position -dx/2 and side length dy, is represented by

$$\left[\rho u - \frac{\partial}{\partial x}(\rho u)\frac{dx}{2} \right] dy. \qquad (2.4)$$

As illustrated in Figure 2.1 the net mass flow through the four sides of the 2-D control surface is

$$\left[\rho u - \frac{\partial}{\partial x}(\rho u)\frac{dx}{2} \right] dy - \left[\rho u + \frac{\partial}{\partial x}(\rho u)\frac{dx}{2} \right] dy$$

$$+ \left[\rho v - \frac{\partial}{\partial y}(\rho v)\frac{dy}{2} \right] dx - \left[\rho v + \frac{\partial}{\partial y}(\rho v)\frac{dy}{2} \right] dx \qquad (2.5)$$

$$\rho v + \frac{\partial}{\partial y}(\rho v)\frac{dy}{2}$$

$$y$$

$$x$$

$$\rho u - \frac{\partial}{\partial x}(\rho u)\frac{dx}{2}$$

dy   +

$$\rho u + \frac{\partial}{\partial x}(\rho u)\frac{dx}{2}$$

dx

$$\rho v - \frac{\partial}{\partial y}(\rho v)\frac{dy}{2}$$
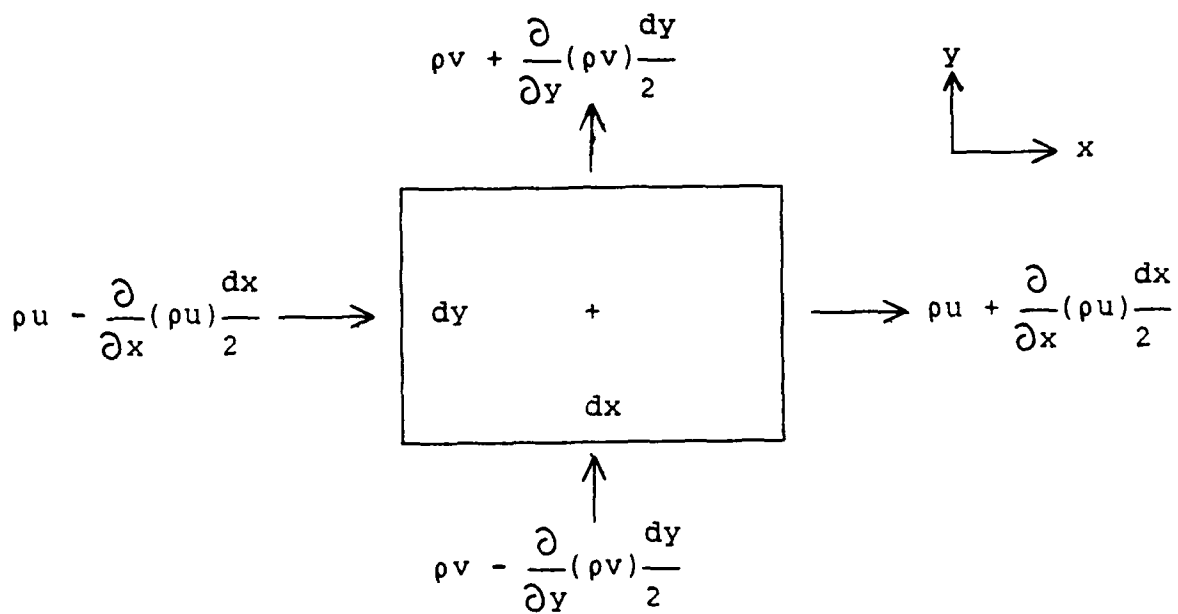
Figure 2.1   Mass Flow Through 2-D Control Surface
[Ref. 4:p. 12]

which is equal to the rate of change of the mass within the control volume

$$\frac{\partial \rho}{\partial t} \, dxdy \qquad (2.6)$$

Combining (2.5) with (2.6) and simplifying yields

$$-\frac{\partial}{\partial x}(\rho u)dxdy - \frac{\partial}{\partial y}(\rho u)dxdy = \frac{\partial \rho}{\partial x} \, dxdy \qquad (2.7)$$

Dividing by dxdy and rearranging yields

$$\frac{\partial \rho}{\partial t} + \frac{\partial}{\partial x}(\rho u) + \frac{\partial}{\partial y}(\rho u) = 0 \qquad (2.8)$$

For steady, incompressible flows the continuity equation becomes

$$\frac{\partial u}{\partial x} + \frac{\partial v}{\partial y} = 0 \qquad (2.9)$$

or in vector form the continuity equation [Ref. 3:p. 30] is

$$\nabla \cdot \mathbf{V} = 0 \qquad (2.10)$$

B. CONSERVATION OF MOMENTUM (NAVIER-STOKES)

The conservation of momentum, Newton's second law of motion, states that the rate of change of the linear momentum is equal to the sum of the forces applied [Ref. 2:p. B-1].

$$\Sigma F = \frac{d}{dx}(mV) \qquad (2.11)$$

As illustrated in Figure 2.2 the two significant forces which act on an element of fluid are surface forces which act on the surface only, pressure and shear, and body forces which affect the mass of the element, such as gravity. Assuming moment equilibrium in an element, $\tau_{xy} = \tau_{yx}$, the 2-D first order Taylor series expansion for normal and shear surface forces in the x-direction is

$$\left[\tau_{xx} + \frac{\partial}{\partial x}(\tau_{xx})\frac{dx}{2} - \tau_{xx} + \frac{\partial}{\partial x}(\tau_{xx})\frac{dx}{2} \right] dy$$

$$+ \left[\tau_{xy} + \frac{\partial}{\partial y}(\tau_{xy})\frac{dy}{2} - \tau_{xy} + \frac{\partial}{\partial y}(\tau_{xy})\frac{dy}{2} \right] dx$$

$$= \frac{\partial}{\partial x}(\tau_{xx})dxdy + \frac{\partial}{\partial y}(\tau_{xy})dxdy. \qquad (2.12)$$

The body forces per unit mass are represented by

$$F_{BODY} = Xi + Yj + Zk \qquad (2.13)$$

such that the x-component of the body force on an element is

$$f_{x(BODY)} = \rho dxdy \cdot 1 \cdot X. \qquad (2.14)$$

Combining equations (2.12) and (2.14) the sum of the forces in the x-direction is

7

$$\tau_{yy} + \frac{\partial}{\partial y}(\tau_{yy})\frac{dy}{2}$$

$$\tau_{yx} + \frac{\partial}{\partial y}(\tau_{yx})\frac{dy}{2}$$

$$\tau_{xx} - \frac{\partial}{\partial x}(\tau_{xx})\frac{dx}{2}$$

$$\tau_{xy} + \frac{\partial}{\partial x}(\tau_{xy})\frac{dx}{2}$$

$$\tau_{xy} - \frac{\partial}{\partial x}(\tau_{xy})\frac{dx}{2}$$

$$\tau_{xx} + \frac{\partial}{\partial x}(\tau_{xx})\frac{dx}{2}$$

$$\tau_{yx} - \frac{\partial}{\partial y}(\tau_{yx})\frac{dy}{2}$$

$$\tau_{yy} - \frac{\partial}{\partial y}(\tau_{yy})\frac{dy}{2}$$
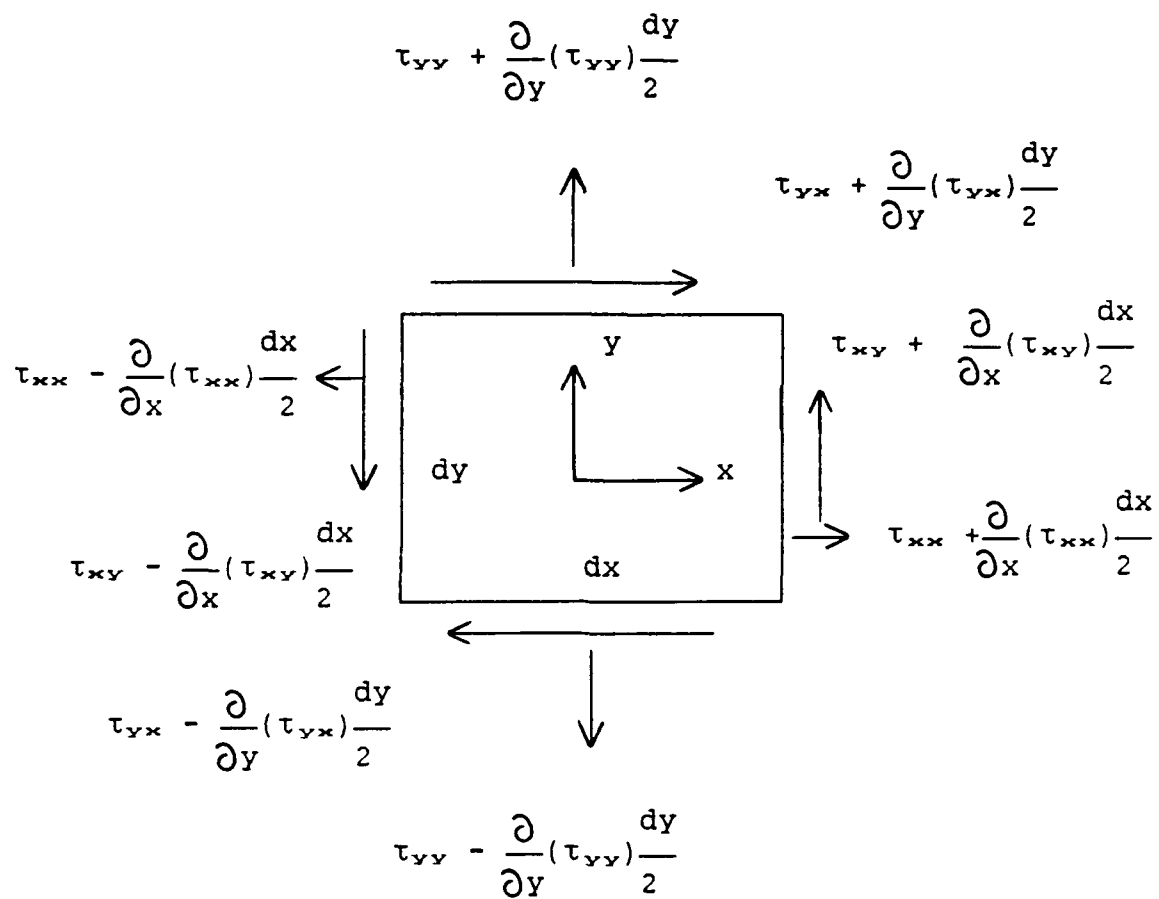
Figure 2.2   Stresses on a 2-D Control Surface
[Ref. 4:p. 15]

$$\Sigma F_x = \left[\rho X + \frac{\partial}{\partial x}(\tau_{xx}) + \frac{\partial}{\partial y}(\tau_{xy}) \right] dxdy. \qquad (2.15)$$

The rate of change of the linear momentum in the x-direction assuming constant mass is mdu/dt.

As $\dfrac{du}{dt} = \dfrac{\partial u}{\partial x}\dfrac{dx}{dt} + \dfrac{\partial u}{\partial y}\dfrac{dy}{dt} + \dfrac{\partial u}{\partial t}$ via the chain rule, and $\dfrac{\partial x}{\partial t} = u,$

and $\dfrac{\partial y}{\partial t} = v$ the x-direction change in linear momentum for

particle is

$$m\frac{du}{dt} = \rho dxdy \left(v\frac{\partial u}{\partial x} + v\frac{\partial u}{\partial y} + \frac{\partial u}{\partial t} \right). \qquad (2.16)$$

Substituting equations (2.15) and (2.16) into the x-component of equation (2.11) yields

$$\rho dxdy \left(u\frac{\partial u}{\partial x} + v\frac{\partial u}{\partial y} + \frac{\partial u}{\partial t} \right) = \left[\rho X + \frac{\partial}{\partial x}(\tau_{xx}) + \frac{\partial}{\partial y}(\tau_{xy}) \right] dxdy. (2.17)$$

Now, in order to have the entire equation as a function of velocity the normal and shear stresses must be found in terms of velocity.

By assuming a Newtonian fluid [Ref. 2:p. B-5] the shear stress is linearly related to the rate of angular deformation with fluid viscosity being the proportionality constant.

9

$$\tau_{xy} = \mu\left(\frac{\partial u}{\partial y} + \frac{\partial v}{\partial x}\right) \qquad (2.18)$$

The normal stresses are equal, but opposite in direction to the pressure when no shear stresses are involved. With shear stress from viscosity it is assumed that the normal stresses deviate from -P and that the deviation is proportional to both a) the rate of linear strain in the direction concerned, and b) the rate of volume deformation. Therefore, the normal stress in the x-direction [Ref. 1:p. B-10] is

$$\tau_{xx} = -P + 2\mu\left(\frac{\partial u}{\partial x}\right) - \frac{2}{3}\mu\left(\frac{\partial u}{\partial x} + \frac{\partial v}{\partial y}\right). \qquad (2.19)$$

Applying the conservation of mass, equation (2.9), equation (2.19) simplifies to

$$\tau_{xx} = -P + 2\mu\left(\frac{\partial u}{\partial x}\right). \qquad (2.20)$$

Substituting equations (2.18) and (2.20) into (2.17) and dividing by dxdy yields

$$\rho\left(u\frac{\partial u}{\partial x} + v\frac{\partial u}{\partial y} + \frac{\partial u}{\partial t}\right) = \rho X + \frac{\partial}{\partial x}\left(-P + 2\mu\left(\frac{\partial u}{\partial x}\right)\right) + \mu\frac{\partial}{\partial y}\left(\frac{\partial u}{\partial y} + \frac{\partial v}{\partial x}\right) \qquad (2.21)$$

After multiplying and rearranging the right hand side becomes

$$\rho X - \frac{\partial P}{\partial x} + 2\mu\frac{\partial^2 u}{\partial x^2} + \mu\frac{\partial^2 u}{\partial y^2} + \mu\frac{\partial^2 v}{\partial y \partial x}$$

which is also equal to

$$\rho X - \frac{\partial P}{\partial x} + \mu\frac{\partial^2 u}{\partial x^2} + \mu\frac{\partial^2 u}{\partial y^2} + \mu\frac{\partial}{\partial x}(\frac{\partial u}{\partial x} + \frac{\partial v}{\partial y})$$

Again applying the conservation of mass, equation (2.9), equation (2.21) becomes

$$\rho(u\frac{\partial u}{\partial x} + v\frac{\partial u}{\partial y} + \frac{\partial u}{\partial t}) = \rho X - \frac{\partial P}{\partial x} + \mu(\frac{\partial^2 u}{\partial x^2} + \frac{\partial^2 u}{\partial y^2}). \qquad (2.22)$$

With $\nu = \mu/\rho$ = kinematic viscosity and neglecting the body force, X, the two dimensional Navier-Stokes, conservation of momentum equation for incompressible and constant viscosity flow in the x-direction [Ref. 2:p. 436] is

$$\frac{\partial u}{\partial t} + u\frac{\partial u}{\partial x} + v\frac{\partial u}{\partial y} = -\frac{1}{\rho}\frac{\partial P}{\partial x} + \nu(\frac{\partial^2 u}{\partial x^2} + \frac{\partial^2 u}{\partial y^2}). \qquad (2.23)$$

Similarly, in the y-direction the Navier-Stokes equation is

$$\frac{\partial v}{\partial t} + u\frac{\partial v}{\partial x} + v\frac{\partial v}{\partial y} = -\frac{1}{\rho}\frac{\partial P}{\partial y} + \nu(\frac{\partial^2 v}{\partial x^2} + \frac{\partial^2 v}{\partial y^2}). \qquad (2.24)$$

III. STEADY INVISCID FLOW

Although real fluids are viscous the major effects of viscosity are concentrated in a region, or layer adjacent to a body. Therefore, analyses of inviscid flow are useful and serve as a good approximation to flow outside the boundary layer and wake behind the body.

The justification for applying the results of perfect fluid analyses to viscous flows was postulated by Ludwig Prandtl in 1904 [Ref. 3:p. 299]. He stated that the effects of viscosity on the flow around streamlined bodies at high Reynolds numbers are effectively limited to a "thin" boundary layer. The characteristic length to judge thinness is the distance from the forward stagnation point to the point of consideration.

A. VELOCITY POTENTIAL

For flow outside the boundary layer it is a great advantage to simplify equations and develop a single governing equation. With the assumptions of steady flow, no energy transfer to or from the fluid, no body forces, no shear stress (inviscid), and irrotational flow the velocity potential, ϕ, is utilized [Ref. 3:p. 48]. ϕ, a scalar function of spatial coordinates, x and y, is defined such that

$$V = \nabla\phi \qquad\qquad (3.1)$$

12

and

$$u = \frac{\partial \phi}{\partial x} \qquad v = \frac{\partial \phi}{\partial y} \qquad (3.2)$$

The importance of the velocity potential is that only one equation is needed to describe the irrotational flow. Velocity components are obtained using equation (3.2).

B. LAPLACE EQUATION

For steady, incompressible flows the continuity equation (2.9) is

$$\frac{\partial u}{\partial x} + \frac{\partial v}{\partial y} = 0$$

Rewriting (2.9) in terms of the velocity potential the equation becomes

$$\frac{\partial^2 \phi}{\partial x^2} + \frac{\partial^2 \phi}{\partial y^2} = 0 \qquad (3.3)$$

This form of the Laplace equation [Ref. 2:p. 81] is the governing equation for steady, irrotational flow of an incompressible fluid.

The importance of equation (3.3) is that it is linear allowing for the principle of superposition. For example if ϕ_1, ϕ_2, ϕ_3...are solutions of (3.3), then the sum $\phi = \phi_1 + \phi_2 + \phi_3 +$...is also a solution of (3.3). Superposition of irrotational, incompressible flows allow for the construction

13

of complex flows that are also irrotational and incompressible.

C. SIMULATION (CONFORMAL MAPPING)

The inviscid flow about an airfoil can be obtained most conveniently by means of a transformation, which starts with a known flow about a simple contour, a circle, distorts the contour into the desired shape, and simultaneously adapts the flow to that shape. The transformation is accomplished using a sequence of three conformal mappings [Ref. 1:p. 324].

The first mapping, necessary only when the airfoil trailing edge has non-zero thickness, is accomplished using a logarithmic mapping function. The airfoil is perturbed slightly to make the upper and lower surface, trailing-edge points coincide.

The second mapping analytically removes the trailing-edge corner using the Karman-Trefftz mapping.

The third and final mapping transforms a quasi-circular shape into a perfect circle using an iterated sequence of Fast-Fourier Transform applications.

During the transformation of streamlines about a circle to those about an airfoil, the preferable approach insuring a transformed flow free from vorticity uses the complex variable $z = x + iy$ [Ref. 5:p. 285]. The transformation of z to another plane is $\xi = f(z) = \xi + i\eta$. The potential function, $Q = \phi + i\psi$, is irrotational and incompressible in both planes.

The streamlines, ψ, and equipotential lines, ϕ, of a flow in the z-plane will transform into another orthogonal network of lines in the ζ-plane. Different magnification ratios and different amounts of rotation at different points in the field will, however, change the appearance of the flow pattern from about a circle to about the airfoil.

The general transformation function whose derivative $d\zeta/dz$ satisfies the requirement $d\zeta/dz$ approaches unity for large values of z is

$$\zeta = z + C_o \ln z + C_1/z + C_2/z^2 + \ldots \quad . \qquad (3.4)$$

The requirement is necessary as streamlines are not distorted a great distance from the body where the body's shape has no influence on the flow.

The coefficients may be real, imaginary or complex. A finite number of the coefficients are determined from the specified normal velocity components equally spaced around the unit circle, and from the Kutta condition which ensures stagnation at the trailing edge.

While in the first iteration the normal velocities are zero, and the solution for flow over a circle is used, the subsequent normal velocity boundary conditions are determined from the previous viscous-flow calculations using the equation

15

$$V_n = \frac{d}{ds}(u_e\delta^*) \tag{3.5}$$

where u_e is the velocity at the edge of the boundary layer and δ^* is the displacement thickness. Once the coefficients are found, the real and imaginary parts of equation (3.4) are equated yielding

$$\xi = \xi(x,y) \text{ and } \eta = \eta(x,y).$$

As $x^2 + y^2 = r^2$ the two equations of ξ and η are transformed to

$$x = x(\xi,r^2) \text{ and } y = y(\eta,r^2).$$

Then x^2 and y^2 are added to yield

$$x^2 + y^2 = r^2 = \left[x(\xi,r^2)\right]^2 + \left[y(\eta,r^2)\right]^2. \tag{3.6}$$

After dividing both sides by r^2

$$1 = \frac{1}{r^2}\left[x(\xi,r^2)\right]^2 + \frac{1}{r^2}\left[y(\eta,r^2)\right]^2. \tag{3.7}$$

Then each circle of radius, r, in the z-plane is transformed to the proper shape in the ζ-plane to describe inviscid flow.

1. **Transformation of Velocities [Ref. 5:p. 291]**

In the z-plane as $Q(z) = \phi(x,y) + i\psi(x,y)$ the velocities are defined by

$$\frac{dQ(z)}{dz} = V_x - iV_y \tag{3.8}$$

where,

$$V = V_x + iV_y.$$

In the ζ-plane the velocities are also found

$$\frac{dQ}{d\zeta} = V_\xi - iV_\eta \tag{3.9}$$

where,

$$V_\zeta = V_\xi + iV_\eta.$$

The velocities in the two planes are equated by

$$V_\xi - iV_\eta = \frac{dQ}{dz} \cdot \frac{dz}{d\zeta} = \frac{V_x - iV_y}{d\zeta/dz}. \tag{3.10}$$

The pressure in the transformed stream is related to the stream velocity through Kelvin's equation

$$\frac{1}{2}\rho \left|V_\zeta\right|^2 + P = \text{Constant} = \frac{1}{2}\rho \left|V_\zeta\right|^2_1 + P_1. \tag{3.11}$$

17

IV. VISCOUS FLOW

A. DERIVATION OF BOUNDARY LAYER EQUATIONS

The previous analyses provide a valid solution to the flow outside the boundary layer. Within the boundary layer however, the effects of viscosity cannot be neglected. In laminar flow governing equations can be obtained by simplifying the conservation equations. In turbulent flow, however, the number of variables outnumbers the equations. Great dependence is then placed on dimensional reasoning and on hypotheses suggested by experimental results.

The most important deduction from Prandtl's thin boundary layer theory is that static pressure can be considered constant across the boundary layer [Ref. 3:p. 299].

$$\frac{\partial p}{\partial y} = 0 \qquad (4.1)$$

As the boundary layer thickness, δ, is small, $d\delta/dx$ is also small. Streamlines are then only slightly curved and the radii of curvature, R, are large. With a large R the equilibrium condition

$$\frac{\partial p}{\partial y} = \rho \frac{u^2}{R}$$

18

illustrates that $\partial p/\partial y$ will be very small and can be neglected. Experimental results confirm that $\partial p/\partial y$ may be neglected even over surfaces of small radii of curvature.

Also, in a thin boundary layer with a slowly changing thickness $\partial v/\partial x$ is much smaller than $\partial u/\partial y$. The significance is then that the normal shear stress may be neglected when compared with the viscous shearing stress. Equation (2.18) then becomes

$$\tau_{xy} = \mu\frac{\partial u}{\partial y}. \tag{4.2}$$

With this simplification the approximate equation for flow in the two-dimensional boundary layer can be found directly. Newton's second law of motion applied to a fluid element of mass may be written

$$\rho dxdy(\frac{\partial u}{\partial t} + u\frac{\partial u}{\partial x} + v\frac{\partial u}{\partial y}) = (-\frac{\partial p}{\partial x} + \frac{\partial \tau_{yx}}{\partial y})dxdy \tag{4.3}$$

as illustrated in Figure 4.1. Substituting equation (4.2) and dividing both sides by dxdy yields

$$\rho(\frac{\partial u}{\partial t} + u\frac{\partial u}{\partial x} + v\frac{\partial u}{\partial y}) = (-\frac{\partial p}{\partial x} + \frac{\partial}{\partial y}(\mu\frac{\partial u}{\partial y}). \tag{4.4}$$

In terms of kinematic viscosity equation (4.4) becomes

$$\frac{\partial u}{\partial t} + u\frac{\partial u}{\partial x} + v\frac{\partial u}{\partial y} = -\frac{1}{\rho}\frac{\partial p}{\partial x} + v\frac{\partial^2 u}{\partial y^2}. \tag{4.5}$$

19

$$(\sigma_{yx} + \frac{\sigma_{yx}}{Y} dy)dx$$

u

Pdy

dy

dx

$$(P + \frac{p}{x} dx)dy$$

$$\sigma_{yx}dx$$

y

x
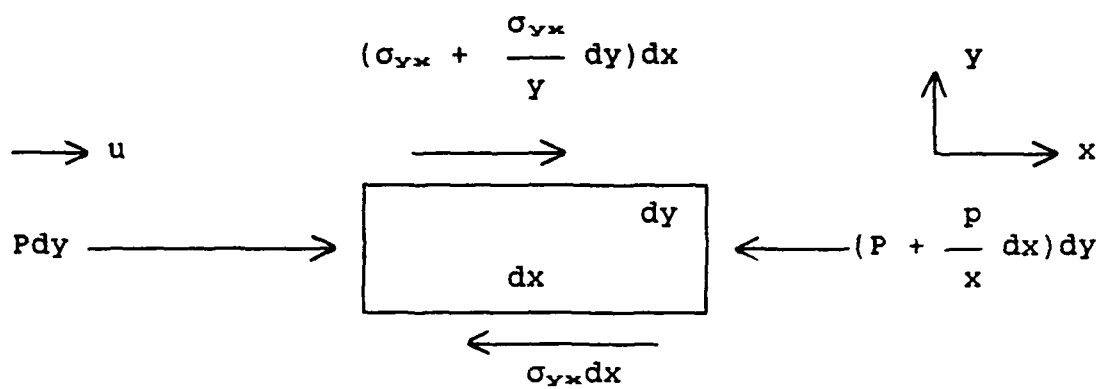
Figure 4.1   Forces Acting on an Element in the Boundary Layer

This equation is the boundary layer equation of motion and is identical to the equation found using an order-of-magnitude analysis [Ref. 3:p. 443]. Equation (4.5) is also nearly identical to the Navier-Stokes equation (2.23) with the exception that the term $\nu \partial^2 u / \partial x^2$ is deleted. The order-of-magnitude analysis suggests that this term, $\nu \partial^2 u / \partial x^2$, may be neglected compared to $\nu \partial^2 u / \partial y^2$. Combined with the continuity equation $\partial u / \partial x + \partial v / \partial y = 0$ (2.9), equations (4.5) and (4.1) are known as Prandtl's boundary layer equations [Ref. 2:p. P-9].

For an incompressible flow, there are three variables, u, v and p, but only two equations, (4.5) and (2.9). The equations may be solved though, by first determining p as a function of x using inviscid methods, setting $\partial p / \partial y = 0$ in the boundary layer, and then solving (4.5) and (2.9) for the velocity distributions.

B. TURBULENT FLOW

Turbulent flow as differentiated from laminar flow is characterized by fluctuating instantaneous properties which greatly increase the complexity of the problem. A very useful simplification to the turbulent problem is then the use of time-averaged values, denoted by a bar over the value. Instantaneous values are indicated by the prime [Ref. 4:p. 23].

$$u = \overline{u} + u'$$

$$v = \overline{v} + v'$$

$$p = \overline{p} + p'$$

The continuity equation containing total values becomes

$$\overline{\frac{\partial}{\partial x}(\overline{u} + u') + \frac{\partial}{\partial y}(\overline{v} + v')} = 0.$$

Simplifying the equation becomes

$$\overline{\frac{\partial}{\partial x}(\overline{u})} + \overline{\frac{\partial}{\partial x}(u')} + \overline{\frac{\partial}{\partial y}(\overline{v})} + \overline{\frac{\partial}{\partial y}(v')} = 0$$

with

$$\overline{\frac{\partial}{\partial x}(\overline{u})} = \frac{\partial}{\partial x}(\overline{u}) \quad \text{and} \quad \overline{\frac{\partial}{\partial x}(u')} = \frac{\partial}{\partial x}(\overline{u'}) = 0$$

$$\overline{\frac{\partial}{\partial x}(\overline{v})} = \frac{\partial}{\partial x}(\overline{v}) \quad \text{and} \quad \overline{\frac{\partial}{\partial x}(v')} = \frac{\partial}{\partial x}(\overline{v'}) = 0.$$

The time-averaged continuity equation for turbulent flow is now

$$\frac{\partial}{\partial x}(\overline{u}) + \frac{\partial}{\partial y}(\overline{v}) = 0 \qquad (4.6)$$

Applying total values, the steady version of the Navier Stokes equation (2.23) becomes

$$(\overline{u} + u')\frac{\partial(\overline{u} + u')}{\partial x} + (\overline{v} + v')\frac{\partial(\overline{u} + u')}{\partial y} = -\frac{1}{\rho}\frac{\partial(\overline{p} + p')}{\partial x}$$

$$+ \nu\left[\frac{\partial^2(\overline{u} + u')}{\partial x^2} + \frac{\partial^2(\overline{u} + u')}{\partial y^2}\right]. \tag{4.7}$$

After simplifying, the time-averaged Navier-Stokes equation for turbulent flow [Ref. 1:p. C-10] becomes

$$\overline{u}\frac{\partial}{\partial x}(\overline{u}) + \overline{v}\left[\frac{\partial(\overline{u})}{\partial y}\right] = -\frac{1}{\rho}\frac{\partial\overline{p}}{\partial x} + \nu\left(\frac{\partial^2\overline{u}}{\partial x^2} + \frac{\partial^2\overline{u}}{\partial y^2}\right)$$

$$-\frac{\partial}{\partial x}(\overline{u'^2}) - \frac{\partial}{\partial y}(\overline{u'v'}). \tag{4.8}$$

The new terms, $\partial/\partial x(\overline{u'^2})$ and $\partial/\partial y(\overline{u'v'})$, which correspond to normal and shear stress, are called Reynolds stresses. The similar y-component terms are $\partial/\partial y(\overline{v'^2})$ and $\partial(\overline{v'u'})/\partial x$.

C. TURBULENCE MODELS

The time-averaged Navier-Stokes equation is nearly identical to the original equation except that the instantaneous values are replaced by the mean or time-

23

averaged values and two additional terms involving
fluctuating velocities, u' and v', appear. An interpretation
of these two terms compares them to the previously existing
terms $\partial^2\bar{u}/\partial x_2$ and $\partial^2\bar{u}/\partial y_2$. The right hand side of equation
(4.8) less the pressure term, and after multiplying by
density, becomes

$$\mu\frac{\partial^2\bar{u}}{\partial x^2} + \mu\frac{\partial^2\bar{u}}{\partial y^2} - \rho\frac{\partial}{\partial x}\overline{u'^2} - \rho\frac{\partial}{\partial y}\overline{u'v'}$$

or

$$\frac{\partial}{\partial x}(\mu\frac{\partial\bar{u}}{\partial x} - \rho\overline{u'^2}) + \frac{\partial}{\partial y}(\mu\frac{\partial\bar{u}}{\partial y} - \rho\overline{u'v'}).$$

As each term has the dimensions of stress, and $\mu(\partial u/\partial y)$ is
part of the laminar shear stress τ_{yx}, it appears that the
term $-\rho\overline{u'v'}$ represents a turbulent addition to shear stress
[Ref. 2:p. T-2]. Now, this shear stress is really a vertical
mixing of horizontally, travelling fluid particles. A model
of this mixing then calculates the rate of momentum transfer
involved.

1. Prandtl's Mixing-Length Model

To predict the turbulent stresses Prandtl assumed
that turbulent fluctuations are primarily the result of the
mean velocity differences between two layers in the flow.
Therefore, u' is proportional to $\partial u/\partial y$ with the
proportionality factor having the unit of length.

24

$$\overline{(u'^2)}^{\bullet} = a\frac{\partial\overline{u}}{\partial y} \tag{4.9}$$

Also, assuming that v' is of the same order of magnitude as u' at a particular point,

$$\overline{(v'^2)}^{\bullet} = b\frac{\partial\overline{u}}{\partial y}. \tag{4.10}$$

Substituting u' and v' into the turbulent shear stress, τ_T, is

$$-\overline{\rho u'v'} = -\rho ab\left(\frac{\partial\overline{u}}{\partial y}\right)\left(\frac{\partial\overline{u}}{\partial y}\right). \tag{4.11}$$

As a and b are both unknown constants of length, they both may be replaced by the "mixing length", l, the hypothetical distance between the two layers involved. The turbulent shear stress is now

$$\tau_T = \rho l^2 \left|\frac{\partial\overline{u}}{\partial y}\right|\frac{\partial\overline{u}}{\partial y} \tag{4.12}$$

which insures the correct sign.

2. Eddy Viscosity - Cebeci-Smith

The turbulent addition to shear stress may also be modeled in terms of "eddy viscosity". As laminar shear

stress $= \tau_{yx} = \mu(\partial u/\partial y) = \rho \nu(\partial u/\partial y$, turbulent shear stress may be equated

$$- \overline{\rho u'v'} = \rho \nu_t \frac{\partial \overline{u}}{\partial y}, \qquad (4.13)$$

where ν_t, the eddy viscosity is empirically determined.

The method used here is that of Cebeci and Smith as modified by Cebeci, Clark, Chang, Halsey and Lee, [Ref. 1:p. 327].

Eddy viscosity by Cebeci is represented by

$$\nu_t = \begin{bmatrix} \{0.4y[1 - \exp(-\dfrac{y}{A})]\}^2 \left| \dfrac{u}{y} \right| \gamma_{tr} & (0 \leq y \leq y_c) & (4.14) \\[4mm] \alpha \left| \displaystyle\int_o^\infty (u_e - u)dy \right| \gamma_{tr}\gamma & (y_c \leq y \leq \delta) & (4.15) \end{bmatrix}$$

where

$$A = \frac{26\nu}{\left[\nu \dfrac{u}{y} \right]^{\frac{1}{2}}_{max}} \qquad \text{and} \qquad \gamma = \frac{1}{1 + 5.5(y/\delta)^6} .$$

The distance from the body y_c which is less than the boundary layer thickness, δ, is the distance where the two equations (4.14 and (4.15 give the same resultant ν_t.

26

The intermittency factor, γ_{tr}, which indicates the local fraction of turbulent flow to total flow, is given by

$$\gamma_{tr} = 1 - \exp\left[- G(x - x_{tr}) \int_{x_{tr}}^{x} \frac{dx}{u_e}\right]. \qquad (4.16)$$

The location of the start of transition is x_{tr}, and the empirical factor G is

$$G = \frac{1}{1200} \frac{u_e^3}{v^2} R_{x_{tr}}^{-1.34} \qquad (4.17)$$

where $R_{x_{tr}}$ is the transition Reynolds number

$$R_{x_{tr}} = (u_e X/v)_{tr}. \qquad (4.18)$$

In equation (4.17) the empirical constant $G\gamma_{tr} = 1200$, was used by Chen and Thyson [Ref. 4:p. 327]. Values lower than 1200 may give better results at low Reynolds numbers as will be discussed in Section VII.

The expression for a is

$$a = \frac{0.0168}{F^{2.5}} = \frac{0.0168}{\left[1 - \beta\dfrac{\partial u/\partial x}{\partial u/\partial y}\right]^{2.5}} \qquad (4.19)$$

The non-dimensional factor F represents the ratio of the product of the turbulent energy by normal stresses to

27

that by shear stress evaluated at the location where shear stress is maximum.

$$F = 1 - \left[\frac{(\overline{u'^2} - \overline{v'^2})\partial u/\partial x}{- \overline{u'v'}\ \partial u/\partial y} \right]_{(-\overline{u'v'})_{MAX}}$$

(4.20)

According to the data of Nakayama [Ref. 1:p. 327], ß can be represented by

$$ß = \left[\frac{\overline{u'^2} - \overline{v'^2}}{- \overline{u'v'}} \right]_{(-\overline{u'v'})_{MAX}} = \left[\begin{array}{ll} \dfrac{6}{1 + 2R_T(2 - R_T)} & R_T < 1 \\[3ex] \dfrac{1 + R_T}{R_T} & R_T \geq 1 \end{array} \right.$$

where $R_T = \tau_w/(-\overline{u'v'})_{MAX}$ and τ_w is the wall (body) shear stress.

D. TRANSITION

The location of the onset of laminar-to-turbulent transition when not found experimentally is determined empirically. The method used by Cebeci [Ref. 4:p. 333] is the criterion proposed by Michel.

At the point of transition the Reynolds number based on momentum thickness, Θ, is related to the Reynolds number based on the coordinate position, x.

28

$$R_{\theta tr} = 1.174 \left(1 + \frac{22400}{R_{extr}}\right) R_{extr}^{0.46} \qquad (4.21)$$

where

$$R_{ex} \equiv U_e(x/\nu) \text{ and } R_{\theta tr} \equiv U_e(\theta/\nu).$$

In the Cebeci Code the transition may be determined in the following ways:

1) The points of transition are calculated using Michel's criterion.

2) If laminar separation occurs forward of the criterion points, Michel's criterion is disregarded and transition is redefined at the separation point.

3) The transition locations may be specified by the user provided stall is not computed.

V. VISCOUS METHODS

Momentum transfer in fluids is accomplished by hydrostatic pressure and viscous stresses. When viscous stresses are negligible, fluid behavior can be predicted by inviscid flow methods as stated in Section III.

Viscous stresses caused by a variation in velocity in a direction normal to the flow are called shear. The most common shear is that found in the boundary layer between a displayed stream and the solid surface. With the "no slip" condition fluid velocity is zero on the surface, but the velocity gradient is not so constrained. From the body along its normal direction the fluid velocity asymptotically approaches that of the free stream.

As mentioned in Section III, Prandtl hypothesized the division of the flowfield into the two regions, the boundary layer where viscous effects cannot be neglected and the region outside the boundary layer which may be considered inviscid.

This hypothesis allows for the use of the parabolic boundary layer equations of section III instead of the elliptic Navier-Stokes equations. Depending on the boundary conditions, solutions fall into three methods [Ref. 6:p. 13]:

1) The direct boundary layer method. This method uses the "no slip" condition, where normal and tangential velocities are zero at the surface, and a pre-determined velocity is specified at the boundary layer edge.

30

2) The inverse boundary layer method. Boundary conditions are replaced by wall shear or displacement thicknesses.

3) The interactive boundary layer method. The edge boundary condition drives a combination of displacement thickness and external velocity.

Methods one and three will be discussed as they apply to the Cebeci Code.

A. DIRECT BOUNDARY LAYER METHOD [Ref. 6:p. 13]

This method for solving the boundary layer equations is used only near the leading edge where the viscous effects are small. Initial conditions are generated at the stagnation point and the equations are integrated around the leading edge. The numerical solution utilizes a finite difference method where the continuity and momentum equations are redefined as a system of linear algebraic equations.

The method begins by describing steady, incompressible, 2-D flows in a curvilinear coordinate system where x is directed along the airfoil surface and y is perpendicular to x. The boundary layer equations with the turbulent Reynolds stress are

$$\frac{\partial \bar{u}}{\partial x} + \frac{\partial \bar{v}}{\partial y} = 0 \qquad (5.1)$$

$$-\frac{1}{\rho}\frac{\partial \bar{p}}{\partial x} + \frac{1}{\rho}\frac{\partial}{\partial y}[\mu\frac{\partial \bar{u}}{\partial y} - \rho\overline{u'v'}] = \bar{u}\frac{\partial \bar{u}}{\partial x} + \bar{v}\frac{\partial \bar{u}}{\partial y} \qquad (5.2)$$

31

$$\frac{\partial \overline{p}}{\partial y} = 0. \qquad (5.3)$$

where the order of magnitude of any turbulent stress is assumed to be that of its laminar stress. The boundary conditions are:

$$\text{at } y = 0; \quad \overline{u} = 0, \quad \overline{v} = 0 \qquad (5.4)$$

$$\text{at } y = \infty; \quad \overline{u} = \overline{U}_e(x) \qquad (5.5)$$

The eddy viscous stress previously defined is reprinted as

$$-\rho \overline{u'v'} = \rho \nu_t \frac{\partial u}{\partial y}. \qquad (4.13)$$

Also, the pressure gradient term may be written

$$-\frac{1}{\rho} \frac{\partial p}{\partial x} = u_e \frac{\partial u_e}{\partial x} \qquad (5.6)$$

Therefore, the momentum equation (5.2) may be rewritten as

$$\overline{u} \frac{\partial \overline{u}}{\partial x} + \overline{v} \frac{\partial \overline{u}}{\partial y} = u_e \frac{\partial u_e}{\partial x} + \frac{\partial}{\partial x} (b \frac{\partial \overline{u}}{\partial y}) \qquad (5.7)$$

where $b = 1 + \nu_t/\nu$ and the boundary conditions are

$$\text{at } y = 0; \quad \overline{u}(x,0) = 0, \quad \overline{v}(x,0) = 0 \qquad (5.8)$$

$$\text{at } y = y_e; \quad \overline{u}(x,y_e) = u_e(x).$$

32

1. Falkner-Skan Transformation [Ref. 6:p. 14]

To solve the new boundary layer equations the Falkner-Skan transformations are used, which reduce the number of variables, and scale the normal coordinate y and the stream function ψ with reference to the external velocity.

$$\eta = y \left[\frac{u_e}{\nu x} \right]^{\frac{1}{2}} \qquad (5.9)$$

$$\psi(x,y) = (u_e x)^{\frac{1}{2}} \cdot f(x,\eta) \qquad (5.10)$$

The continuity equation is automatically satisfied using the stream function ($u = \partial\psi/\partial y$ and $v = -\partial\psi/\partial x$). Therefore, only the momentum equation needs to be solved, which after transformation becomes

$$(bf'')^{\cdot} + \frac{m+1}{2} ff'' + m[1 - (f')^2] = x(f'\frac{\partial f'}{\partial x} - f''\frac{\partial f}{\partial x}) \quad (5.11)$$

where $m = (x/u_e)(du_e/\partial x)$, a dimensionless pressure-gradient, and $f' = \partial f/\partial \eta$.

This equation (5.11) is a third order partial differential equation, and the solutions are "non-similar" as they are functions of both x and η. If the solutions were only a function of η, then the right hand side of the equation would equal zero, and the flow would be "similar"

33

[Ref. 1:p. v-10]. To solve equation (5.11), a numerical solution is needed such as the "box" method.

2. The Box Method

The box method, developed by Keller in 1970 [Ref. 1:p. 331], is a widely used methods for solving non-linear differential equations. The steps of this method include the conversion of the Falkner-Skan, transformed, momentum equation into a system of first-order partial differential equations. This non-linear system, after conversion from a continuous function to discrete, is linearized by Newton's method. The block elimination method is then used to solve the linearized difference equations of the boundary layer problem.

The third order momentum equation (5.11) is converted into a first order system with the addition of the dependent variables U and V [Ref. 6:p. 14].

$$U = f' \tag{5.12}$$

$$V = U' = f'' \tag{5.13}$$

$$(bV)' + \frac{m + 1}{2}fV + m(1 - U^2) = x(U\frac{\partial U}{\partial x} - V\frac{\partial f}{\partial x}) \tag{5.14}$$

The boundary conditions are

at $\eta = 0$; $U(x,0) = 0$, $f(x,0) = 0$

at $\eta = \eta_e$; $U(x,\eta_e) = 1$

34

The solution domain, $0 \leq x \leq x_I$ and $0 \leq \eta \leq \eta_J$, of the continuous functions f, U and V is then covered by a rectangular grid to facilitate the problem solving with a set of discrete values. This grid is shown in Figure 5.1.

The subsequent notation [ ]$_j^i$ is used to represent the quantities of f, U or V at the point (x_i, η_j).

All quantities can then be approximated by network coordinate values. Using the grid system, the solution of the parabolic layer equation at a certain streamline position depends solely on the solution of upstream positions, while no downstream influence needs to be considered. As calculations proceed from the stagnation point in the downstream direction, the overall solution can be obtained incrementally. Hence, one step of the solution procedure sets up the governing equations for a column of grid boxes in the sub-domain

$$x_{i-1} \leq x \leq x_i \text{ and } 0 \leq \eta \leq \eta_J$$

and solves for the values of the downstream grid position. The x-grid position currently solved for is then assigned the superscript "i" while "i-1" represents the previous position of known properties. Using coordinates of box midpoints and centered-difference derivatives, the equations are actually satisfied midway between the grids.

Equations (5.12) through (5.14) in terms of finite differences [Ref. 6:p. 15] are now written
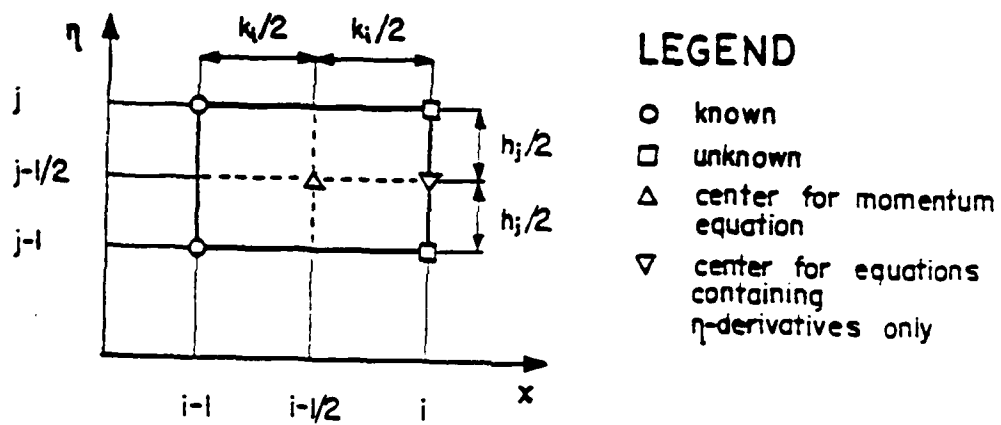
Figure 5.1   Rectangular Grid   for Finite Difference
                 Approximation

$$\frac{f_j^i - f_{j-1}^i}{h_j} = \frac{1}{2}(U_j^i + U_{j-1}^i) \qquad (5.15)$$

$$\frac{U_j^i - U_{j-1}^i}{h_j} = \frac{1}{2}(V_j^i + V_{j-1}^i) \qquad (5.16)$$

$$\frac{(bV)_j^{i-\frac{1}{2}} - (bV)_{j-1}^{i-\frac{1}{2}}}{h_j} + \frac{m^{i-\frac{1}{2}} + 1}{2}(fV)_{j-\frac{1}{2}}^{i-\frac{1}{2}} +$$

$$m^{i-\frac{1}{2}}\left[1 - (V_{j-\frac{1}{2}}^{i-\frac{1}{2}})^2\right] = x_{i-\frac{1}{2}}\left[U_{j-\frac{1}{2}}^{i-\frac{1}{2}} \frac{U_{j-\frac{1}{2}}^i - U_{j-\frac{1}{2}}^{i-1}}{k_i} - \right.$$

$$\left. V_{j-\frac{1}{2}}^{i-\frac{1}{2}} \frac{f_{j-\frac{1}{2}}^i - f_{j-\frac{1}{2}}^{i-1}}{k_i}\right] \qquad (5.17)$$

where the ordinary differential equations, (5.15) and (5.16), are centered about $(x_i, \eta_{j-\frac{1}{2}})$ and the partial differential equation, (5.17), is centered about $(x_{i-\frac{1}{2}}, \eta_{j-\frac{1}{2}})$.

The boundary conditions are

$$U_1^i = 0, \quad f_1^i = 0 \text{ and } U_j^i = 1$$

Equations (5.15) and (5.16) are the centered difference derivatives.

3. Newton's Method [Ref. 6:p. 15]

This set of finite difference equations is nonlinear with combinations of unknowns. Newton's method is therefore

needed to solve the system. The variables are linearized using an iterative procedure with preceding values.

$$f_j^{i,1} = f_j^{i-1} + \delta f_j^{i \cdot 1} \text{ and } f_j^{i,K} = f_j^{i,K-1} + \delta f_j^{i \cdot K} \text{ for } K \geq 2$$

where, $\delta f_j^{i \cdot K} << f_j^{i \cdot K-1}$

$$U_j^{i,1} = U_j^{i-1} + \delta U_j^{i \cdot 1} \text{ and } U_j^{i,K} = U_j^{i,K-1} + \delta_j^{i \cdot K} \text{ for } K \geq 2$$

where, $\delta U_j^{i \cdot K} << U_j^{i \cdot K-1}$

$$V_j^{i,1} = V_j^{i-1} + \delta V_j^{i \cdot 1} \text{ and } V_j^{i,K} = V_j^{i,K-1} + \delta V_j^{i \cdot K} \text{ for } K \geq 2$$

where, $\delta V_j^{i \cdot K} << V_j^{i \cdot K-1}$

K is the iteration counter. After substituting these values into equations (5.15) through (5.17) and neglecting the quadratic terms of $\delta f_j^{i,K}$, $\delta U_j^{i,K}$ and $\delta V_j^{i \cdot K}$, the system of unknowns is then linear.

$$\delta f_j^{i \cdot K} - \delta f_{j-1}^{i \cdot K} - \frac{h_j}{2}(\delta U_j^{i \cdot K} + \delta U_{j-1}^{i \cdot K}) = f_{j-1}^{i \cdot K-1} - f_j^{i \cdot K-1}$$

$$+ h_j U_{j-\frac{1}{2}}^{i \cdot K-1} \tag{5.18}$$

$$\delta U_j^{i \cdot K} - \delta U_{j-1}^{i \cdot K} - \frac{h_j}{2}(\delta V_j^{i \cdot K} + \delta V_{j-1}^{i \cdot K}) = U_{j-1}^{i \cdot K-1} - U_j^{i \cdot K-1}$$

$$+ h_j V_{j-\frac{1}{2}}^{i \cdot K-1} \tag{5.19}$$

$$(S_1)_j^{i.K} \delta V_j^{i.K} + (S_2)_j^{i.K} \delta V_j^{i.K} + (S_3)_j^{i.K} \delta f_j^{i.K} +$$

$$(S_4)_j^{i.K} \delta f_{j-1}^{i.K} + (S_5)_j^{i.K} \delta U_j^{i.K} + (S_6)_j^{i.K} \delta U_{j-1}^{i.K} = (r_2)_j^{i.K} \qquad (5.20)$$

where

$$(S_1)_j^{i.K} = \frac{b_j^{i.K-1}}{h_j} + \frac{x_{i-\frac{1}{2}}}{2k_i} (f_{j-\frac{1}{2}}^{i.K-1} - f_{j-\frac{1}{2}}^{i-1}) + \frac{m^{i+1}}{4} f_{j-1}^{i.K-1}$$

$$(S_2)_j^{i.K} = -\frac{b_j^{i.K-1}}{h_j} + \frac{x_{i-\frac{1}{2}}}{2k_i} (f_{j-\frac{1}{2}}^{i.K-1} - f_{j-\frac{1}{2}}^{i-1}) + \frac{m^i + 1}{4} f_{j-1}^{i.K-1}$$

$$(S_3)_j^{i.K} = \frac{x_{j-\frac{1}{2}}}{1k_i} (V_{j-\frac{1}{2}}^{i.K-1} + V_{j-\frac{1}{2}}^{i-1}) + \frac{m^i + 1}{4} V_j^{i.K-1}$$

$$(S_4)_j^{i.K} = \frac{x_{j-\frac{1}{2}}}{2k_i} (V_{j-\frac{1}{2}}^{i.K-1} + V_{j-\frac{1}{2}}^{-1}) + \frac{m^i + 1}{4} V_{j-1}^{i.K-1}$$

$$(S_5)_j^{i.K} = - (\frac{x_{i-\frac{1}{2}}}{k_i} + m^i) U_j^{i.K-1}$$

$$(S_6)_j^{i.K} = - (\frac{x_{i-\frac{1}{2}}}{k} + m^i) U_{j-1}^{i.K-1}$$

$$(r_2)_j^{i.K} = - \{ (\frac{(bV)_j^{i.K-1} - (bV)_{j-1}^{i.K-1}}{h_j} + \frac{m + 1}{2}(fV)_{j-\frac{1}{2}}^{i.K-1}$$

$$- (\frac{x_{i-\frac{1}{2}}}{k_i} + m^i)(U_{j-\frac{1}{2}}^{i.K-1})^2 + \frac{x_{i-\frac{1}{2}}}{k_i}(V_{j-\frac{1}{2}}^{i.K-1} f_{j-\frac{1}{2}}^{i.K-1}$$

39

$$+ V_{j-\frac{1}{2}}^{i-1} f_{j-\frac{1}{2}}^{i.K-1} - f_{j-\frac{1}{2}}^{i-1} V_{j-\frac{1}{2}}^{i.K-1}))$$

$$- \{((\frac{(bV)_{j}^{i-1} - (bV)_{j-1}^{i-1}}{h_j}) + \frac{m^{i-1}+ 1}{2} fV)_{j-\frac{1}{2}}^{i-1}$$

$$+ (\frac{x_{i-\frac{1}{2}}}{k_i} + m^{i-1})(U_{j-\frac{1}{2}}^{i-1})^2 - \frac{x_{i-\frac{1}{2}}}{k_i}(V_{j-\frac{1}{2}}^{i-1} f_{j-\frac{1}{2}}^{i-1}$$

$$+ 2m^{i-\frac{1}{2}}\}$$

The boundary conditions are

$$\delta f_o = 0, \quad \delta U_o = 0, \quad \delta U_J = 0$$

4. **Block Elimination Method [Ref. 6:P. 17]**

The system of equations are iteratively solved until

$\delta f_j^{i.K}$, $\delta U_j^{i.K}$ and $\delta V_j^{i.K}$ become small enough to be neglected.

The solution method is that by Keller and is called the Block Elimination Method. In this method block-tridiagonal matrices are composed of blocks. Only those blocks on the main diagonal and on the two adjacent diagonals are non-zero.

$$\begin{bmatrix} [A_1^{i.K}] & [C_1^{i.K}] & & & & \\ [B_2^{i.K}] & [A_2^{i.K}] & [C_2^{i.K}] & & & \\ & \ddots & \ddots & \ddots & & \\ & & [B_j^{i.K}] & [A_j^{i.K}] & [C_j^{i.K}] & \\ & & & \ddots & \ddots & \ddots \\ & & & & [B_{J-1}^{i.K}] & [A_{J-1}^{i.K}] & [C_{J-1}^{i.K}] \\ & & & & & [B_J^{i.K}] & [A_J^{i.K}] \end{bmatrix} \begin{Bmatrix} \{\delta_1^{i.K}\} \\ \{\delta_1^{i.K}\} \\ \vdots \\ \{\delta_j^{i.K}\} \\ \vdots \\ \{\delta_{J-1}^{i.K}\} \\ \{\delta_J^{i.K}\} \end{Bmatrix} = \begin{Bmatrix} \{r_1^{i.K}\} \\ \{r_1^{i.K}\} \\ \vdots \\ \{r_j^{i.K}\} \\ \vdots \\ \{r_{J-1}^{i.K}\} \\ \{r_J^{i.K}\} \end{Bmatrix} \quad (5.21)$$

where the blocks are 3x3 matrices

$$[A_j^{i.K}] = \begin{bmatrix} 1 & -h_j/2 & 0 \\ (S_3)_j^{i.K} & (S_5)_j^{i.K} & (S_1)_j^{i.K} \\ 0 & -1 & -h_{j+1}/2 \end{bmatrix} \qquad 2 \le j \le J-1$$

$$[B_j^{i.K}] = \begin{bmatrix} -1 & -h_j/2 & 0 \\ (S_4)_j^{i.K} & (S_6)_j^{i.K} & (S_2)_j^{i.K} \\ 0 & 0 & 0 \end{bmatrix} \qquad 2 \le j \le J$$

$$[C_j^{i.K}] = \begin{bmatrix} 0 & 0 & 0 \\ 0 & 0 & 0 \\ 0 & 1 & -h_{j+1}/2 \end{bmatrix} \qquad 1 \le j \le J-1$$

$$[A_j^{i.K}] = \begin{bmatrix} 1 & 0 & 0 \\ 0 & 1 & 0 \\ 0 & -1 & -h_2/2 \end{bmatrix}$$

$$[A_J^{i.K}] = \begin{bmatrix} 1 & -h_J/2 & 0 \\ (S_3)_J^{i.K} & (S_5)_J^{i.K} & (S_1)_J^{i.K} \\ 0 & 1 & 0 \end{bmatrix}$$

The right-hand sides of the equations are

$$(r_1)_j^{i.K} = f_{j-1}^{i.K-1} - f_j^{i.K-1} + h_j U_{j-\frac{1}{2}}^{i.K-1} \qquad 2 \le h \le J$$

$$(r_2)_j^{i.K} = \{\text{As defined in equation (5.20)}\} \qquad 2 \le j \le J$$

$$(r_3)_j^{i.K} = U_j^{i.K-1} - U_{j-1}^{i.K-1} + h_{j+1} V_{j+\frac{1}{2}}^{i.K-1} \qquad 2 \le h \le J$$

$$(r)_1^{i.K} = 0, \quad (r_2)_1^{i.K} = 0, \quad (r_3)_J^{i.K} = 0$$

The block elimination method solves the linear equations with two steps. The forward step eliminates the lower diagonal of the tridiagonal matrix. The reverse step solves the remaining system from bottom to top.

B. INTERACTIVE BOUNDARY LAYER METHOD [Ref. 6:p. 18]

As the direct boundary layer method is, as previously stated, restricted to regions of small viscous effects, and integration of the boundary layer equations fails at points of zero skin friction, a method is needed to integrate the boundary layer through the point of emerging reversed flow. This method must also account for strong interaction effects

42

due to separation and rapid acceleration of the flow downstream of the trailing edge.

The interactive method fulfills these requirements by treating the external velocity and displacement thickness as unknown quantities. Reflecting the elliptic nature of the outer flows, an additional unknown is introduced, but the solution can be obtained using either the eigenvalue or Mechul function methods.

The Mechul method is preferred as the eigenvalue method involves nonlinear problems. In this method the edge boundary condition of the direct method is supplemented with the interactive boundary condition. The unknown external velocity is related to its displaced and perturbed conditions. The unknown functions $u(x,y)$, $v(x,y)$ and $u_e(x,y)$ are represented in this system of boundary layer equations

$$\frac{\partial u}{\partial x} + \frac{\partial v}{\partial y} = 0 \qquad (5.22)$$

$$u\frac{\partial u}{\partial x} + v\frac{\partial u}{\partial y} = u_e\frac{\partial u_e}{\partial x} + v\frac{\partial}{\partial y}(b\frac{\partial u}{\partial y}) \qquad (5.23)$$

$$\frac{\partial u_e}{\partial y} = 0 \qquad (5.24)$$

where pressure in the y-momentum equation is expressed in terms of the external velocity.

The Mechul function approach assumes that the external velocity, u_e, is a function of two arguments, x and y, allowing for an easy setup of finite difference equations,

43

and avoiding nonlinear eigenvalue techniques. The velocity components u and v are required to satisfy the no-slip condition at the surface, and u must merge smoothly into the edge velocity.

at $y = 0$: $u(x,0) = 0$, $v(x,0) = 0$

at $y = y_e$: $u(x,Y_e) = u_e(x,Y_e)$, $u_e(x,Y_e) =$

$$= U_{er} + \frac{1}{\pi} \int \frac{d}{d\xi}(u_e\delta^*)\frac{d\xi}{x-\xi}$$

$U_{er}(x)$ is the inviscid edge velocity and the last term, the Hilbert integral, approximates the viscosity induced, perturbation velocity.

Interactive methods are useful in both attached and separated regions, while direct methods fail at the onset of reversed flow, and inverse methods converge poorly. Only at the stagnation point singularity are interactive methods prohibited. The transformation of the partial differential equations into a linear system of algebraic equations is very similar to that of the direct method. The normal coordinate y, streamfunction ψ, and the external velocity u_e are scaled with reference to a constant velocity u_o, and the local streamwise coordinate x.

$$\eta = y\left[\frac{u_o}{\nu x}\right]^{\frac{1}{2}} \qquad (5.25)$$

44

$$\psi(x,y) = (u_o \nu x)^* f(x,\eta) \qquad (5.26)$$

$$W(x,\eta) = \frac{u_e(x,y)}{u_o} \qquad (5.27)$$

U_o is the vector mean velocity. U_e cannot be the reference velocity as for Falkner-Skan variables because in this case the external velocity is unknown. The first order, semi-transformed coordinate system with additional variables U and V is

$$U = f' \qquad (5.28)$$

$$V = U' = f'' \qquad (5.29)$$

$$(bV)' + \frac{1}{2} fV + xW\frac{\partial W}{\partial x} = x(U\frac{\partial U}{\partial x} - V\frac{\partial f}{\partial x}) \qquad (5.30)$$

$$W' = 0 \qquad (5.31)$$

and the boundary conditions are

at $\eta = 0$: $U(x,0) = 0$, $f(x,0) = 0$

at $\eta = \eta_e$: $U(x,\eta_e) = W(x,\eta_e)$

$$W(x,\eta_e) = \frac{u_{eI}(x)}{u_o} + \frac{1}{\pi} \int \frac{d}{d\xi} \{(\frac{\nu\xi}{u_o})^* [W(\xi,\eta_e)\eta_e}$$

$$- f(\xi,\eta_e)]\}\frac{d\xi}{x-\xi}$$

The conversion of the flowfield to discrete values is very similar to that of the direct method with an orthogonal grid, central differences, and two-point averages. In the interactive method though, the solution proceeds in the downstream direction only. As only downstream disturbances are accounted for, backflow causes numerical instabilities. A stable integration can be accomplished though, with the assumption that backflow velocities are comparatively small. The FLARE approximation (Flugge-Lotz and Reyhner), [Ref. 6:p. 19] sets the streamwise convection term $u\partial u/\partial x$ equal to zero in regions of backflow.

$$FLR_{j-\frac{1}{2}}^{i} = \begin{bmatrix} 1 & \text{if} & U_{j-\frac{1}{2}}^{i} \geq 0 \\ 0 & \text{if} & U_{j-\frac{1}{2}}^{i} < 0 \end{bmatrix}$$

The finite difference equations of the interactive boundary layer with the "on-off switch" are now

$$\frac{f_{j}^{i} - f_{j-1}^{i}}{h_{j}} = \frac{1}{2}(U_{j}^{i} + U_{j-1}^{i}) \qquad (5.32)$$

$$\frac{U_{j}^{i} - U_{j-1}^{i}}{h_{j}} = \frac{1}{2}(V_{j}^{i} + V_{j-1}^{i}) \qquad (5.33)$$

$$\frac{(bV)_{j}^{i-\frac{1}{2}} - (bV)_{j-1}^{i-\frac{1}{2}}}{h_{j}} + \frac{1}{2}(fV)_{j-\frac{1}{2}}^{i-\frac{1}{2}} + x_{i-\frac{1}{2}}(W^{i-\frac{1}{2}} \frac{W^{i} - W^{i-1}}{k_{i}})_{j-\frac{1}{2}}$$

46

$$= x_{i-\frac{1}{2}} \left[FLR_{j-\frac{1}{2}}^i (U^{i-\frac{1}{2}} \frac{U^i - U^{i-1}}{k_i})_{j-\frac{1}{2}} - (V^{i-\frac{1}{2}} \frac{f' - f^{i-\frac{1}{2}}}{k_i})_{j-\frac{1}{2}} \right]$$

$$\frac{W_j^i - W_{j-1}^i}{h_j} = 0. \qquad\qquad (5.34) \text{ and } (5.35)$$

The boundary conditions are also expressed in terms of grid or nodal values.   A panel method type approximation leads to

$$U_1^i = 0, \quad f_1^i = 0$$

$$U_J^i = W_J^i, \quad W_J^i = g_i + c_{ii}(W_J^i \eta_J - f_j^i)$$

where g_i and c_{ii} represent a parameter and the diagonal element of the interaction matrix, due to a discrete approximation to the Hilbert integral. To keep the number of generated terms to a minimum, ordinary differential equations like the y-momentum equation are centered about the downstream face, and partial differential equations like the x-momentum equation are centered about the middle of the box.

The unknowns occur in vectors of four components

$$\{f_j^i, \quad U_j^i, \quad V_j^i, \quad W_j^i\}.$$

The J quadruplets of unknowns match with 4J equations, including 2(J-1) auxiliary relations and (j-1) x-momentum and (j-1) y-momentum equations. Each equation corresponds to one

of the (j-1) grid rectangles and four boundary conditions. The system is linearized around the values of the preceding iteration (counter K-1) and a system with Newton iterates

$$\delta f_j^{i.K}, \quad \delta U_j^{i.K}, \quad \delta V_j^{i.K}, \quad \delta W_j^{i.K}, \text{ emerges.}$$

$$\delta f_j^{i.K} - \delta f_{j-1}^{i.K} - \frac{h_j}{2}(\delta U_j^{i.K} + \delta a_{j-1}^{i.K}) = f_{j-1}^{i.K-1} - f_j^{i.K-1}$$

$$+ h_j \, U_{j-\frac{1}{2}}^{i.K-1} \tag{5.36}$$

$$\delta U_j^{i.K} - \delta U_{j-1}^{i.K} - \frac{h_j}{2}(\delta V_j^{i.K} + \delta V_{j-1}^{i.K}) = U_{j-1}^{i.K-1} - U_j^{i.K-1}$$

$$+ h_j \, V_{j-\frac{1}{2}}^{i.K-1} \tag{5.37}$$

$$(S_1)_j^{i.K}\delta V_j^{i.K} + (S_2)_j^{i.K}\delta V_{j-1}^{i.K} + (S_3)_j^{i.K}\delta f_j^{i.K} +$$

$$(S_4)_j^{i.K}\delta f_{j-1}^{i.K} + (S_5)_j^{i.K}\delta U_j^{i.K} + (S_6)_j^{i.K}\delta U_{j-1}^{i.K} +$$

$$(S_7)_j^{i.K}\delta W_j^{i.K} + (S_8)_j^{i.K}\delta W_{j-1}^{i.K} = \delta W_{j-1}^{i.K} = (r_2)_j^{i.K} \tag{5.38}$$

$$\delta W_j^{i.K} - \delta W_{j-1}^{i.K} = W_{j-1}^{i.K-1} - W_j^{i.K-1} \tag{5.39}$$

where

$$(S_1)_j^{i.K} = \frac{b_j^{i.K-1}}{h_j} + \frac{x_{i-\frac{1}{2}}}{2K_i}(f_{j-\frac{1}{2}}^{i.K-1} - f_{j-\frac{1}{2}}^{i-1}) + \frac{1}{4}f_j^{i.K-1}$$

48

$$(S_2)_j^{i.K} = -\frac{b_j^{i.K-1}}{h_j} + \frac{x_{i-\frac{1}{2}}}{2k_i}(f_{j-\frac{1}{2}}^{i.K-1} - f_{j-\frac{1}{2}}^{i-1}) + \frac{1}{4}f_{j-1}^{i.K-1}$$

$$(S_3)_j^{i.K} = -\frac{x_{i-\frac{1}{2}}}{2k_i}(V_{j-\frac{1}{2}}^{i.K-1} + V_{j-\frac{1}{2}}^{i-1}) + \frac{1}{4}V_j^{i.K-1}$$

$$(S_4)_j^{i.K} = -\frac{x_{i-\frac{1}{2}}}{2k_i}(V_{j-\frac{1}{2}}^{i.K-1} + V_{j-\frac{1}{2}}^{i-1}) + \frac{1}{4}V_{j-1}^{i.K-1}$$

$$(S_5)_j^{i.K} = -\frac{x_{i-\frac{1}{2}}}{k_i}U_j^{i.K-1}FLR_{j-\frac{1}{2}}^i$$

$$(S_6)_j^{i.K} = -\frac{x_{i-\frac{1}{2}}}{k_i}U_{j-1}^{i.K-1} \cdot FLR_{j-\frac{1}{2}}^i$$

$$(S_7)_j^{i.K} = \frac{x_{i-\frac{1}{2}}}{k_i}W_j^{i.K-1}$$

$$(S_8)_j^{i.K} = \frac{x_{i-\frac{1}{2}}}{k_i}W_{j-1}^{i.K-1}$$

$$(r_2)_j^{i.K} = -\{(\frac{(bV)_j^{i.K-1} - (bV)_{j-1}^{i.K-1}}{h_j} + \frac{1}{2}(fV)_{j-\frac{1}{2}}^{i.K-1}$$

$$+ (\frac{x_{i-\frac{1}{2}}}{k_i}[(W^2)_{j-\frac{1}{2}}^{i.K-1} - (U^2)_{j-\frac{1}{2}}^{i.K-1}FLR_{j-\frac{1}{2}}^i$$

$$+ V_{j-\frac{1}{2}}^{i.K-1} f_{j-\frac{1}{2}}^{i.K-1} + V_{j-\frac{1}{2}}^{i-1} f_{j-\frac{1}{2}}^{i.K-1}$$

$$- f_{j-\frac{1}{2}}^{i-1} \; V_{j-\frac{1}{2}}^{i.K-1}]\} - \{\frac{(bV)_j^{i-1} - (bV)_{j-1}^{i-1}}{h_J} + \frac{1}{2}(fV)_{j-\frac{1}{2}}^{i-1}$$

$$- (\frac{X_{i-\frac{1}{2}}}{K_i} \; [(W^2)_{j-\frac{1}{2}}^{i-1} - (U^2)_{j-\frac{1}{2}}^{i-1} FLR_{j-\frac{1}{2}}^{i}$$

$$+ V_{j-\frac{1}{2}}^{i-1} \; f_{j-\frac{1}{2}}^{i-1}]\}$$

The boundry conditions are

$$\delta U_1^{i.K} = 0, \; \delta f_1^{i.K} = 0, \; \delta U_J^{i.K} - \delta W_J^{i.K} = 0$$

$$\delta f_J^{i.K} + (\frac{1}{C_{ii}} - \eta_J)W_J^{i.K} = \frac{g_i}{C_{ii}} - f_J^{i.K-1} - (\frac{1}{C_{ii}} - \eta_J) \; W_J^{i.K-1}$$

The overall procedure is a repetitive, linear approach to solve the nonlinear system. The numerical solution is again obtained using the block elimination method by Keller, except that unlike the direct method the vectors of the unknown Newton iterates are four dimensional.

$$\{\delta_j^{i.K}\} = \delta f_j^{i.K}, \; \delta U_j^{i.K}, \; \delta V_j^{i.K}, \; \delta W_j^{i.K} \}^T$$

and

$$\{r_j^{i.K}\} = \{(r_1)_j^{i.K}, \; (r_2)_j^{i.K}, \; (r_3)_j^{i.K}, \; (r_4)_j^{i.K}\}^T$$

50

In matrix-vector form

$$
\begin{bmatrix}
[A_1^{i.K}] & [C_1^{i.K}] \\
[B_2^{i.K}] & [A_2^{i.K}] & [C_2^{i.K}] \\
& & \ddots & \ddots & \ddots \\
& & [B_j^{i.K}] & [A_j^{i.K}] & [C_j^{i.K}] \\
& & & \ddots & \ddots & \ddots \\
& & & & [B_{J-1}^{i.K}] & [A_{J-1}^{i.K}] & [C_{J-1}^{i.K}] \\
& & & & & [B_J^{i.K}] & [A_J^{i.K}]
\end{bmatrix}
\begin{Bmatrix}
\{\delta_1^{i.K}\} \\
\{\delta_2^{i.K}\} \\
\vdots \\
\{\delta_j^{i.K}\} \\
\vdots \\
\{\delta_{J-1}^{i.K}\} \\
\{\delta_J^{i.K}\}
\end{Bmatrix}
=
\begin{Bmatrix}
\{r_1^{i.K}\} \\
\{r_2^{i.K}\} \\
\vdots \\
\{r_1^{i.K}\} \\
\vdots \\
\{r_{J-1}^{i.K}\} \\
\{r_J^{i.K}\}
\end{Bmatrix}
$$

The 4x4 matrix blocks are

$$
[A_j^{i.K}] =
\begin{bmatrix}
1 & -h_j/2 & 0 & 0 \\
(S_3)_j^{i.K} & (S_5)_j^{i.K} & (S_1)_j^{i.K} & (S_7)_j^{i.K} \\
0 & -1 & -h_{j+1}/2 & \\
0 & 0 & 0 & 0
\end{bmatrix}
\qquad 2 \le j \le J-1
$$

$$
[B_j^{i.K}] =
\begin{bmatrix}
-1 & -h_j/2 & 0 & -1 \\
(S_4)_j^{i.K} & (S_6)_j^{i.K} & (S_2)_j^{i.K} & (S_8)_J^{i.K} \\
0 & 0 & 0 & 0 \\
0 & 0 & 0 & 0
\end{bmatrix}
\qquad 2 \le j \le J
$$

$$
[C_j^{i.K}] =
\begin{bmatrix}
0 & 0 & 0 & 0 \\
0 & 0 & 0 & 0 \\
0 & 1 & -h_{j+1}/2 & 0 \\
0 & 0 & 0 & 1
\end{bmatrix}
\qquad 1 \le j \le J-1
$$

51

$$[A_1^{i.K}] = \begin{bmatrix} 1 & 0 & 0 & 0 \\ 0 & 1 & 0 & 0 \\ 0 & -1 & -h_2/2 & 0 \\ 0 & 0 & 0 & -1 \end{bmatrix}$$

$$[A_1^{i.K}] = \begin{bmatrix} 1 & -h/2 & 0 & 0 \\ (S_3)_J^{i.K} & (S_5)_J^{i.K} & (S_1)_J^{i.K} & (S_7)_j^{i.K} \\ 1 & 0 & 0 & 1/C_{ii}-\eta_J \\ 0 & 0 & 0 & -1 \end{bmatrix}$$

$$(r_1)_j^{i.K} = f_{j-1}^{i.K-1} - f_j^{i.K-1} + h_j V_{j-\frac{1}{2}}^{i.K-1} \qquad 2 \le j \le J$$

$$(r_2)_j^{i.K} = \{\text{As defined in equation (5.38)}\} \qquad 2 \le j \le J$$

$$(r_3)_j^{i.K} = U_j^{i.K-1} - U_{j-1}^{i.K-1} + h_{j+1} V_{j+\frac{1}{2}}^{i.K-1} \qquad 1 \le j \le J-1$$

$$(r_4)_j^{i.K} = W_j^{i.K-1} - W_{j+1}^{i.K-1} \qquad 1 \le j \le J-1$$

$$(r_1)_1^{i.K} = 0, \quad (r_2)_1^{i.K} = 0$$

$$(r_3)^{i.K} = \frac{g_i - C_{ii}f_J^{i.K-1} - (1 - C_{ii-J})W_J^{i.K-1}}{C_{ii}}$$

and

$$(r_4)_J^{i.K} = 0$$

VI. INTERACTION METHODS [Ref. 7:p. 79]

Interactive methods couple viscous and inviscid flows and are intended to compute through regions of flow separation. Given their levels of success, these methods have become inexpensive alternatives to the Navier-Stokes solvers.

The simple, classical method of computing the viscous flow over an airfoil is:

1) The velocity distribution is computed for inviscid flow.

2) The inviscid velocity is input to the viscous flow.

3) The viscous flow is computed by integrating the boundary layer equations.

Now, this method is good at predicting lift and drag, but only if the flow remains attached, as information is transferred only once from inviscid to viscous regions. For more complex flow multiple information transfers are required.

Close coupling is needed to compute flows with separation or separation bubbles. A better method than the previously outlined classical method for exchanging information between viscous and inviscid regions is interaction. The different elements of interaction include direct and inverse, inviscid and viscous flow solvers. Table 6.1 illustrates the different elements.

The disadvantage of the direct boundary layer method is that the equations become singular at the point of

53

separation. The point of separation may be integrated through, however, if the external velocity is computed with a predetermined displacement thickness. This method is known as the inverse boundary layer method.

Another problem associated with separation is the instability of numerical methods which prohibits downstream marching in regions of reversed flow. In the situation where flow is reversed the FLARE approximation is used, where the momentum transport term $u\partial u/\partial x$ is neglected. This approximation is not necessarily accurate, but it does allow for continued calculations.

Four interaction models have been developed to calculate combined inviscid and viscous flows. All procedures solve the Laplace equation for inviscid flow and the boundary layer equations for viscous flow. The four models are the direct, inverse, semi-inverse and viscous-inviscid interaction methods. Each model is subject to different boundary conditions.

The first three models are considered weak interaction methods in that they provide only a loose coupling between viscous and inviscid regions. The two regions are treated alternately. As indicated in Table 6.1, the viscous flow solver calculates the flow in the viscous region and produces the boundary condition of the inviscid region. The inviscid

TABLE 6.1   INTERACTION ELEMENTS

| Flow | BOUNDARY CONDITION | |
	Direct	Inverse
Inviscid	* Zero normal velocity at the surface	* Prescription of velocity distribution
Viscous	* No slip condition * Prescription of external velocity	* No slip condition * Prescription of displacement thickness

flow solver calculates the flow in the inviscid region and produces the boundary condition of the viscous region. The weak interaction methods process either displacement thickness or external velocity as an input and the other quantity as an output.

In contrast, the fourth method, the simultaneous interaction method, is considered a strong interaction method. A strong method calculates displacement thickness and external velocity simultaneously. The foundation of the four interaction methods are discussed below.

A. DIRECT INTERACTION METHOD

The direct interaction model is composed of direct inviscid and viscous flow solvers as indicated in Figure 6.1a. The external velocity distribution is calculated first by inviscid computations. The displacement thickness, δ^*, is then calculated using the external velocity as a boundary condition. An updated shape of the displacement body is then computed, and all steps are recomputed in order until the results converge. As previously stated this method breaks down at the point of separation, and is therefore not useable in regions of separated flow. However, it is very useful where viscous effects are small. The direct method is used in the Cebeci Code around the nose and stagnation point of the airfoil.
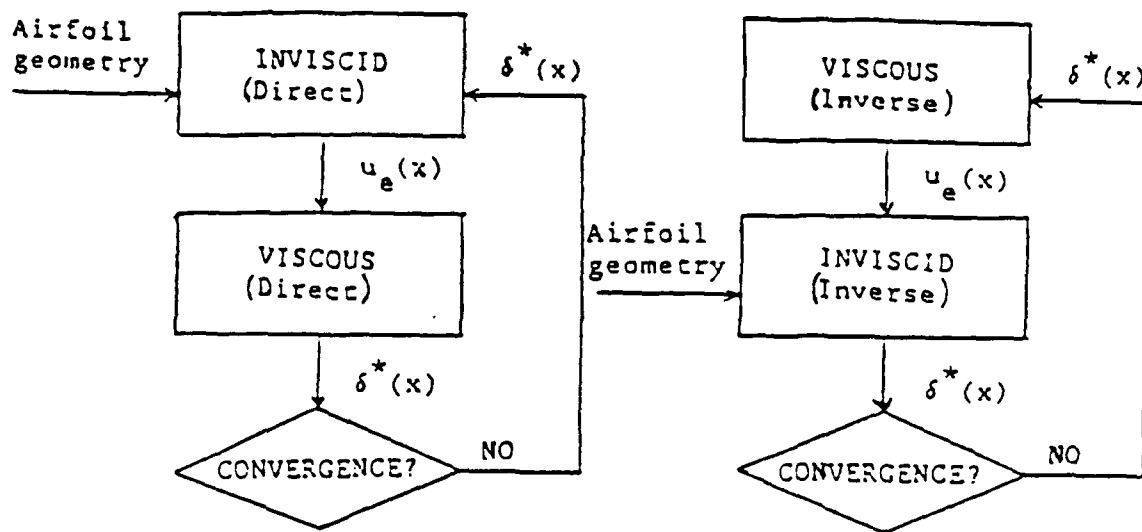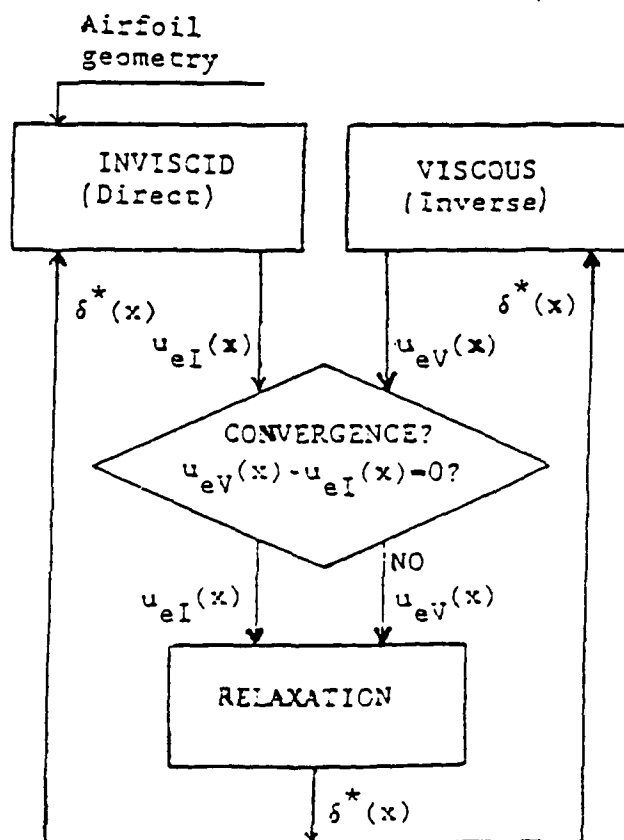
Figure 6.1   Organization of Interaction Methods
              a) Direct, b) Inverse and c) Semi-inverse

B. INVERSE INTERACTION METHOD

This method was developed to circumvent the singularity problems near separation. According to Figure 6.1b it uses inverse inviscid and viscous flow solvers. Because of the inverse method's very slow convergence, though, it is suitable only at singular points.

C. SEMI-INVERSE INTERACTION METHOD

The semi-inverse interaction method incorporates direct inviscid and inverse viscous flow solvers such that displacement thickness is input to both solvers as shown in Figure 6.1c. External velocity is output from both solvers. Convergence is ensured with the use of a relaxation formula which redefines the displacement thickness distribution.

$$\delta_{new}^*(x) = \delta_{old}^*(x)[1 + \omega(\frac{U_{ev}(x)}{Ue_{I}(x)} - 1) \qquad (6.1)$$

where ω is a relaxation parameter.

The numerical weaknesses of the direct and inverse methods are improved, but inviscid and viscous regions are still loosely coupled.

D. VISCOUS-INVISCID INTERACTION METHOD

The viscous-inviscid interaction method ensures a strong interaction between the outer, inviscid, and inner, viscous, regions. Both the external velocity, $u_e(x)$, and displacement thickness, δ^*, are unknown quantities. Convergence is

58

ensured through the interaction law which uses the blowing velocity concept.

The equations are solved through successive sweeps over the airfoil surface as indicated in Figure 6.2. For each sweep the external velocity for the boundary layer equation is written

$$u_e(x) = u_{er}(x) + \delta u_e(x) \tag{6.2}$$

where,

$u_{er}(x)$ is the inviscid velocity

and

$u_e(x)$ is the perturbation velocity due to the boundary layer displacement.

The perturbation velocity is modeled by the interaction law with the help of blowing velocities. The displacement effect of ~ boundary layer is obtained by ejecting fluid at the surface of the airfoil as shown in Figure 6.3.

With a properly arranged blowing velocity source distribution on the airfoil surface, the virtual displacement body becomes a streamline.

In determining the source strengths, the displacement-body tangential flow condition is represented by

$$\frac{v(x,\delta^*)}{u_e(x)} = \frac{d\delta^*}{dx}. \tag{6.3}$$

59

START

INPUT of
1. Airfoil geometry
2. Angle of attack
3. Reynolds number

V_{wt}, δ^*

INVISCID FLOW SOLVER
Laplace equation is solved by a conformal mapping.
INPUT: Airfoil geometry and angle of attack displacement thickness distribution and blowing velocity distribution
OUTPUT: Velocity distribution u_{el} on displacement body

DATA INTERFACE
1. RELAXATION of the product term "$u_e \delta^*$"
2. Compute BLOWING VELOCITY distribution V_{wt}
3. Switch from b.l. grid to conformal mapping grid. Interpolate displacement thickness distribution and blowing velocity distribution at boundary points

u_{el}

DATA INTERFACE
Switch from conformal mapping to b.l. grid. Interpolate external velocity at b.l. points.

u_{el}

u_e, δ^*

VISCOUS FLOW SOLVER
Boundary layer equations are solved by a finite difference method.

DIRECT B.L. METHOD
(Used close to lead. edge)
INPUT: External velocity, initial guess of velocity profile
OUTPUT: Velocity profile and b.l. characteristics like displacement thickness δ^* and skin friction

INTERACTIVE B.L. METHOD
(Used anywhere else)
Both external velocity and displacement thickness are treated as unknowns.
INPUT: External velocity distribution and displacement thickness distribution of current (upstream) and previous (downstream) cycle, initial guess of velocity profile
OUTPUT: Velocity profile including the "viscous" external velocity u_e and b.l. characteristics like displ. thickness δ^* and skin friction

u_e, δ^*

CHECK CONVERGENCE
Compare 1. Viscous and inviscid external velocities
2. Displacement thickness of previous and current cycle
3. Product term "$u_e \delta^*$" of previous and current cycle

YES

NO

OUTPUT of
1. Pressure distribution
2. B.l. characteristics for both upper and lower surfaces
3. Velocity profiles if required

STOP

Figure 6.2   Viscid/Inviscid Interaction Method

60

Figure 6.3   The Blowing Velocity Concept

Model simplifications are achieved through the use of these thin airfoil approximations:

1) The u-velocity component is considered invariant across the boundary layer, as the displacement thickness is thin enough to consider the differences negligible.

2) The blowing velocity, $v(x,0)$, is one half the source strength, $\sigma(x)$, on an airfoil represented by a straight line.

$$\frac{\sigma(x)}{2} = (x,0)$$

$$= v(x,\delta^*) - \int_{o}^{\delta^*} \frac{\delta v}{\delta y} \, dy$$

$$= u_e \frac{d\delta^*}{\delta x} + \frac{du_e}{dx} \delta^*$$

$$\frac{\sigma(x)}{2} = \frac{d}{dx}(u_e \delta^*) \qquad (6.4)$$

where $(d/dx)(u_e\delta^*)$ is the blowing velocity.

The blowing velocity once obtained from the source strength is then related to the perturbation velocity, δu_e, through the use of the Hilbert integral.

$$\delta u_e = \frac{1}{2\pi} \int_{x_a}^{x_b} \frac{\sigma(\xi)}{x-\xi} \, d \qquad (6.5)$$

After substituting equations (6.4) and (6.5) into (6.2) the interaction law is obtained.

62

$$u_e(x) = u_{eI}(x) + \frac{1}{\pi} \int_{x_a}^{x_b} \frac{d}{d\xi}(u_e\delta^*)\frac{d\xi}{x-\xi} \qquad (6.6)$$

The numerical implementation of the interaction law requires some discrete approximation of the thin airfoil integral, equation (6.6). Similar to the panel method, a piecewise approximation of the continuous blowing velocity $d(u_e\delta^*)/dx$ allows for piecewise analytical integration.

VII. AIRFOIL STUDIES

Cebeci's interactive aircode was applied to four airfoils over a wide range of Reynolds numbers and angles of attack. The computer program results were then compared to reported experimental data. Unless otherwise stated, 20 iterations were used for each computer run, and laminar-to-turbulent transitions were determined internal to the program. The significance of the number of iterations will be discussed later in the section.

A. NACA 66_3-018

Computer results of the NACA 66_3-018 airfoil section were compared to the test results of Gault [Ref. 8], which were performed in the NASA Ames Research Center 7-by-10-foot wind tunnel. The laminated pine model with a 1/8 inch-thick mahogany plywood veneer spanned the 7-foot dimension to simulate two-dimensional flow.

Total-and static-pressure surveys, hot-wire-anemometer observations, and detailed pressure-distribution and liquid-film measurements were made in regions of separated flow. The measurements were obtained for a wide range of angles of attack and for Reynolds numbers from 1.5 to 10 million. A main purpose of these measurements was to identify locations of separation, transition and reattachment.

Using the Cebeci Code the 66_3-018 airfoil shown in Figure 7.1 was initially tested for section lift coefficients. Comparisons were made with Abbott and Doenhoff [Ref. 9] and the results are presented in Figures 7.2 and 7.3 for Reynolds numbers of 3 and 6 million, respectively.

Upper surface, laminar to turbulent, transition locations are shown in Figures 7.4 and 7.5 for increasing angles of attack and for Reynolds numbers of 3 and 6 million, respectively. Gault's locations were obtained from pressure and hot-wire measurements, which provided near identical results. The program transition locations were computed to be the point of laminar separation. Note that the transition locations shift forward as the angle of attack is increased, and they approach the leading edge above 6 degrees. Unless otherwise stated, all computer runs used a transition constant of GY = 1200.

Midchord upper surface transitions at less than two degrees angle of attack and Reynolds numbers of 1.5 to 10 million are shown in Figures 7.6, 7.7, 7.8 and 7.9. In all cases the computed predictions were forward of Gault's because of laminar separation predicted by the Code.

While Gault found leading edge separation bubbles, the Cebeci Code did not predict them at any angle of attack for Reynolds numbers of 3 and 6 million.

The relationships between separation and transition are illustrated in Figure 7.10 for the results of Gault and the

NACA 663-018
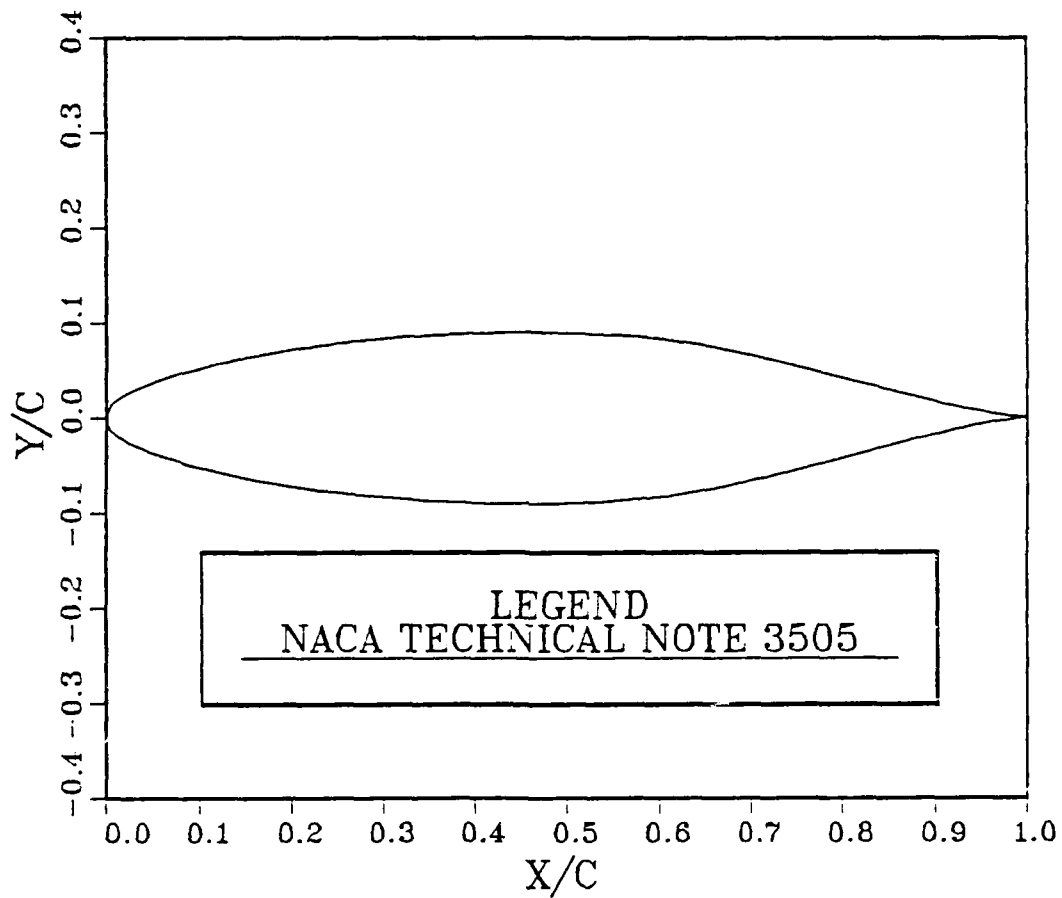
Figure 7.1   NACA 66₃-018 Airfoil

LIFT COEFFICIENT
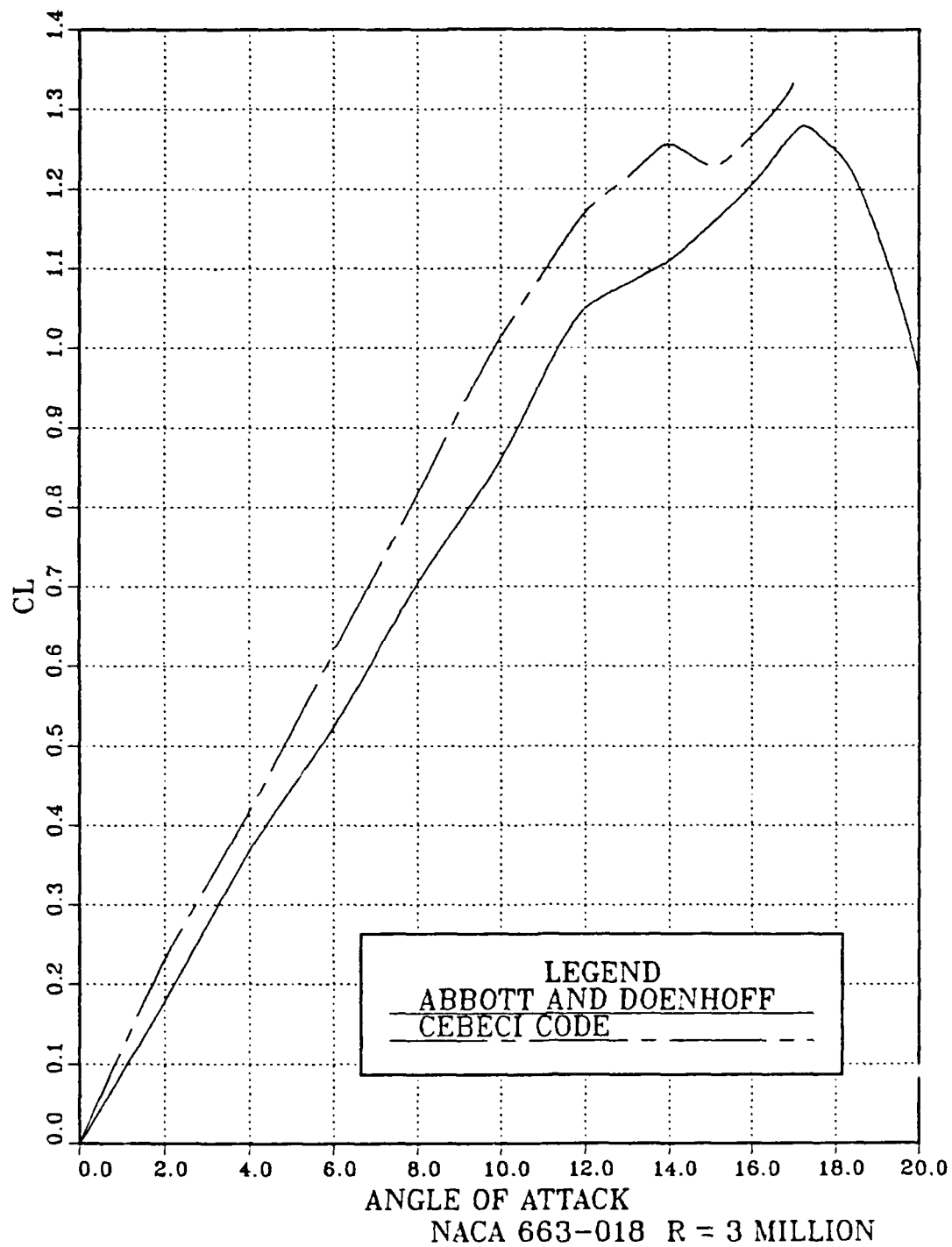
Figure 7.2   Lift Coefficient, NACA 66₃-018, R = 3 Million

67

LIFT COEFFICIENT

NACA 663-018 R = 6 MILLION
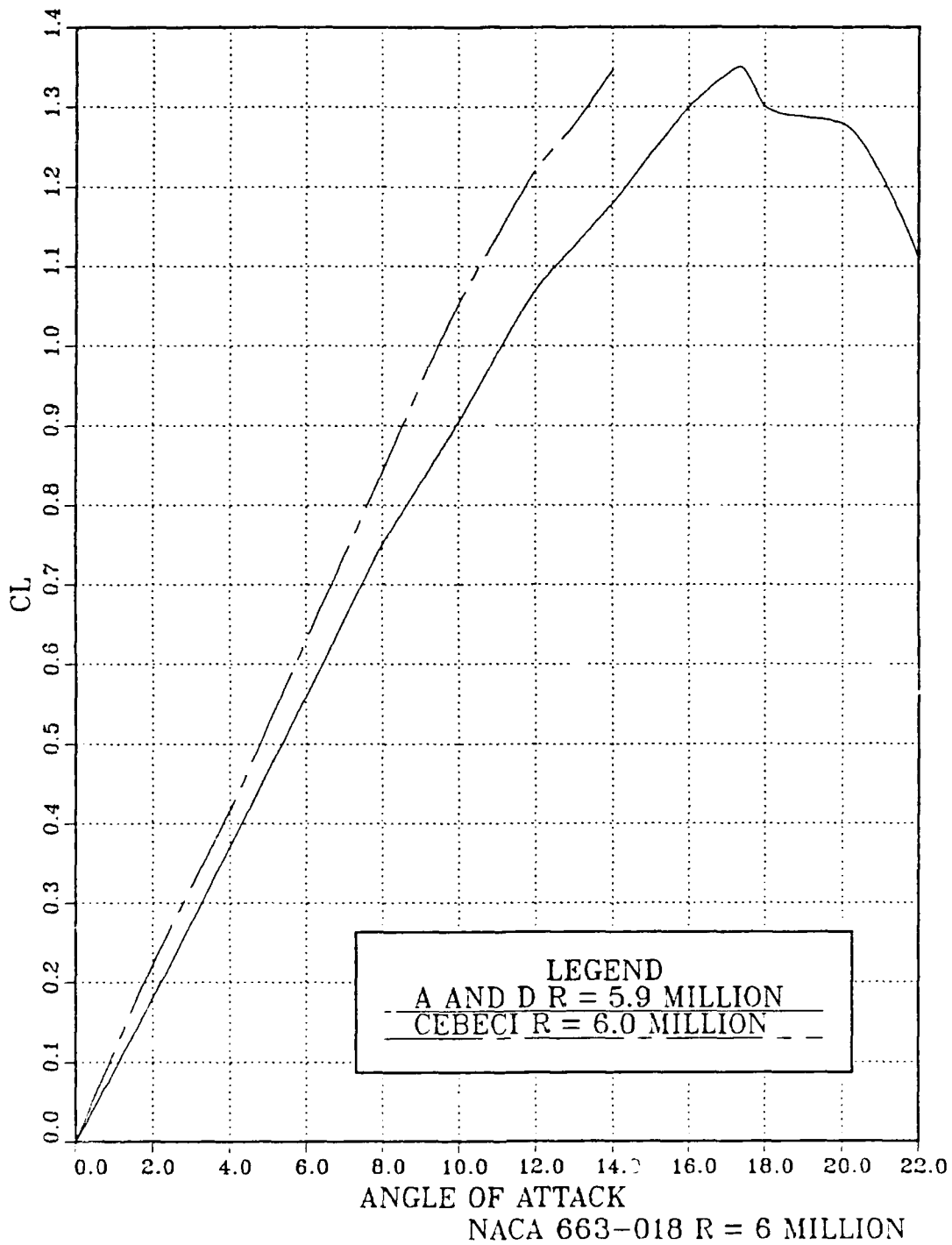
Figure 7.3   Lift Coefficient, NACA 66₃-018, R = 6 Million

68

LAMINAR TO TURBULENT TRANSITION

Figure 7.4   Upper Surface Laminar to Turbulent
             Transition, NACA 66_3-018, R = 3 Million

LAMINAR TO TURBULENT TRANSITION

NACA 663-018, R = 6.0 MILLION
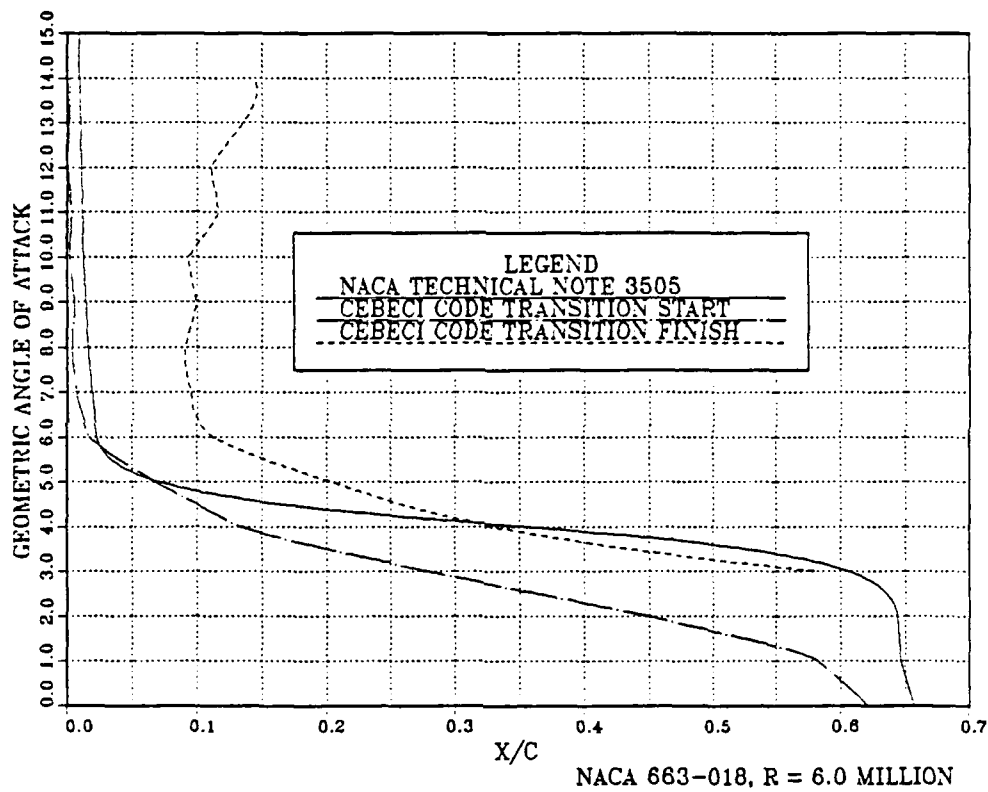
Figure 7.5   Upper Surface Laminar to Turbulent
              Transition, NACA 66₃-013, R = 6 Million

70

UPPER SURFACE TRANSITION
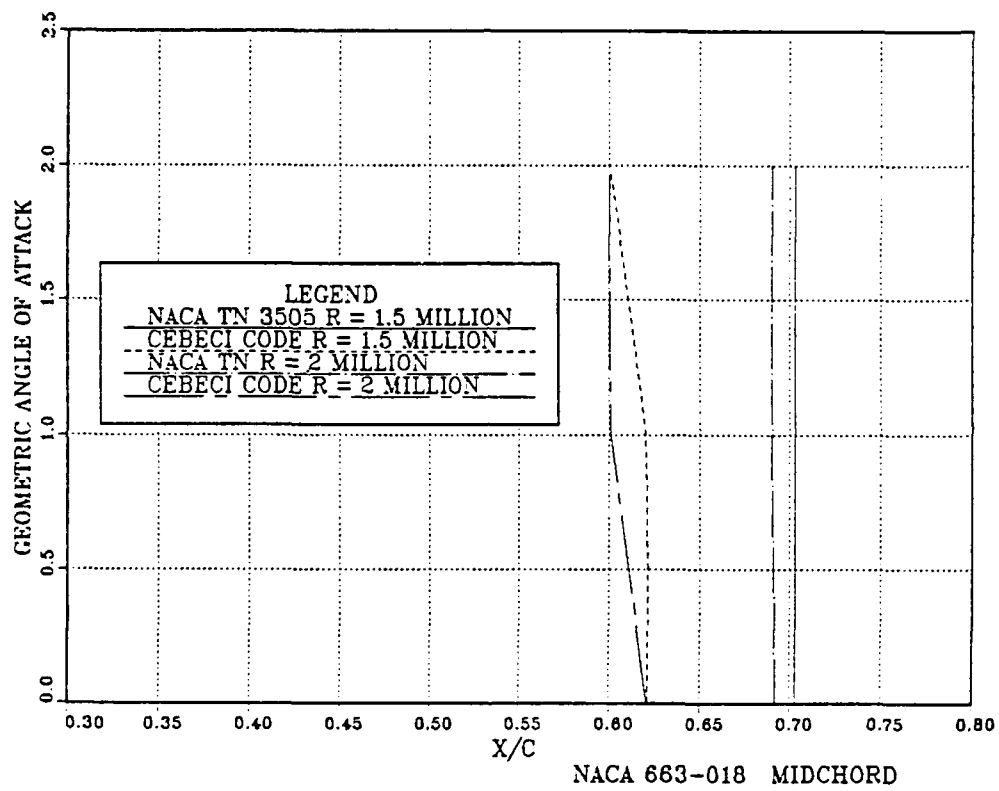
Figure 7.6   Upper Surface Transition, Midchord, NACA
               66_3-018, R = 1.5 and 2 Million

UPPER SURFACE TRANSITION
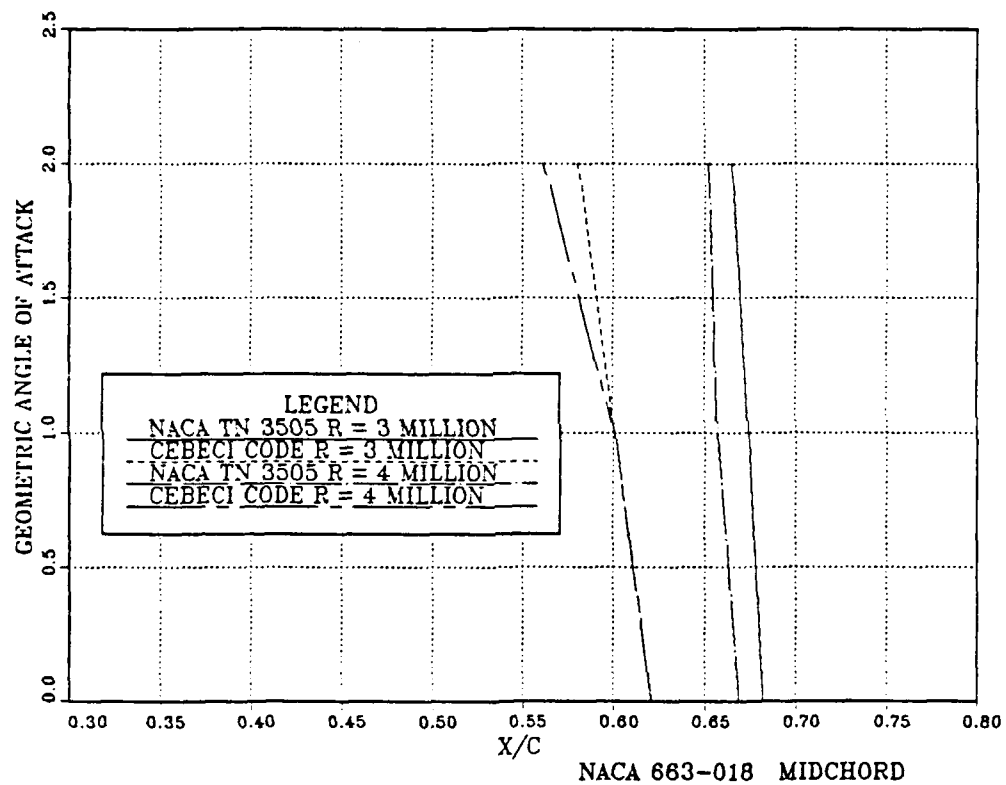
Figure 7.7   Upper Surface Transition, Midchord, NACA
              66_3-018, R = 3 and 4 Million

UPPER SURFACE TRANSITION

NACA 663-018   MIDCHORD
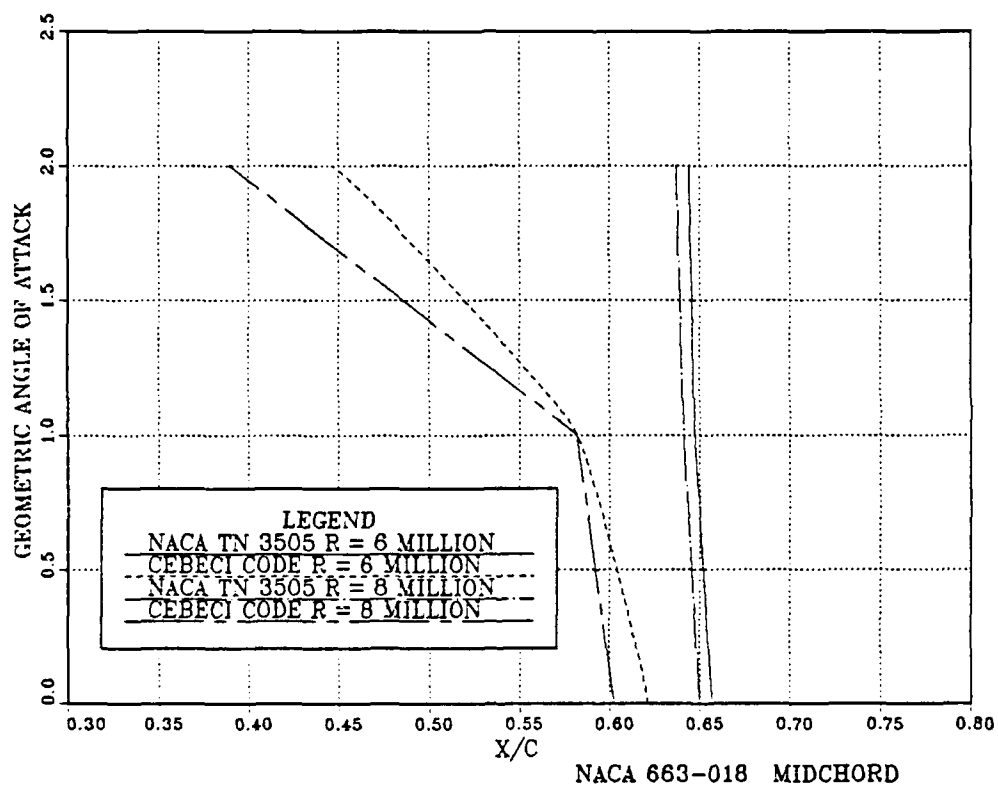
Figure 7.8   Upper Surface Transition, Midchord, NACA
66₃-J18, R = 6 and 8 Million

UPPER SURFACE TRANSITION

NACA 663-018 MIDCHORD
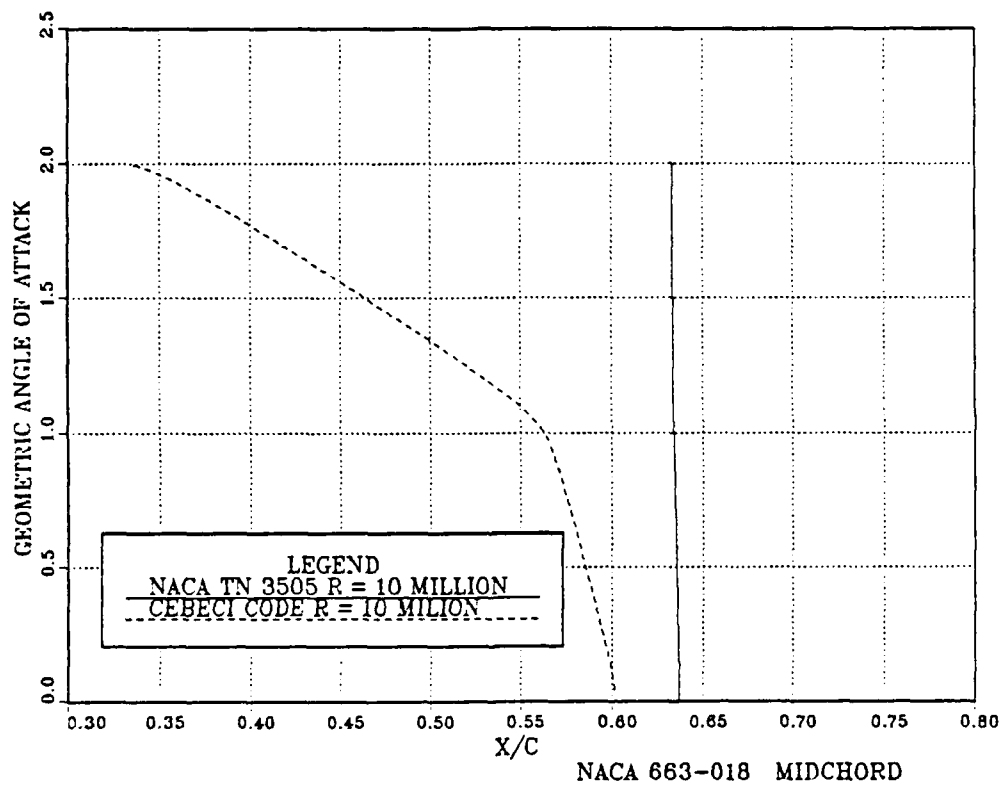
Figure 7.9   Upper Surface Transition, Midchord, NACA
66₃-018, R = 10 Million

UPPER SURFACE TRANSITION

663-018 MIDCHORD R = 2 MILLION
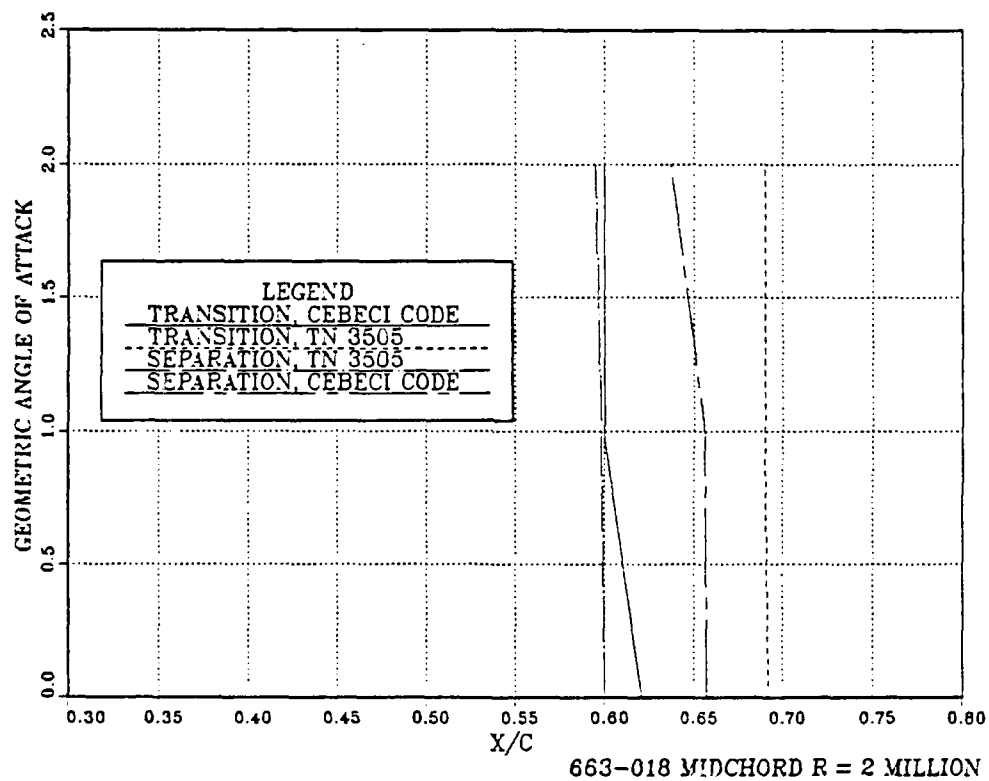
Figure 7.10 Upper Surface Transition and Separation,
            Midchord, NACA 66_3-018, R = 2 Million

75

Cebeci code. The experimental results show separation prior to transition, whereas the computer results predict separation after transition. The importance of this difference manifests itself in the difference between the measured and computed midchord bubbles, pressure distributions and velocity profiles shown in Figures 7.11 to 7.31.

Midchord separation bubbles for angles of attack of 0 and 2 degrees and Reynolds number of 2 million are plotted in Figures 7.11 and 7.12. The lines represent contours where u/u_e = 0. The Cebeci Code midchord bubbles are much smaller than those found by Gault.

Full chord pressure distributions for angles of attack of zero and two degrees, and Reynolds numbers of three and six million are shown in Figures 7.13 to 7.16. In each case the biggest difference between the experimental results and the Cebeci code occurred near the midchord separation bubble regions. Figure 7.17 shows a leading edge pressure distribution for an angle of attack of six degrees and a Reynolds number of three million.

Midchord velocity profiles are shown in Figures 7.18 through 7.24 for an angle of attack of zero degrees and a Reynolds number of two million, and in Figures 7.25 through 7.31 for two degrees angle of attack and a Reynolds number of two million. These velocity profil.s clearly show a big difference in bubble sizing.

76

MIDCHORD BUBBLE SHAPE

NACA 663-018, AOA=0, R=2 MILLION
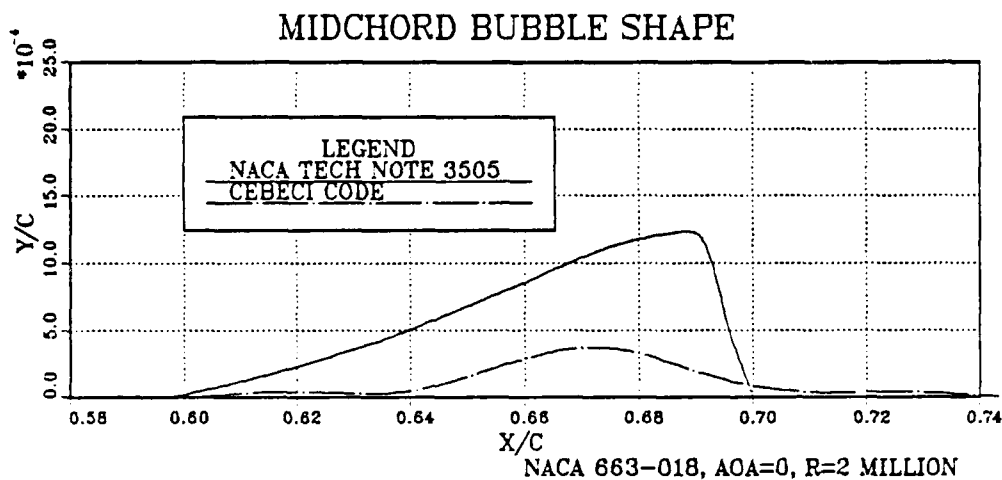
Figure 7.11 Midchord Bubble Shape, NACA 66_3-018,
AOA = 0°, R = 2 Million

MIDCHORD BUBBLE SHAPE

NACA 663-018, AOA=2, R=2 MILLION
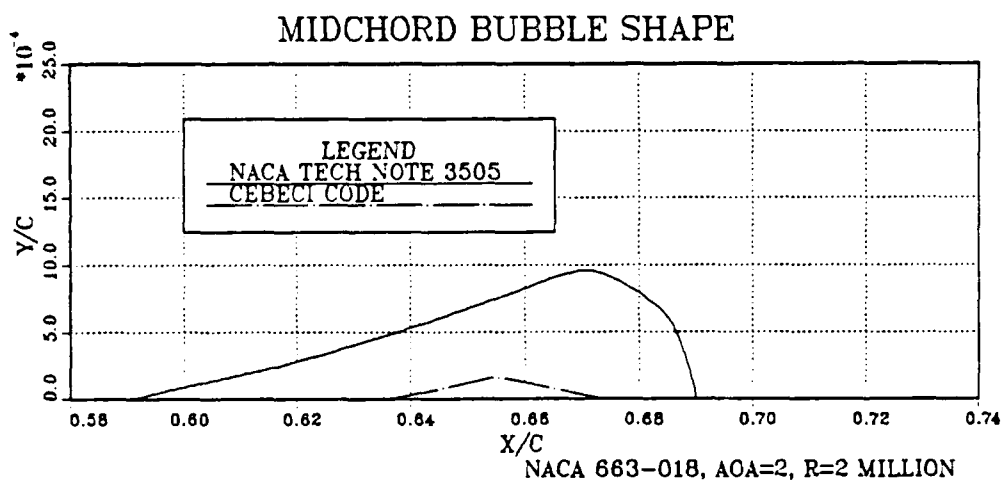
Figure 7.12 Midchord Bubble Shape, NACA 66_3-018,
AOA = 2°, R = 2 Million

77

UPPER SURFACE PRESSURE

NACA 663-018 AOA=0 R=3 MILLION
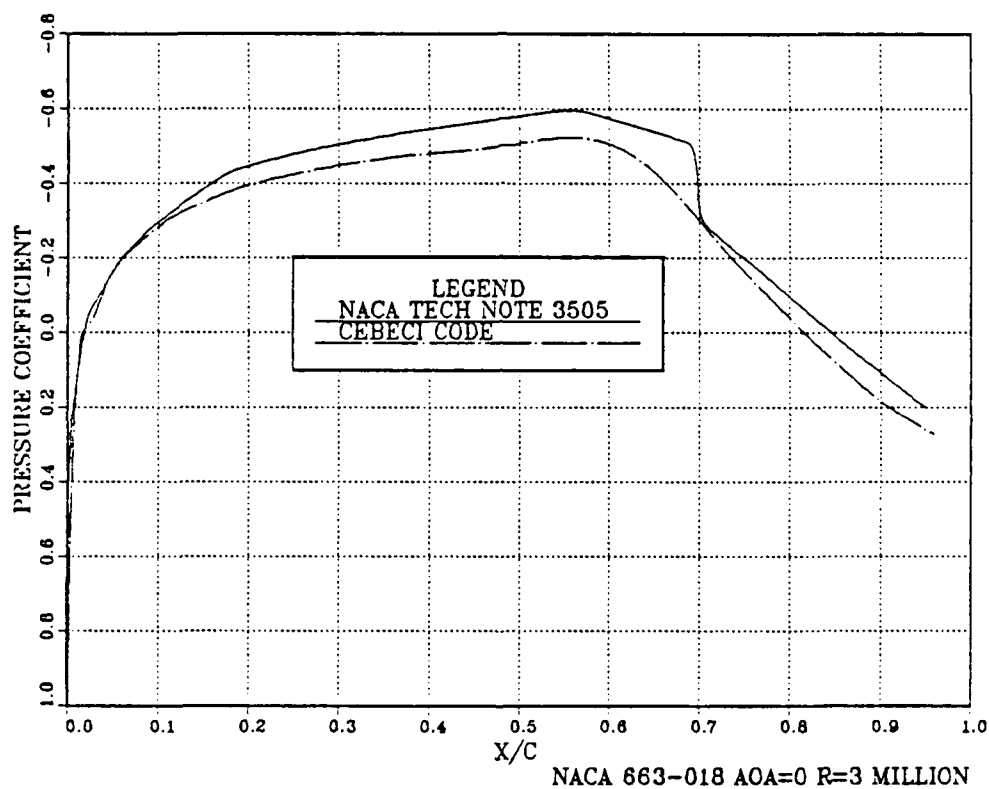
Figure 7.13   Upper Surface Pressure Distribution, NACA
66$_3$-018, AOA = 0°, R = 3 Million

UPPER SURFACE PRESSURE

NACA 663-018 AOA=0 R=6 MILLION
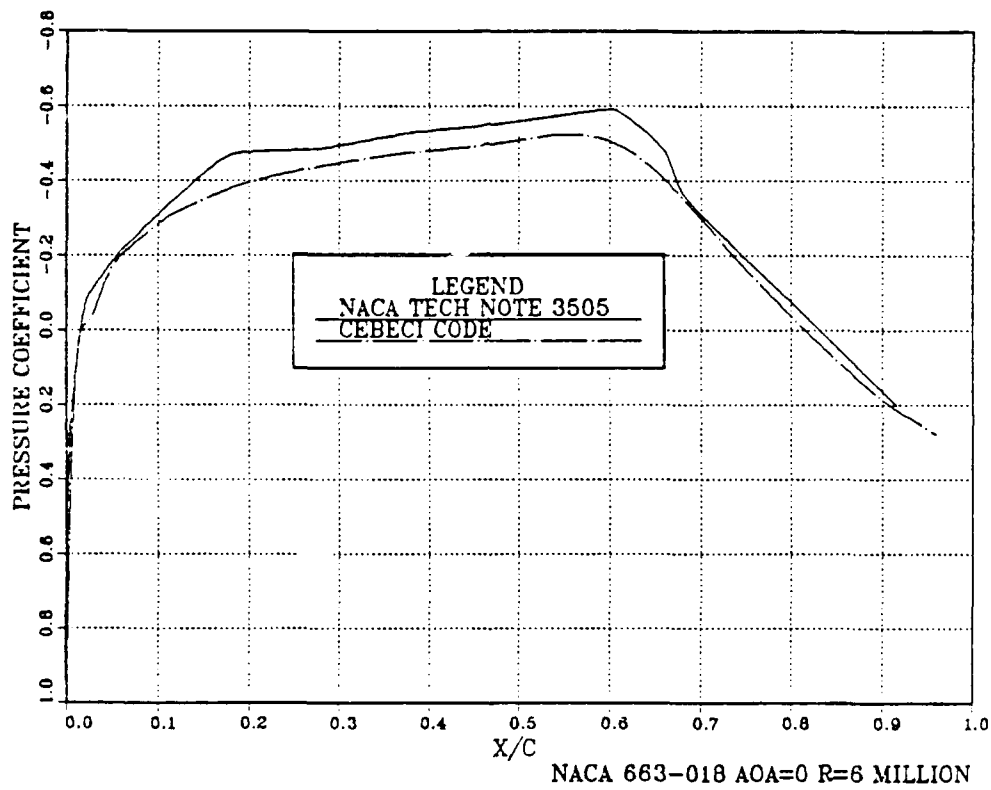
Figure 7.14   Upper Surface Pressure Distribution, NACA
66₃-018, AOA = 0°, R = 6 Million

UPPER SURFACE PRESSURE

NACA 663-018 AOA=2 R=3 MILLION
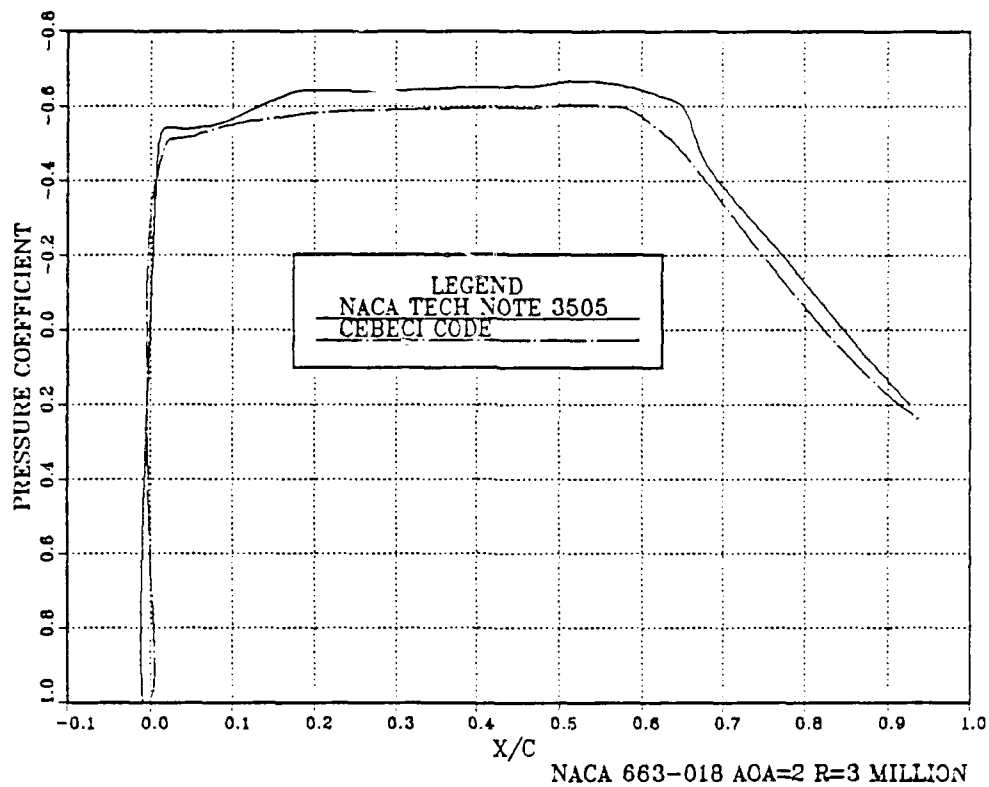
Figure 7.15   Upper Surface Pressure Distribution, NACA
66$_3$-018, AOA = 2°, R = 3 Million

UPPER SURFACE PRESSURE

NACA 663-018 AOA=2 R=6 MILLION
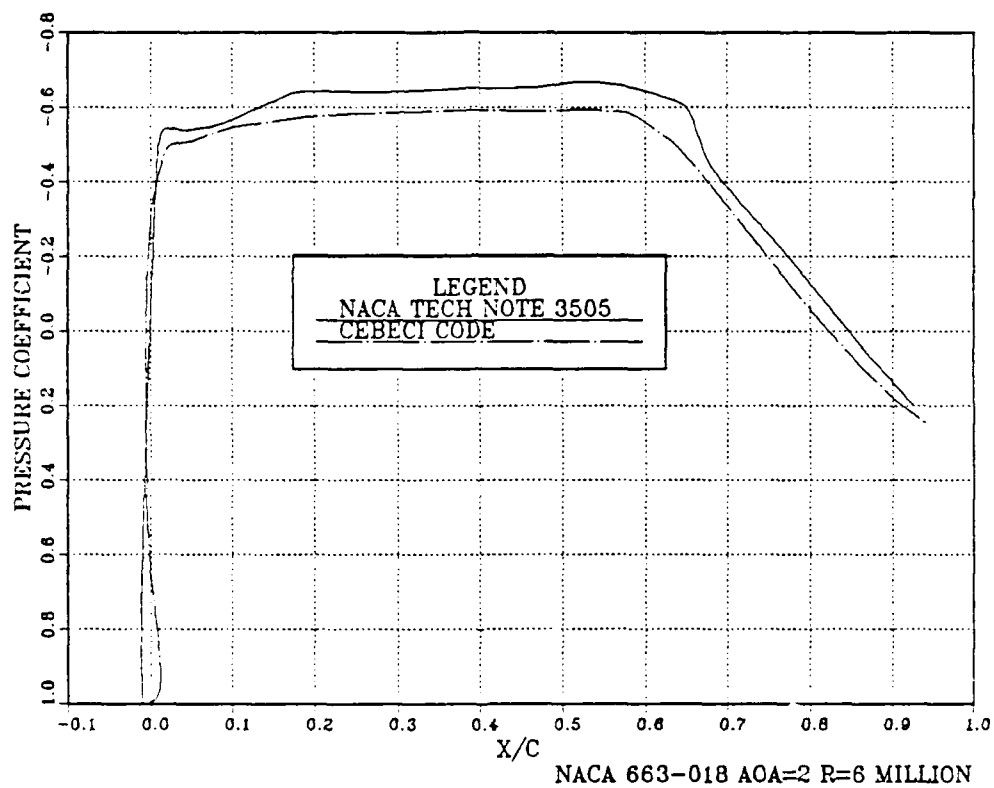
Figure 7.16   Upper Surface Pressure Distribution, NACA
66_3-018, AOA = 2°, R = 6 Million

UPPER SURFACE PRESSURE

NACA 663-018 AOA=6 R=3 MILLION
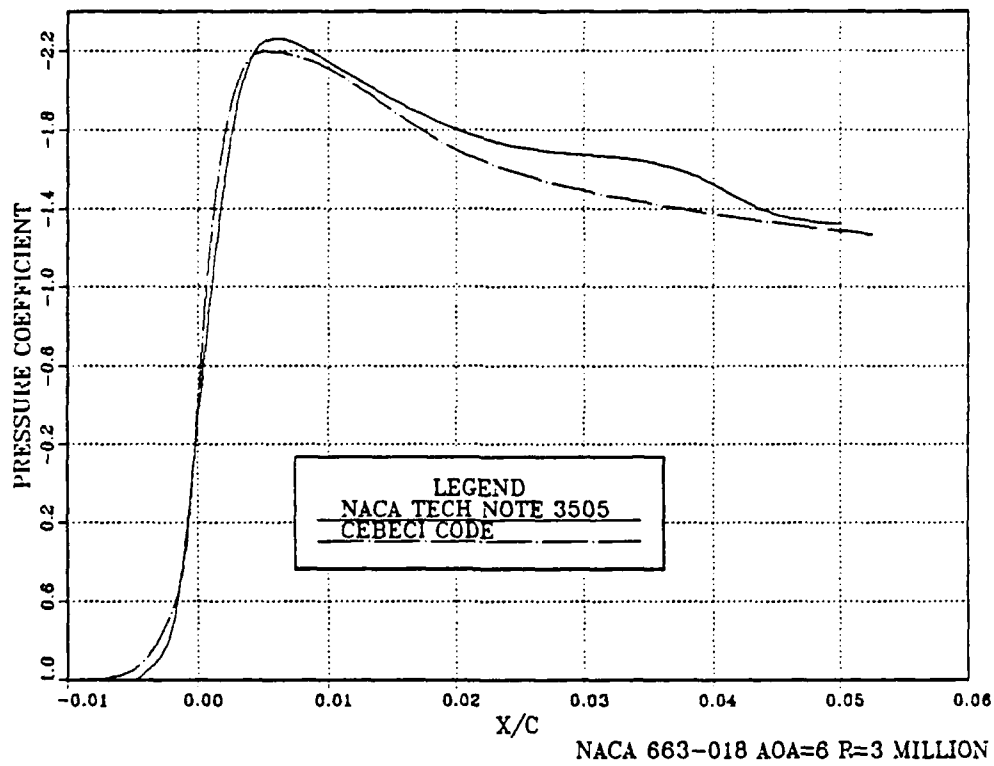
Figure 7.17   Leading Edge Upper Surface Pressure
                Distribution, NACA 66_3-018, AOA = 6°,
                R = 3 Million

VELOCITY PROFILES
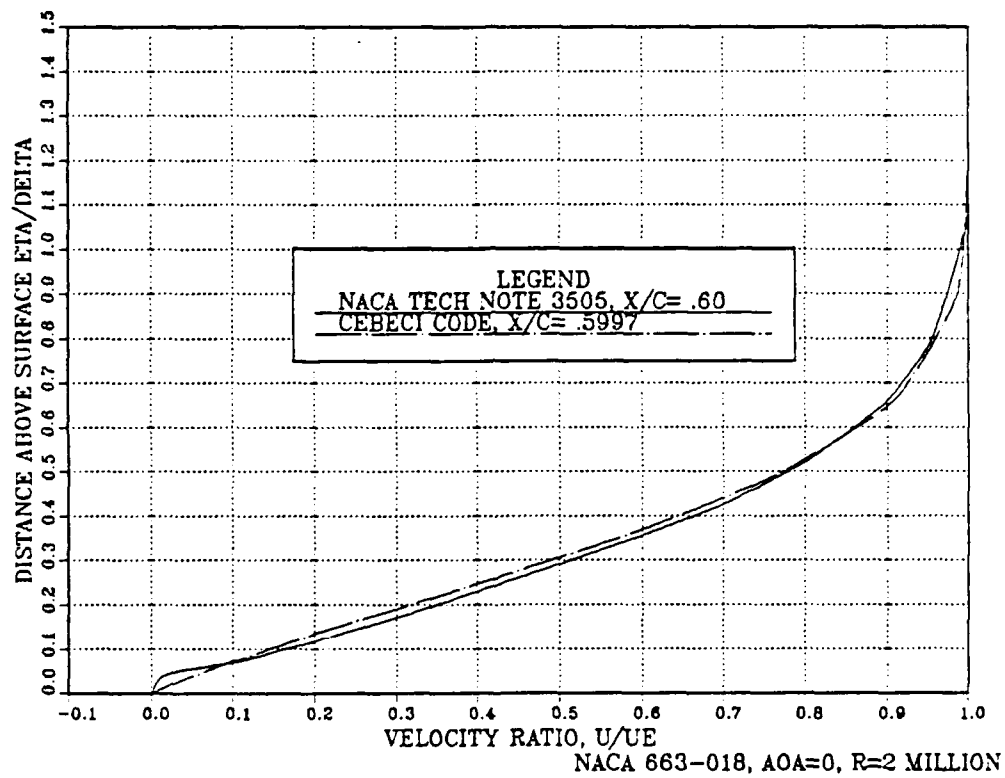
Figure 7.18   Upper Surface Velocity Profile, NACA 66_3-018,
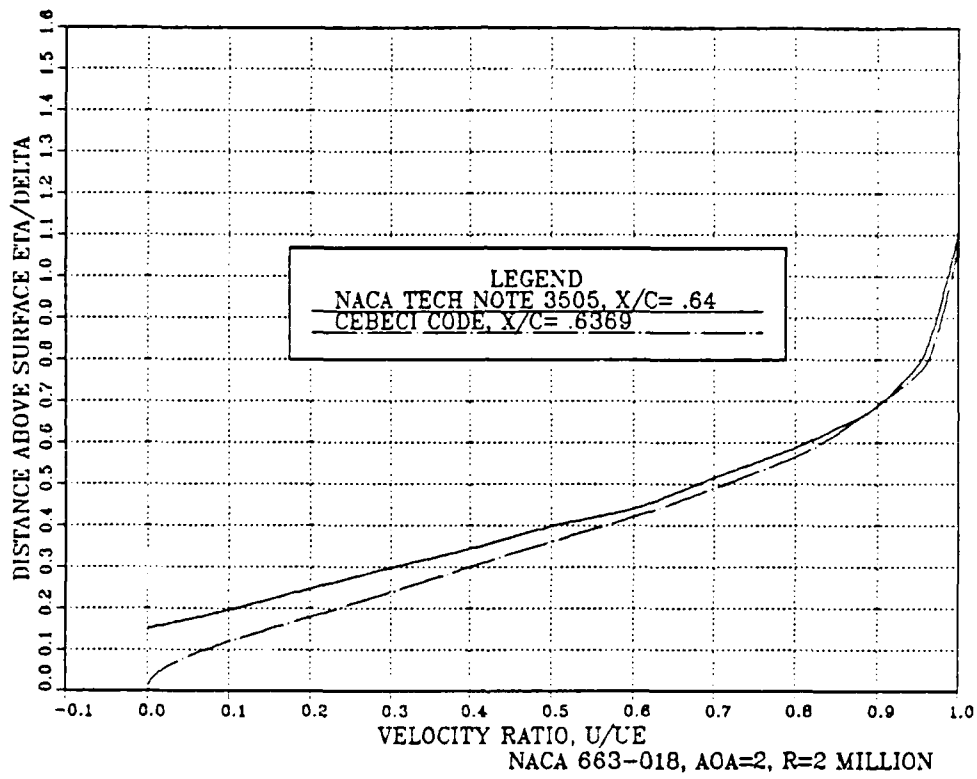X/C = .60, AOA = 0°, R = 2 Million

83
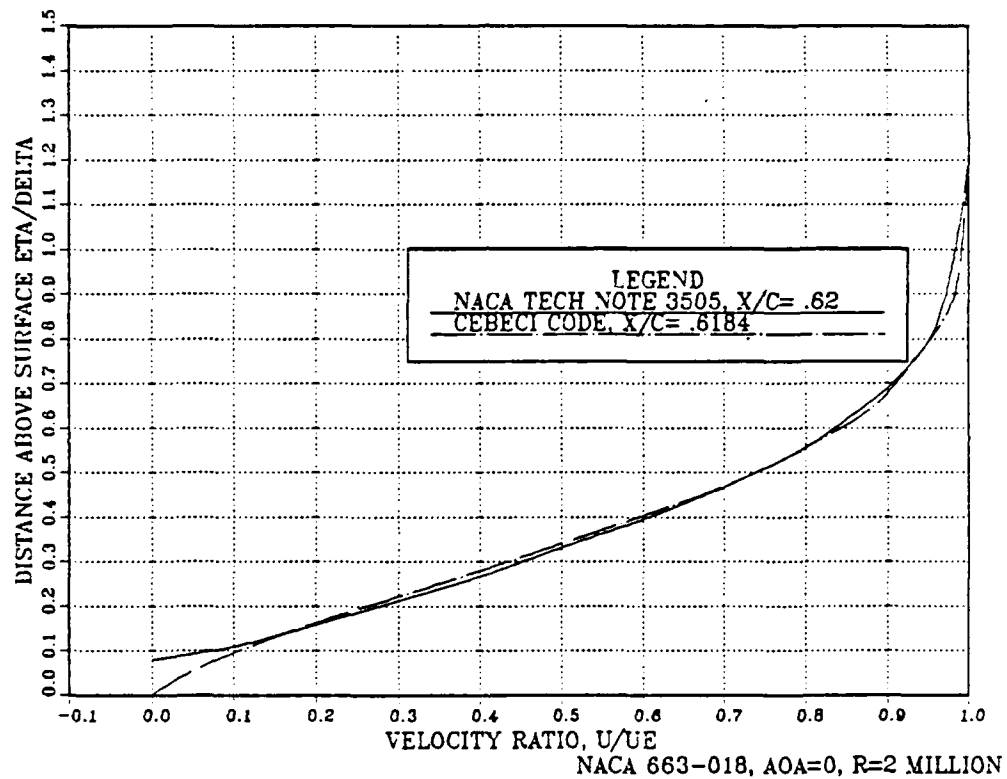
VELOCITY PROFILES
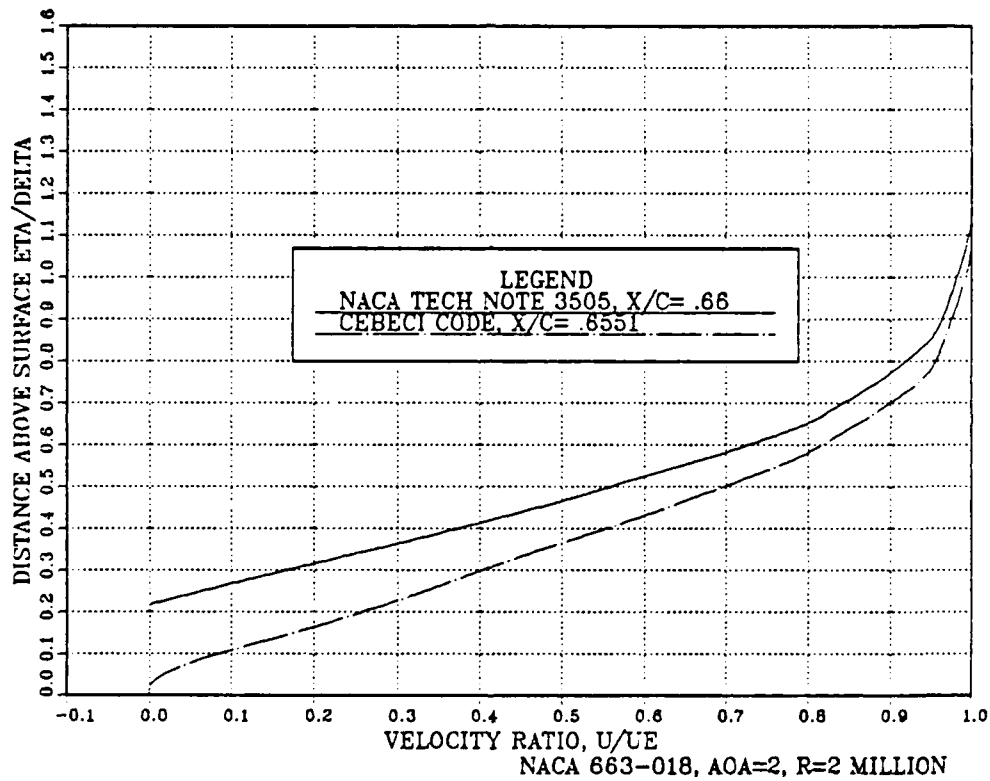

Figure 7.19   Upper Surface Velocity Profile, NACA 66₃-018, X/C = .62, AOA = 0°, R = 2 Million

VELOCITY PROFILES
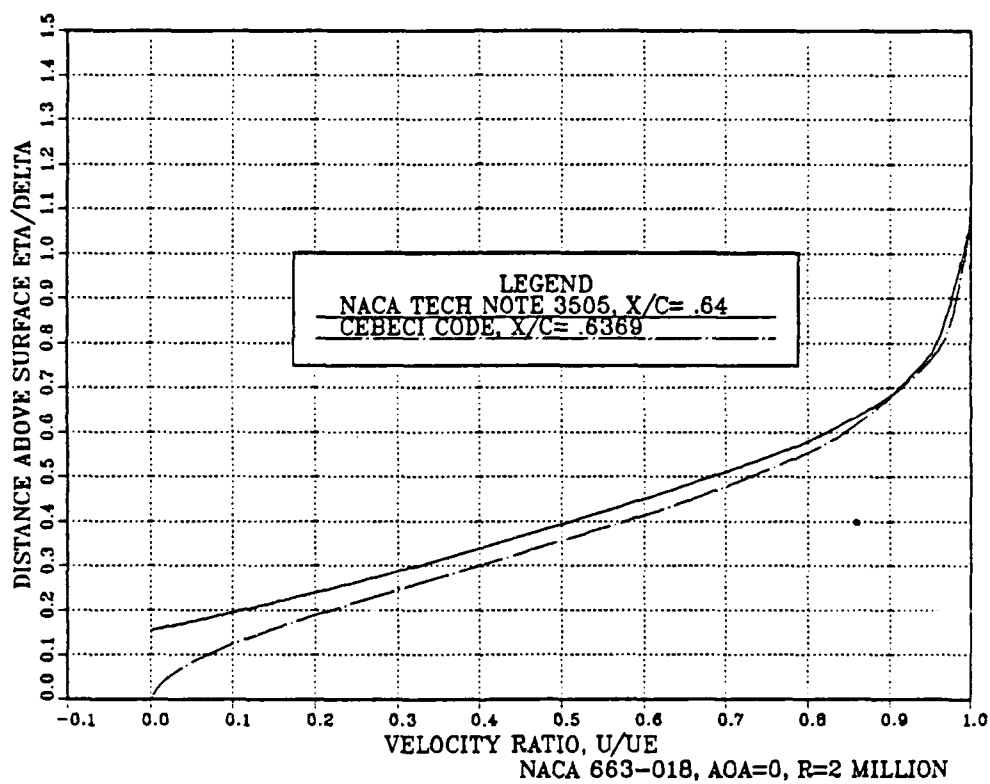
Figure 7.20 Upper Surface Velocity Profil
X/C = .64, AOA = 0°, R = 2 Million

VELOCITY PROFILES
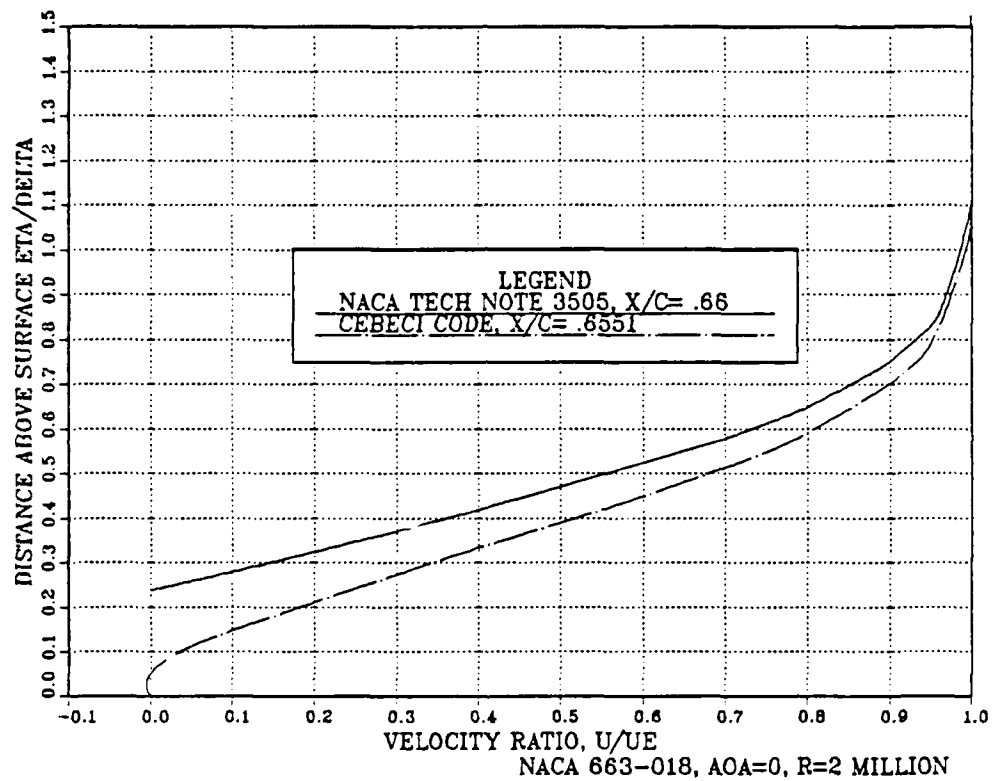
Figure 7.21   Upper Surface Velocity Profile, NACA 66$_3$-018,
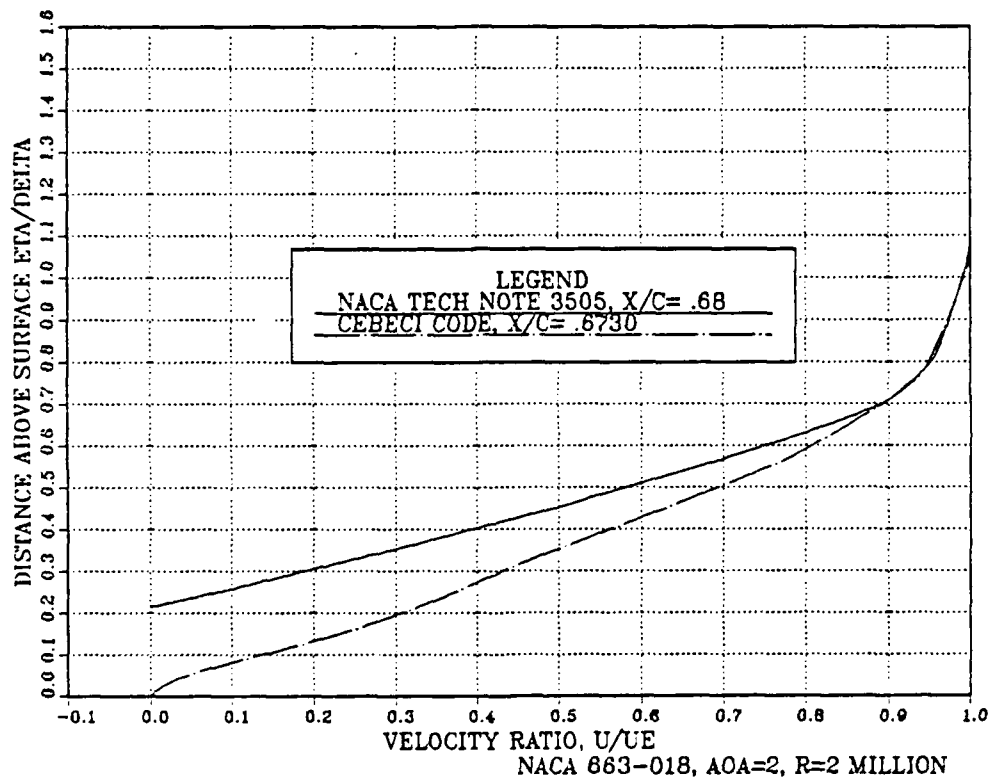X/C = .66, AOA = 0°, R = 2 Million

VELOCITY PROFILES
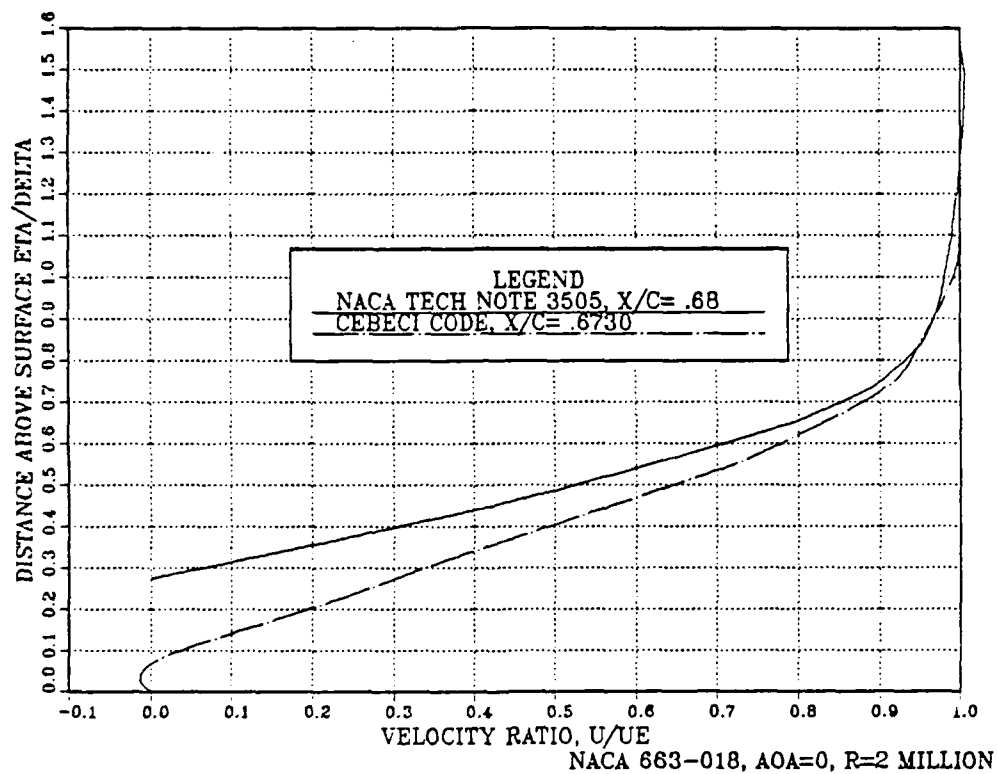
Figure 7.22   Upper Surface Velocity Profile, NACA 66₃-018,
X/C = .68, AOA = 0°, R = 2 Million

87

VELOCITY PROFILES

NACA 663-018, AOA=0, R=2 MILLION
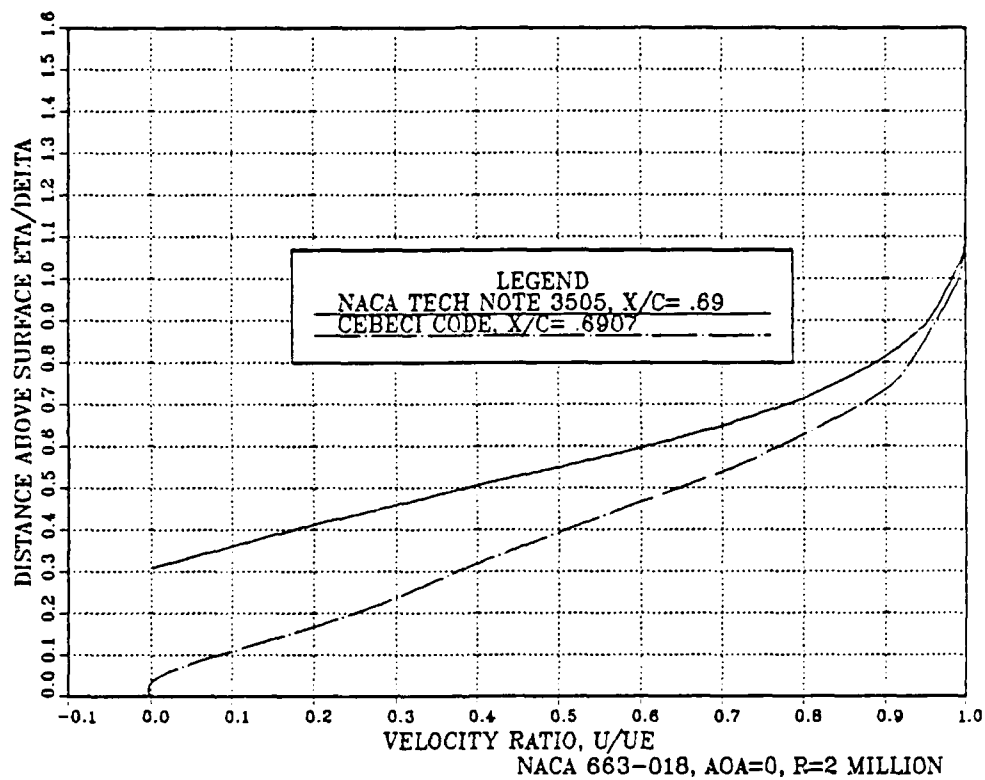
Figure 7.23   Upper Surface Velocity Profile, NACA 66₃-018,
X/C = .69, AOA = 0°, R = 2 Million

VELOCITY PROFILES
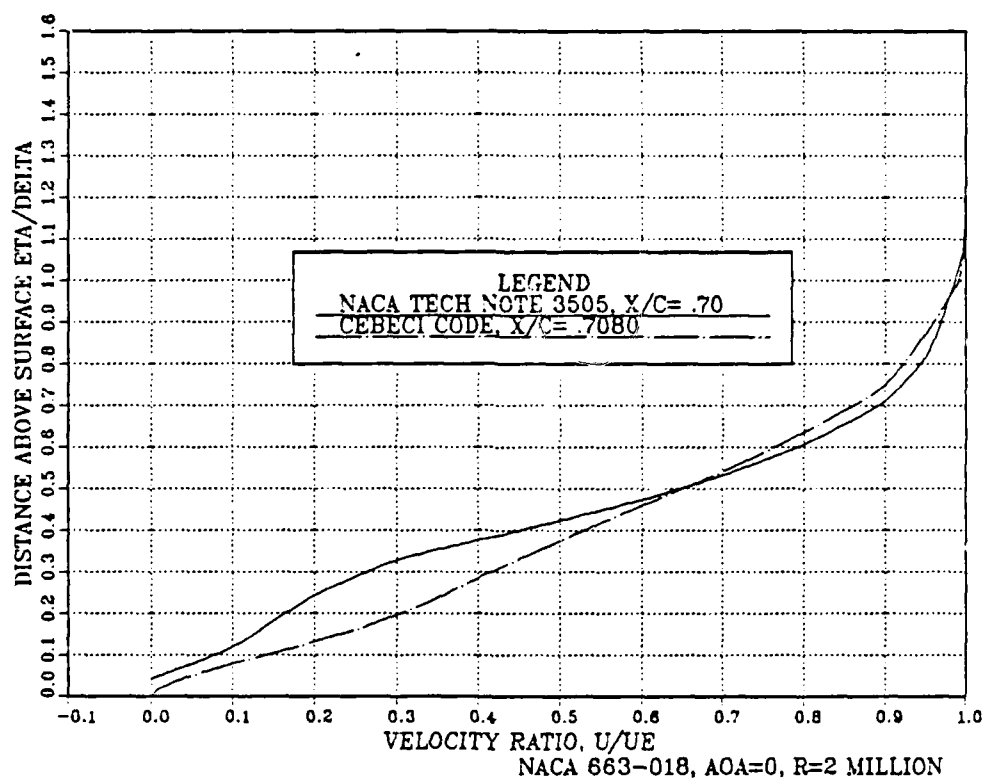
Figure 7.24   Upper Surface Velocity Profile, NACA 66_3-018, X/C = .70, AOA = 0°, R = 2 Million

VELOCITY PROFILES
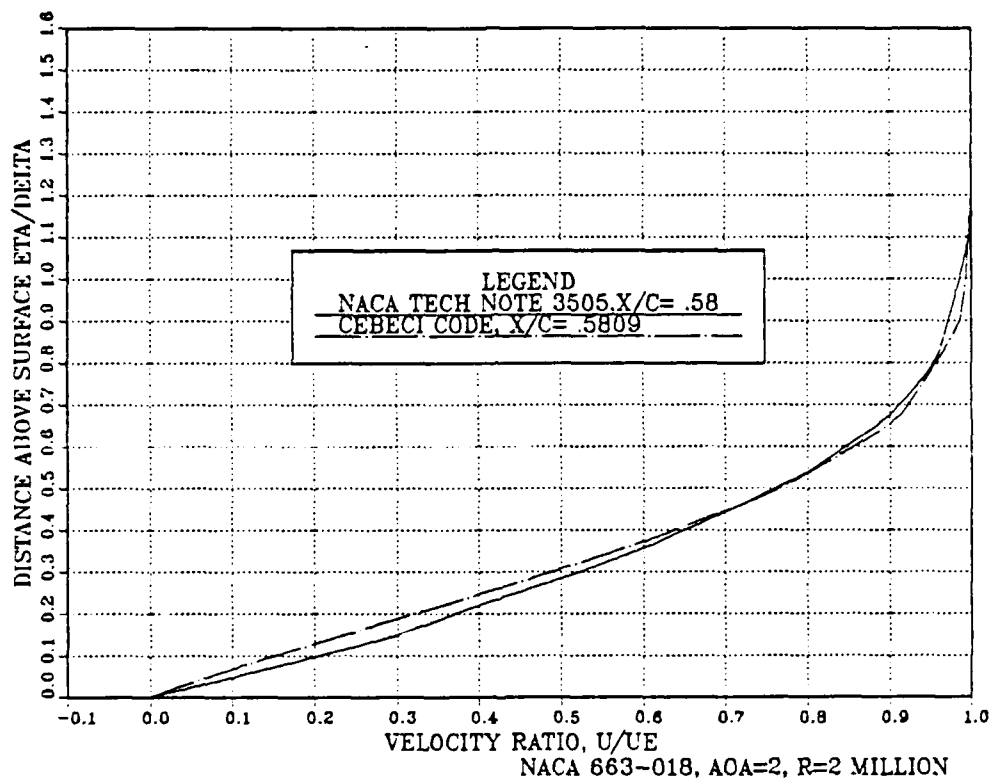
Figure 7.25   Upper Surface Velocity Profile, NACA 66₃-018,
              X/C = .58, ACA = 2°, R = 2 Million

90

VELOCITY PROFILES

NACA 663-018, AOA=2, R=2 MILLION
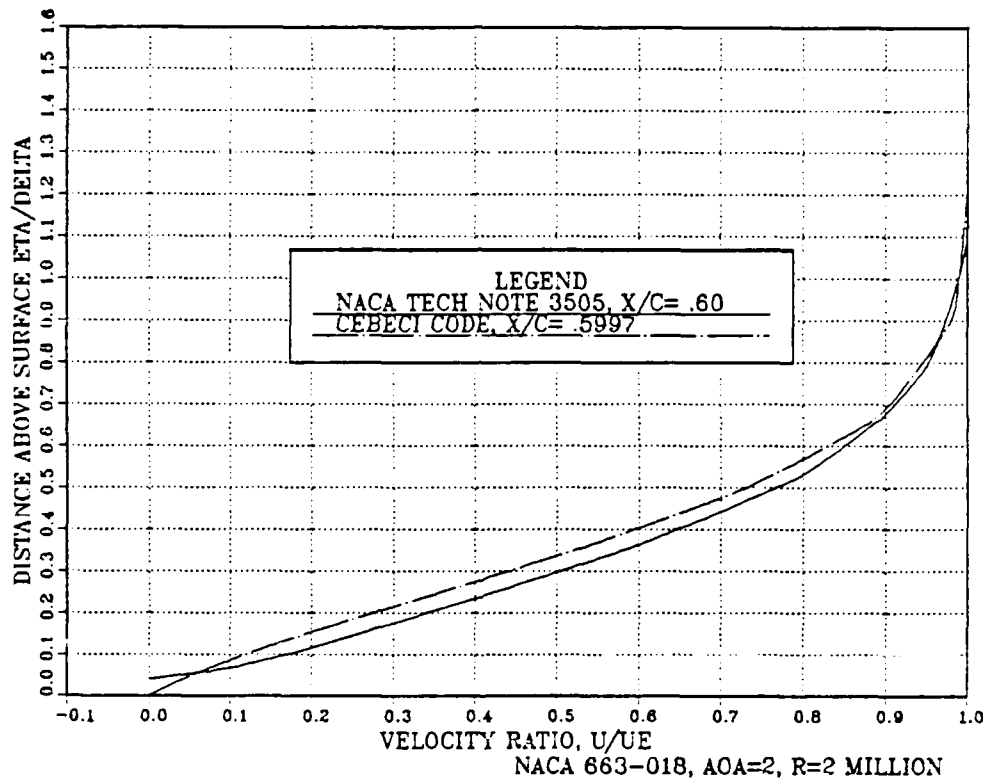
Figure 7.26 Upper Surface Velocity Profile, NACA 66₃-018,
X/C = .60, AOA = 2°, R = 2 Million

VELOCITY PROFILES
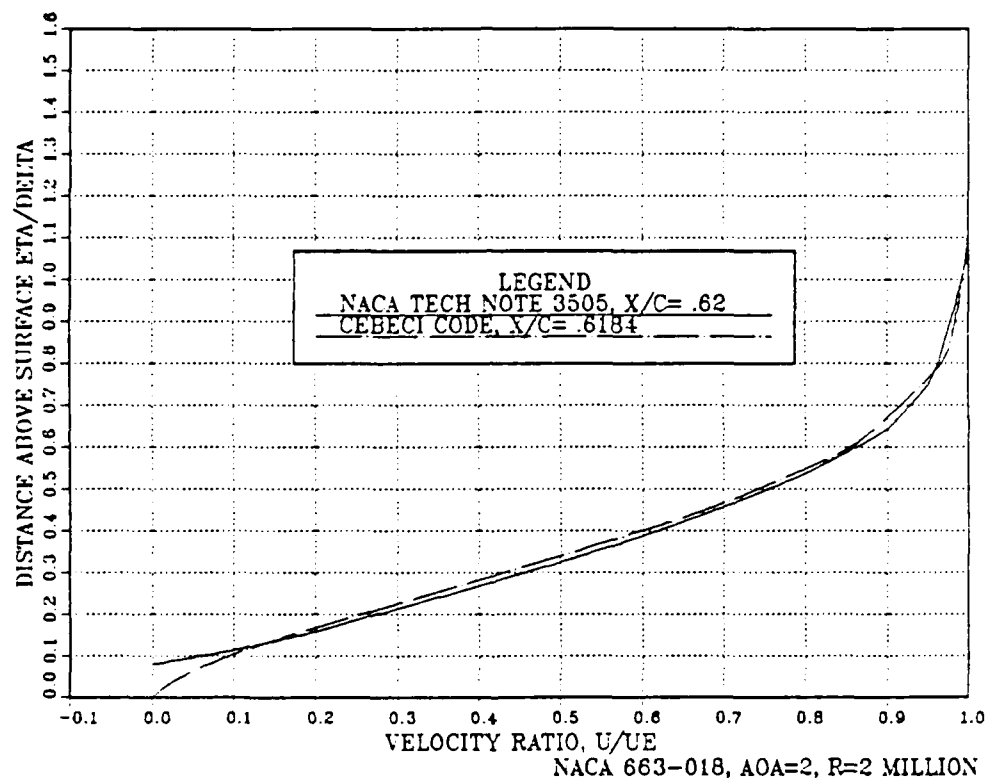
Figure 7.27   Upper Surface Velocity Profile, NACA 66₃-018,
              X/C = .62, ACA = 2°, R = 2 Million

VELOCITY PROFILES

Figure 7.28 Upper Surface Velocity Profile, NACA 66_3-018, X/C = .64, AOA = 2°, R = 2 Million

VELOCITY PROFILES

NACA 663-018, AOA=2, R=2 MILLION

Figure 7.29   Upper Surface Velocity Profile, NACA 66₃-018,
              X/C = .66, AOA = 2°, R = 2 Million

VELOCITY PROFILES

Figure 7.30   Upper Surface Velocity Profile, NACA 66_3-018,
X/C = .68, AOA = 2°, R = 2 Million

VELOCITY PROFILES
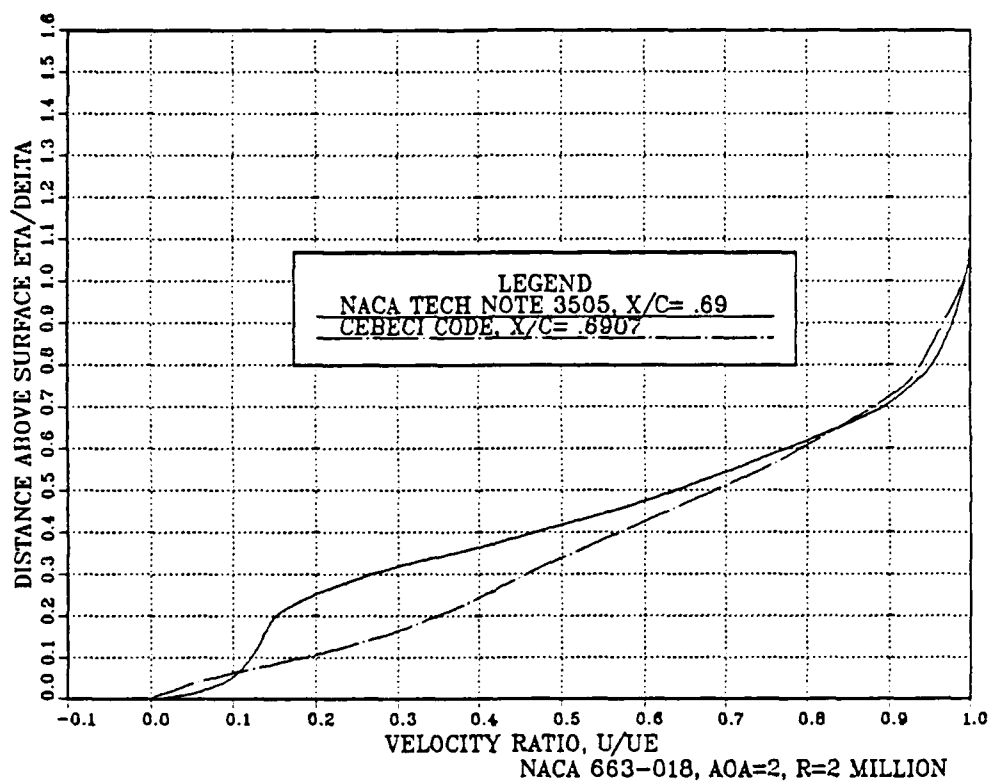
Figure 7.31   Upper Surface Velocity Profile, NACA 66_3-018, X/C = .69, AOA = 2°, R = 2 Million

In an effort to increase the region of separated flow, both the GY transition constant and the location of upper surface transition were adjusted. Table 7.1 shows theresults. With a constant of 1200 the transition location could not be moved aft. However, when the constant was lowered to 200 and below, the transition location, $x/c = .69$, found by Gault, could be used moving the transition inside the bubble. While a lowered GY_{tr} constant and increased x/c transition improved the bubble size, the separation length, $x/c = .60$ to .70, could not quite be met. The best result, bubble = .6391 - .7098 (x/c), was obtained with a GY_{tr} of 40, and an upper surface transition location, XTRU, input of .69 (x/c). Whether 40 is a suitable value for other foils has not been determined.

Twenty iterations were used on all computer runs for this airfoil. To make sure that 20 iterations were sufficient for accurate results, Figure 7.32 was obtained. The lift coefficient was plotted for each iteration, and as can be seen the even iterations produced very minimal changes past 12. Even between 19 and 20 the change in lift was only 5×10^{-4}. Therefore, 20 iterations were considered sufficient for all computer runs.

B. NACA 0010 (MODIFIED)

Similar to the NACA 66_3-018, computer results of the NACA 0010 (Modified) airfoil section were compared to the test results of Gault [Ref. 8]. The tests were also conducted in

97

TABLE 7.1   EFFECT OF GYTR AND XTRU ON THE LENGTH OF THE SEPARATION BUBBLE

GYTR	XTRU (X/C)	SEPARATION (X/C)
1200	.620792 (1)	.6572 - .6929
	.65	(2)
	.69	(2)
400	.69	(2)
300	.69	(2)
200	.69	.6391 - .7596
120	.639164 (1)	No Separation
	.65	.6572 - .6751
	.69	.6391 - .7434
80	.69	.6391 - .7268
60	.69	.6391 - .7268
40	.69	.6391 - .7098
30	.69	.6572 - .7098
20	.69	.6572 - .7098
10	.69	.6572 - .7098

NACA 663-018

Reynolds Number = 2,000,000
Angle of Attack = 0 Degrees

Region of Separation, Experimental (Gault) = .60 - .70 (x/c)

GYTR = Empirical Transition Constant

XTRU = Upper Surface Begin of Transition, Input   or Computer
Derived

Lower Surface Begin of Transition = Computer Derived, Each
Case

1) Computer Derived

2) Breakdown in Simulation

LIFT COEFFICIENT ITERATIONS
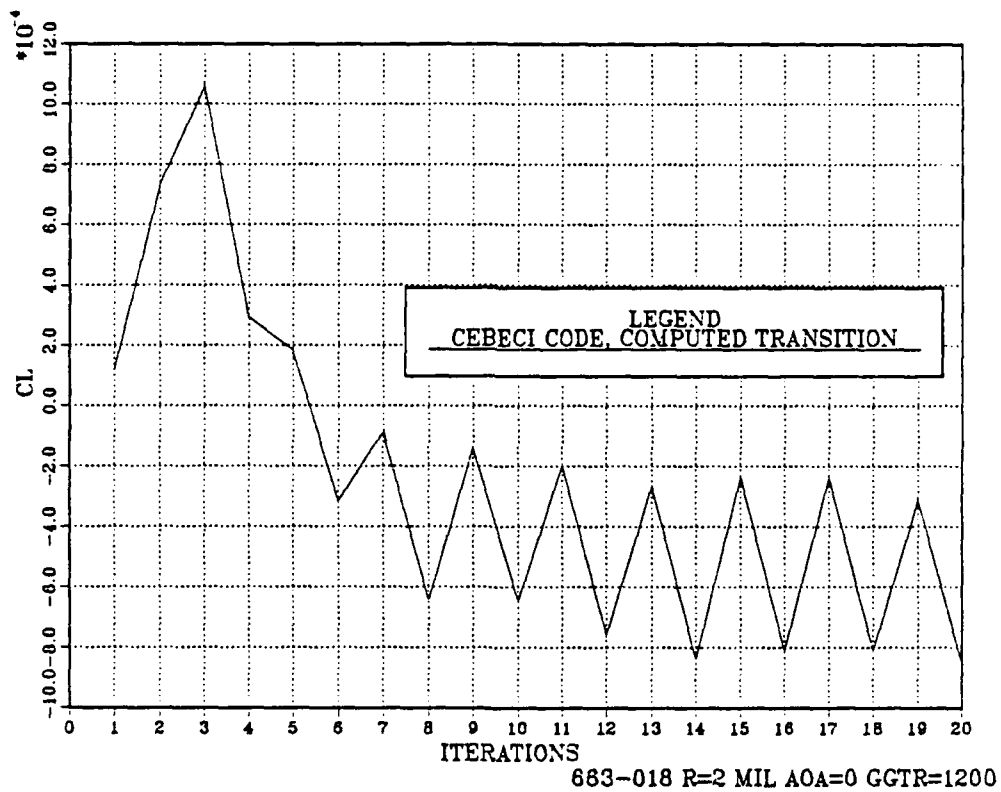
Figure 7.32   Lift Coefficient Versus Iterations, NACA
66_3-018, AOA = 0, R = 2 Million, Transition
Constant = 1200

the 7-by-10-foot wind tunnel at NASA Ames and two-dimensional flow was simulated.

The 0010 (modified) airfoil shown in Figure 7.33, unlike the 66_3-018, was not computer tested for section lift coefficients as Abbott and Doenhoff [Ref. 9] had no comparable airfoil.

Leading edge, upper surface, laminar to turbulent, transition locations were observed, though, and the results are shown in Figures 7.34 and 7.35 for Reynolds numbers of two and six million, respectively. The Cebeci Code curves represent the beginning of transition.

Full chord pressure distributions for angles of attack of zero and three degrees and Reynolds numbers of three and eight million are plotted in Figures 7.36 through 7.39.

Leading edge pressure distributions for angles of attack of four, eight and twelve degrees, and Reynolds numbers of two and six million are shown in Figures 7.40 through 7.45. Of particular interest are the "lump" disparities in Figures 7.42 through 7.45. A possible explanation for the computer program deletions of the lumps is a failure to predict leading edge bubbles.

C. NACA 4412

Computer results of the NACA 4412 airfoil section were compared to the test results of Hastings and Williams [Ref. 10], which were performed in the 13-by 9-foot low speed wind tunnel of the Royal Aircraft Establishment at Bedford. The

NACA 0010 (MODIFIED)
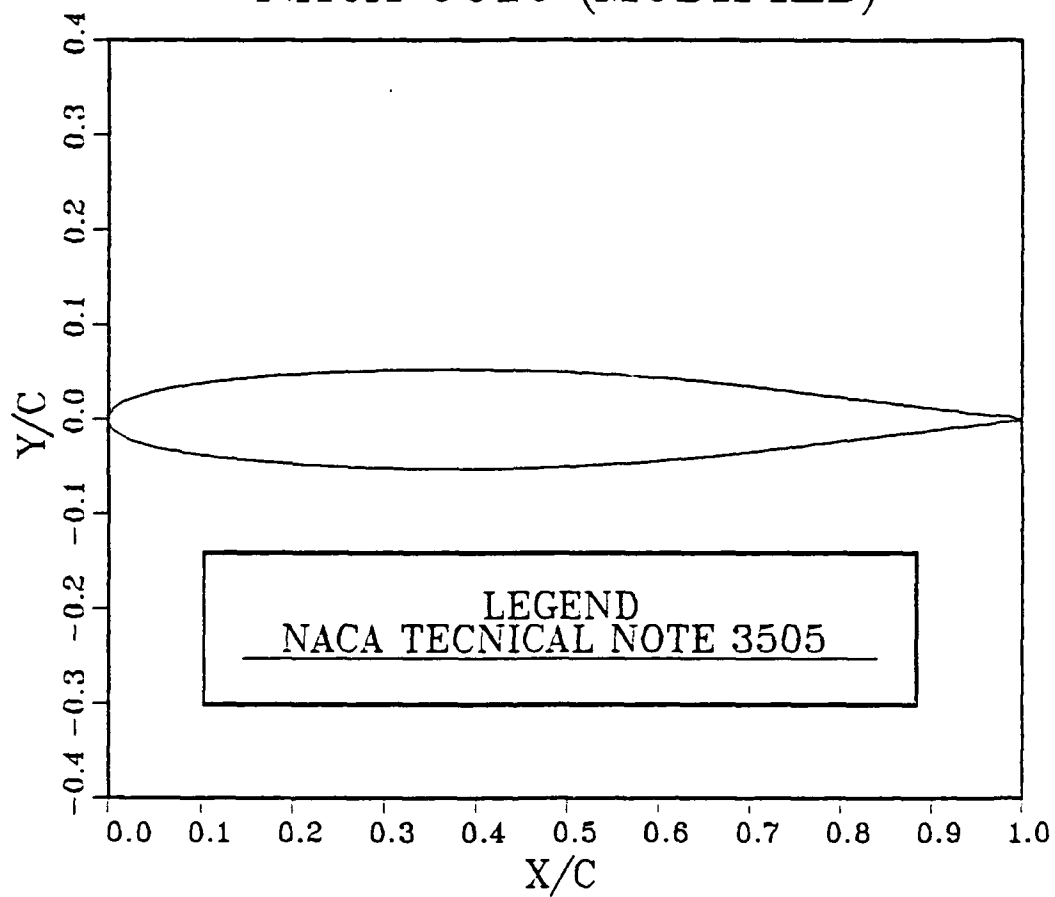
Figure 7.33   NACA 0010 (Modified)

LAMINAR TO TURBULENT TRANSITION

NACA 0010 MOD, R = 2.0 MILLION
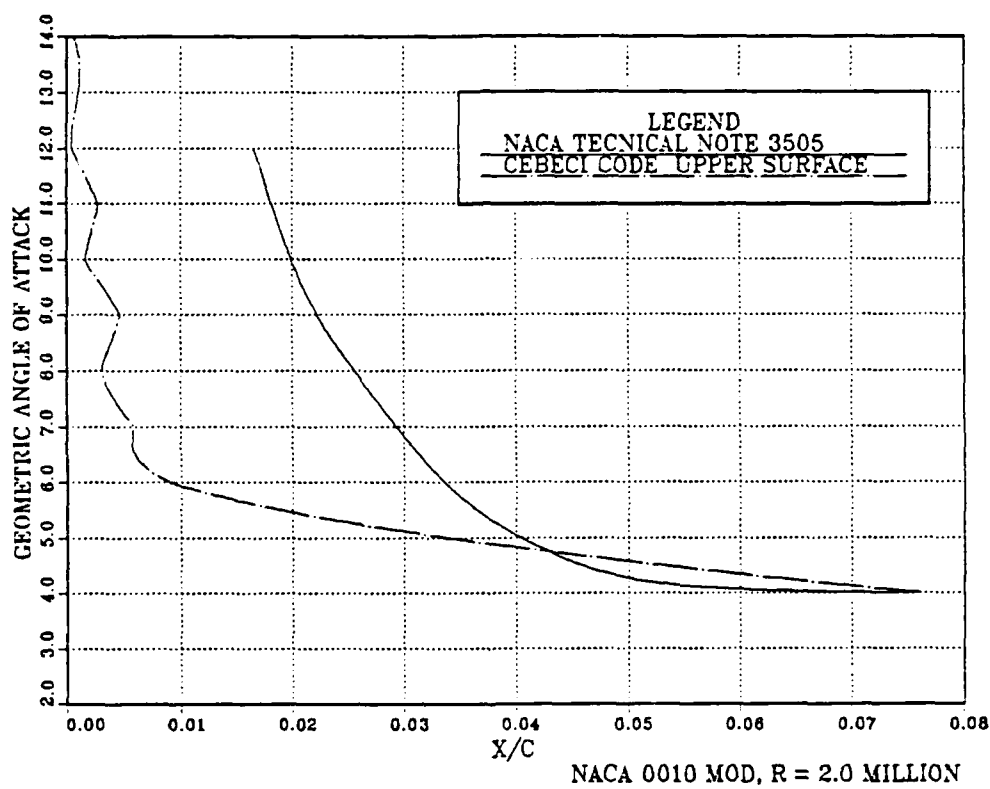
Figure 7.34   Upper Surface Laminar to Turbulent
              Transition, Leading Edge, NACA 0010
              (Modified), R = 2 Million

102
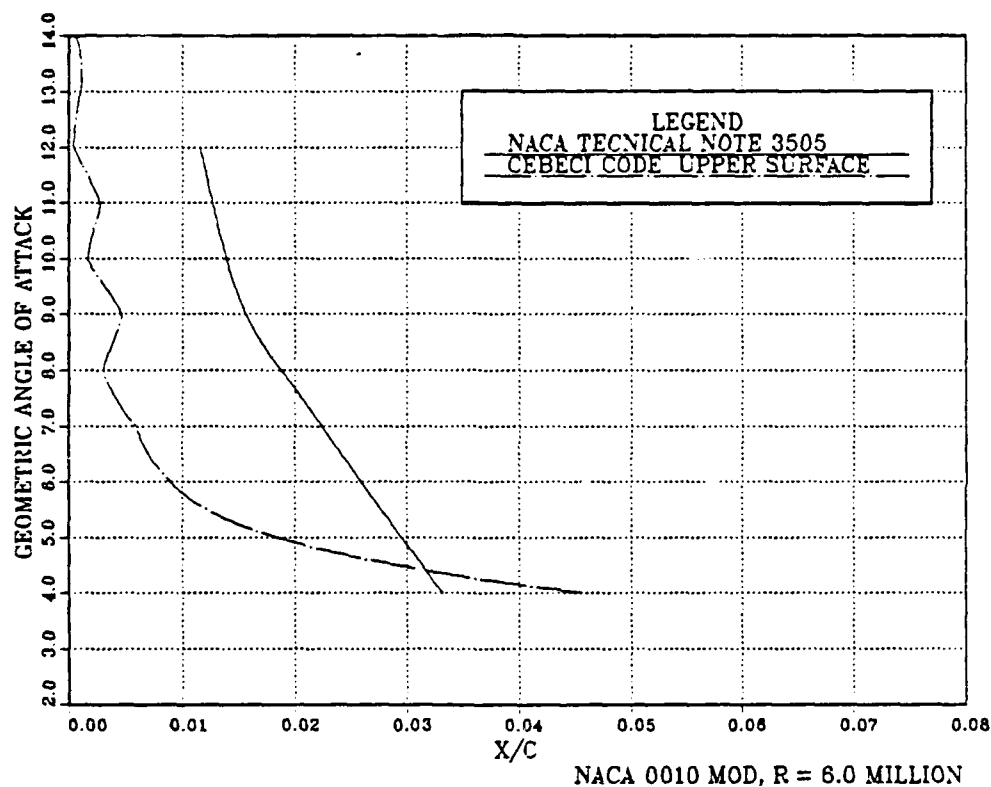
LAMINAR TO TURBULENT TRANSITION

Figure 7.35   Upper Surface Laminar to Turbulent
             Transition, Leading Edge, NACA 0010
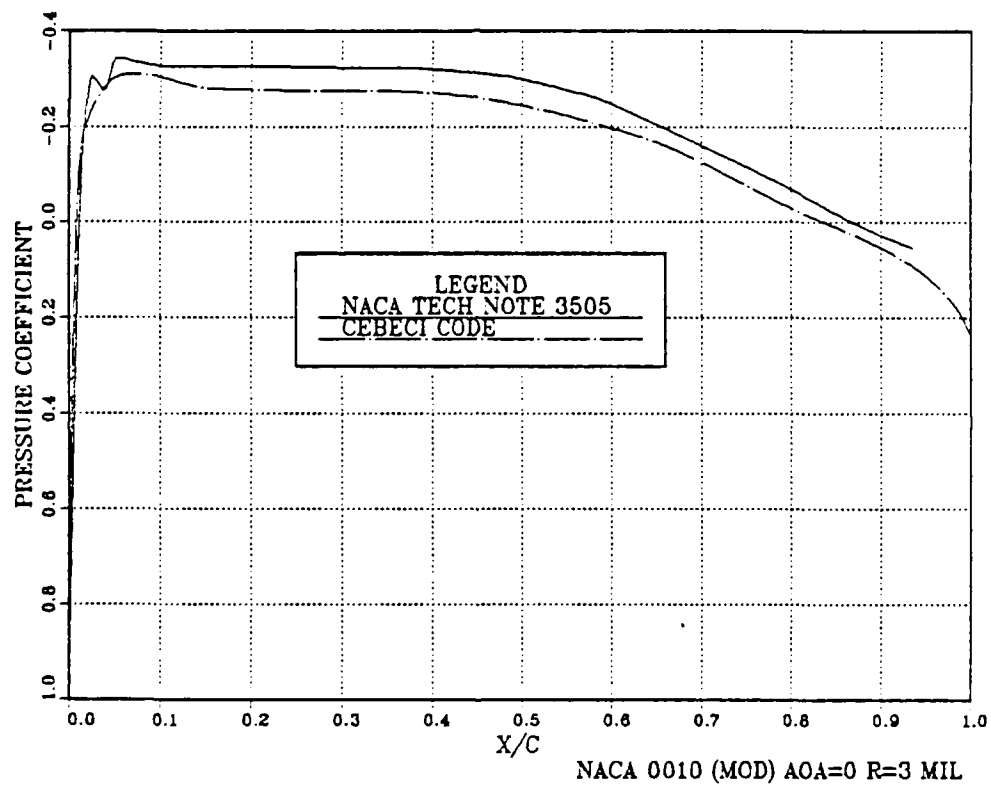   (Modified), R = 6 Million

UPPER SURFACE PRESSURE

NACA 0010 (MOD) AOA=0 R=3 MIL

Figure 7.36   Upper Surface Pressure Distribution, NACA
0010 (Modified), AOA = 0°, R = 3 Million

104

UPPER SURFACE PRESSURE

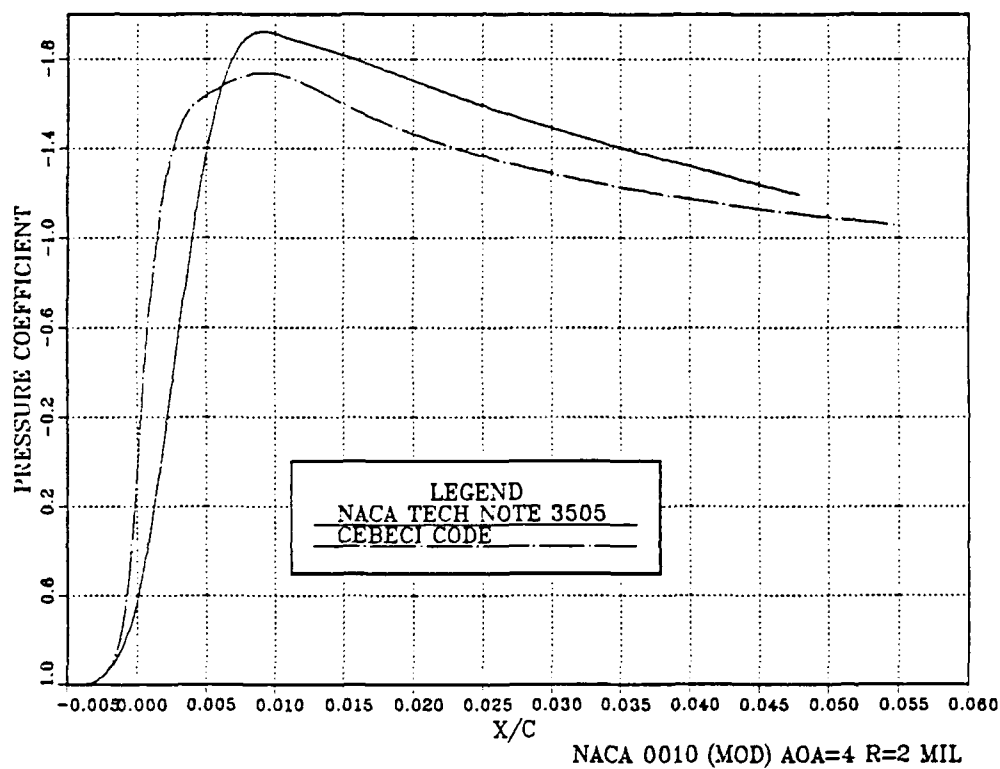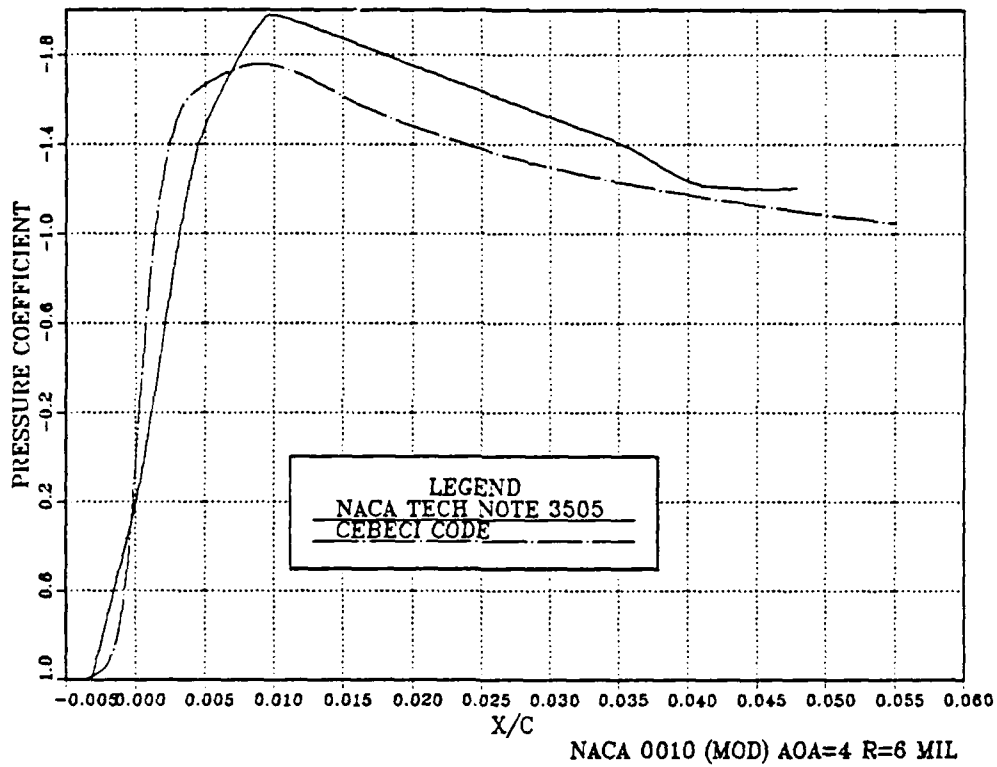NACA 0010 (MOD) AOA=0 R=8 MIL
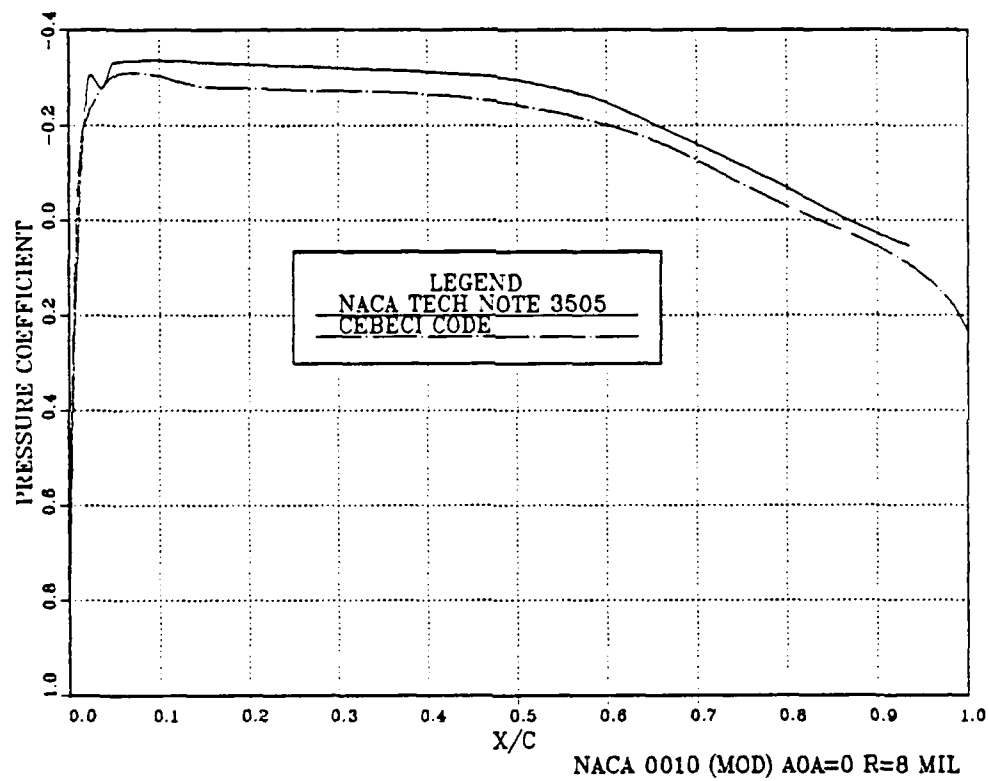
Figure 7.37   Upper Surface Pressure Distribution, NACA
0010 (Modified), AOA = 0°, R = 8 Million

105

UPPER SURFACE PRESSURE

Figure 7.38 Upper Surface Pressure Distribution, NACA
0010 (Modified), AOA = 3°, R = 3 Million

UPPER SURFACE PRESSURE

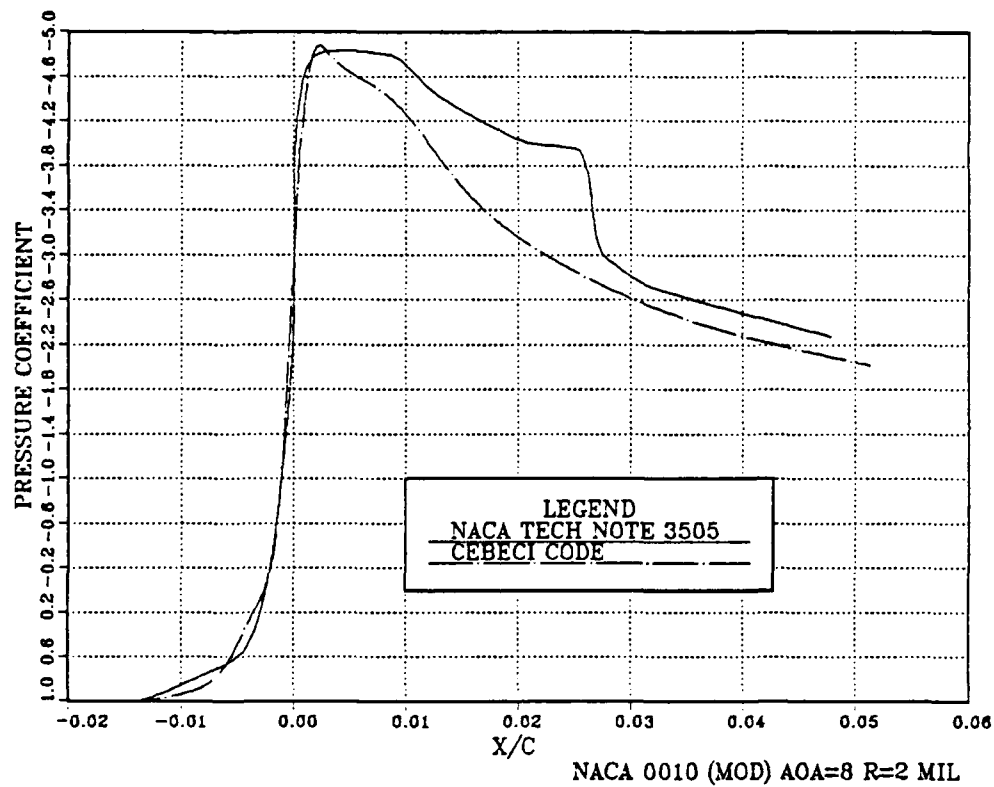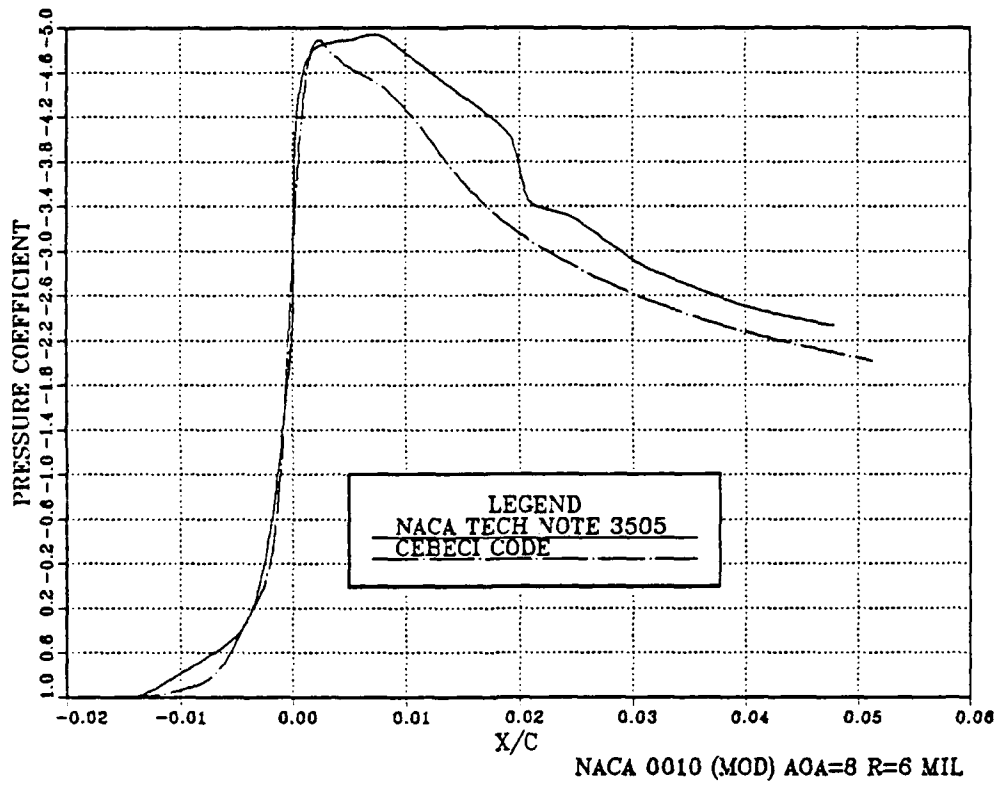NACA 0010 (MOD) AOA=3 R=8 MIL
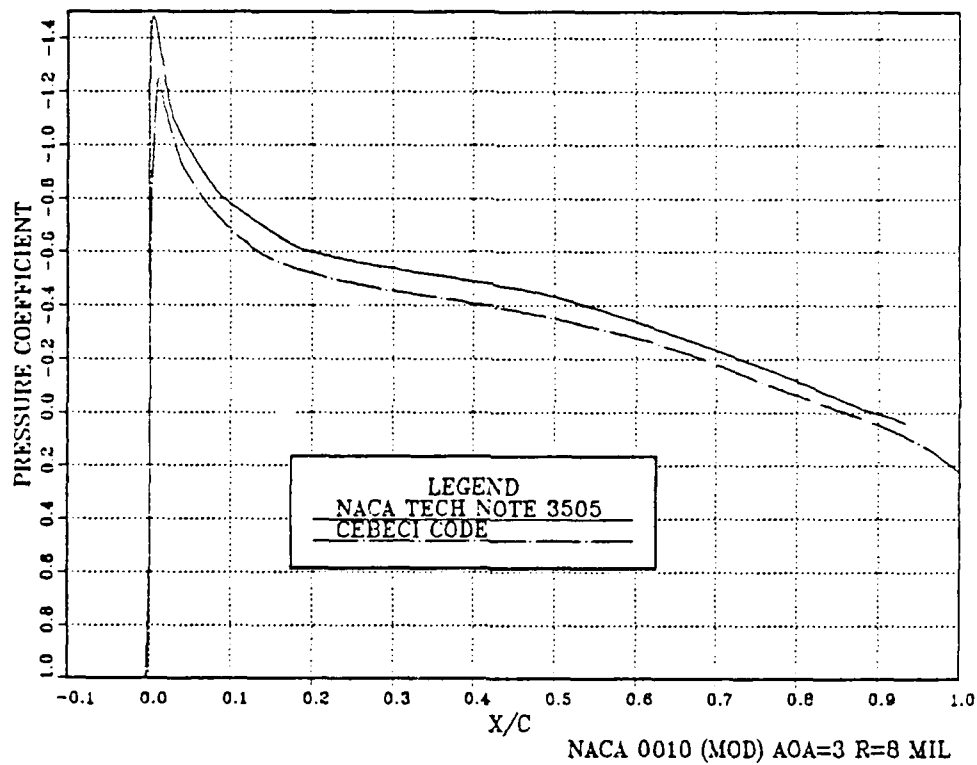
Figure 7.39   Upper Surface Pressure Distribution, NACA
0010 (Modified), AOA = 3°, R = 8 Million
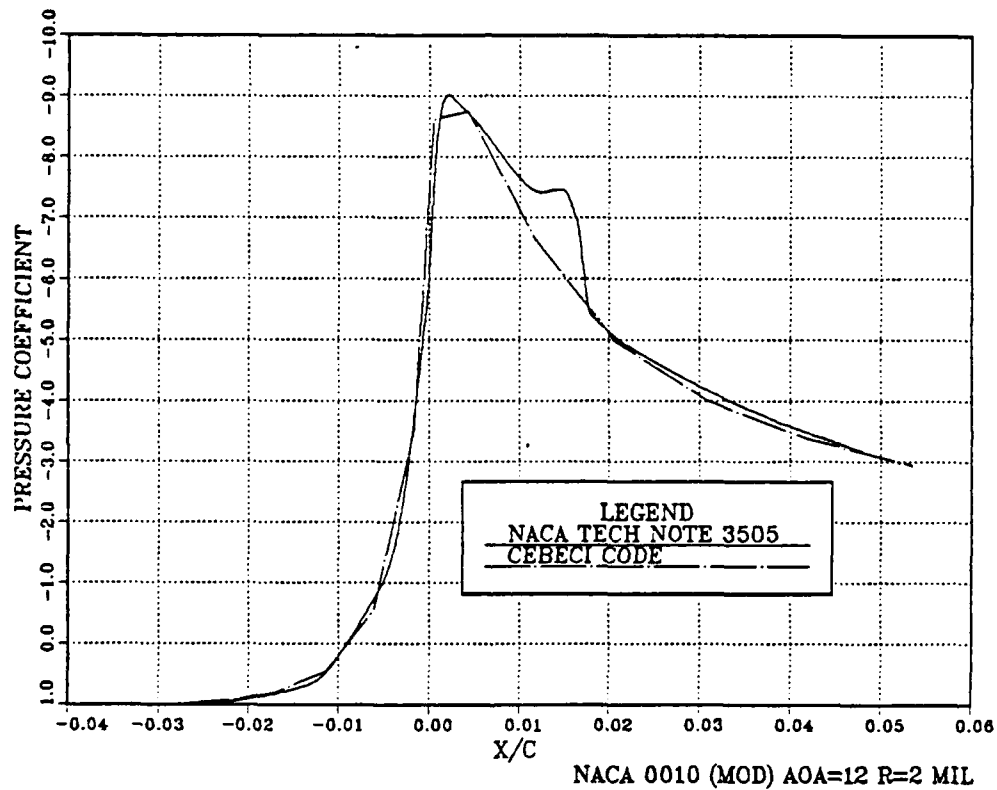
UPPER SURFACE PRESSURE

NACA 0010 (MOD) AOA=4 R=2 MIL

Figure 7.40   Leading Edge Upper Surface Pressure
Distribution, NACA 0010 (Modified), AOA = 4°,
R = 2 Million

UPPER SURFACE PRESSURE

NACA 0010 (MOD) AOA=4 R=6 MIL

Figure 7.41 Leading Edge Upper Surface Pressure
Distribution, NACA 0010 (Modified), AOA = 4°,
R = 6 Million

UPPER SURFACE PRESSURE

NACA 0010 (MOD) AOA=8 R=2 MIL

Figure 7.42 Leading Edge Upper Surface Pressure
Distribution, NACA 0010 (Modified), AOA = 8°,
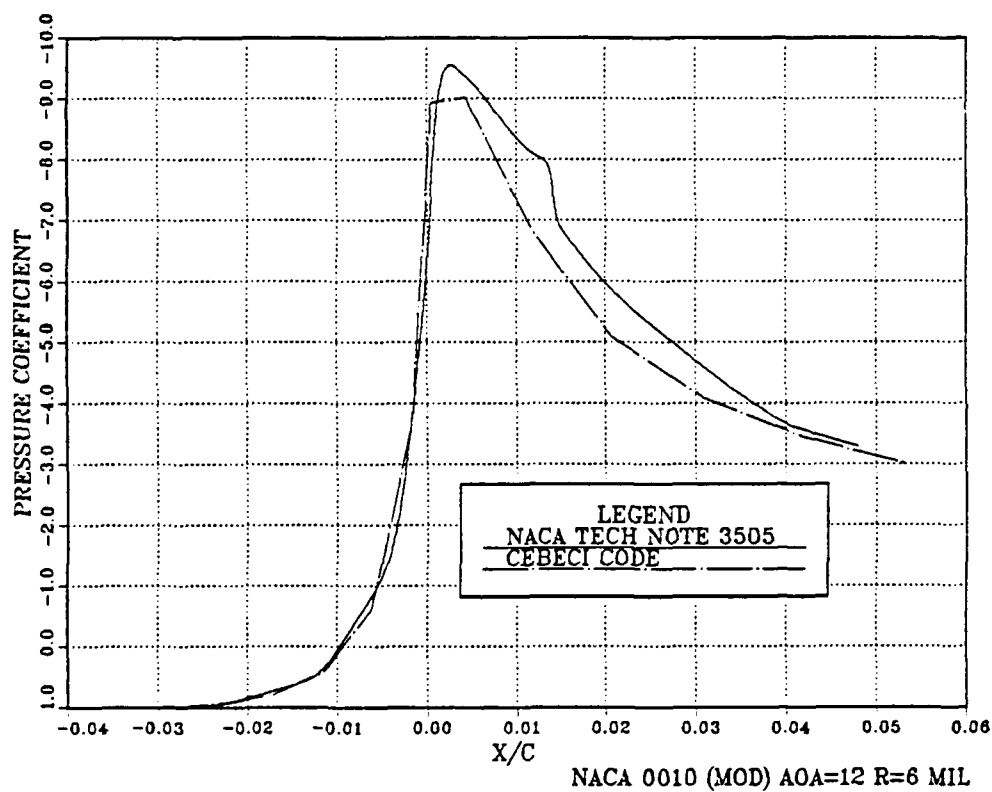R = 2 Million

110

UPPER SURFACE PRESSURE

NACA 0010 (MOD) AOA=8 R=6 MIL

Figure 7.43 Leading Edge Upper Surface Pressure Distribution, NACA 0010 (Modified), AOA = 8°, R = 6 Million

UPPER SURFACE PRESSURE

NACA 0010 (MOD) AOA=12 R=2 MIL

Figure 7.44   Leading Edge Upper Surface Pressure
              Distribution, NACA 0010 (Modified),
              AOA = 12°, R = 2 Million

112

UPPER SURFACE PRESSURE

NACA 0010 (MOD) AOA=12 R=6 MIL

Figure 7.45   Leading Edge Upper Surface Pressure
Distribution, NACA 0010 (Modified),
AOA = 12°, R = 6 Million

113

one meter chord model spanned the full width, 13 feet, to simulate two-dimensional flow.

Mounted at its quarter-chord point, the model was extensively instrumented with static pressure orifices. Boundary layer and wake measurements were made at mid-span where the 88 pressure orifices were located.

The main emphasis in the experiment was on defining the upper surface boundary layer through separation and into the wake. Laser anemometry was used to measure the average velocities and Reynolds stresses were measured by hot-wire anemometry.

The 4412 shown in Figure 7.46 was initially computer tested with the Cebeci code for momentum thickness. In Figure 7.47 the upper and lower surface laminar to turbulent transitions were computer derived, x/c_{tr} upper and lower surfaces = 0.00625. In Figure 7.48 the upper and lower surface transitions were input as x/c_{tr} upper surface = 0.01, and x/c_{tr} lower surface = 0.11. These values were as close as could be input to 0.014 and 0.110 respectively, for the downstream ends of the transition trips used in the experiment. The differences in transition locations seemed to make no difference in computer results. The momentum thicknesses still did not agree very well with Hastings and Williams' experimental results.

Figure 7.49 compares lift coefficients from the Cebeci code, Hastings and Williams, and Abbott and Doenhoff [Ref.
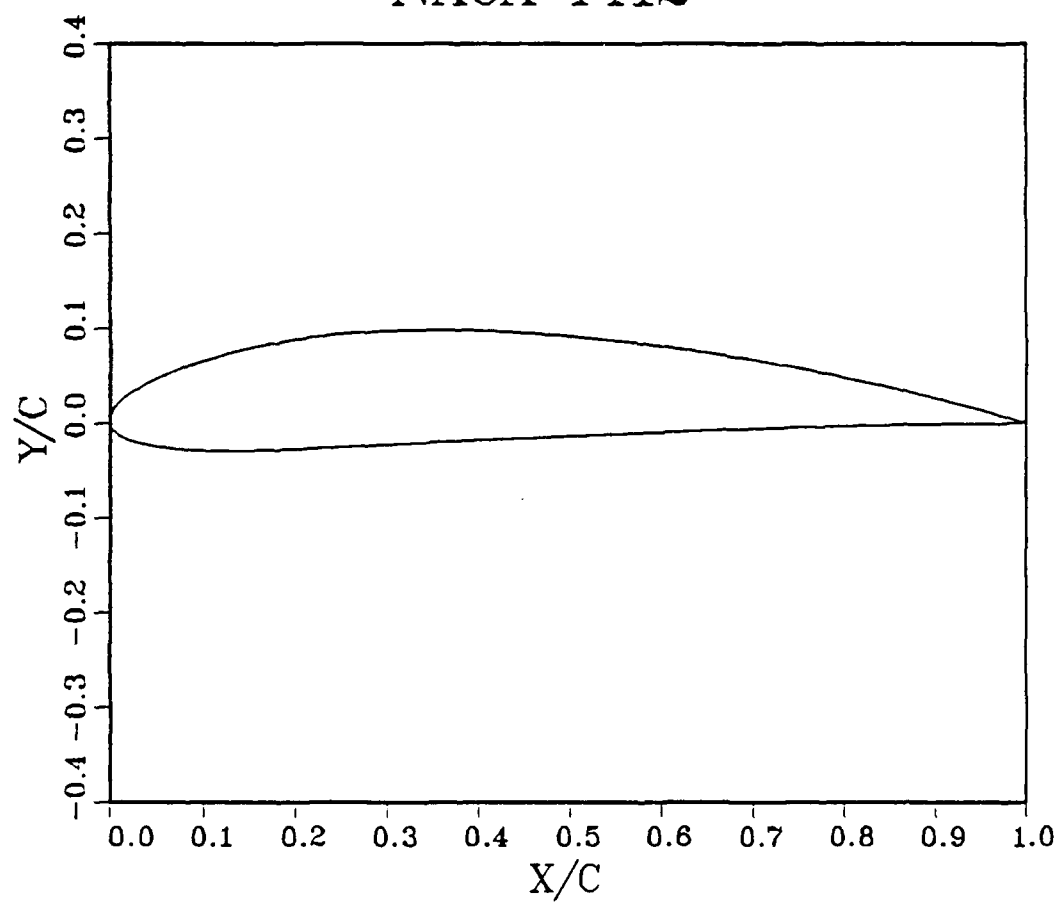
114

NACA 4412

Figure 7.46   NACA 4412
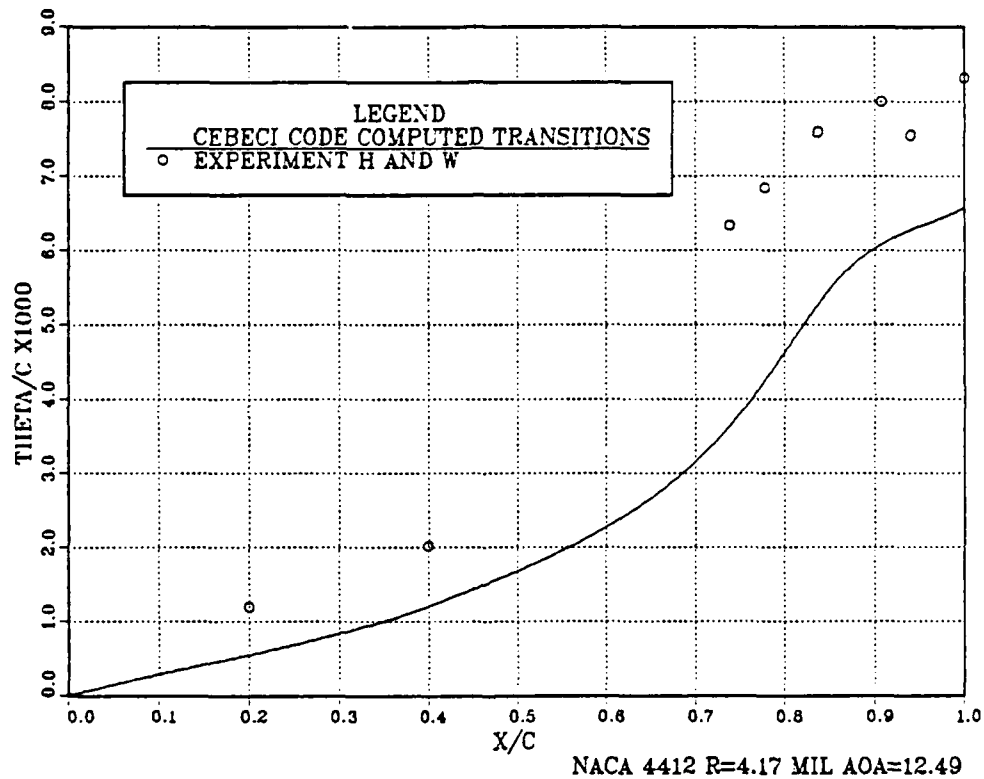
UPPER SURFACE MOMENTUM THICKNESS

Figure 7.47   Upper Surface Momentum Thickness, NACA 4412,
AOA = 12.49°, R = 4.17 Million, Computer
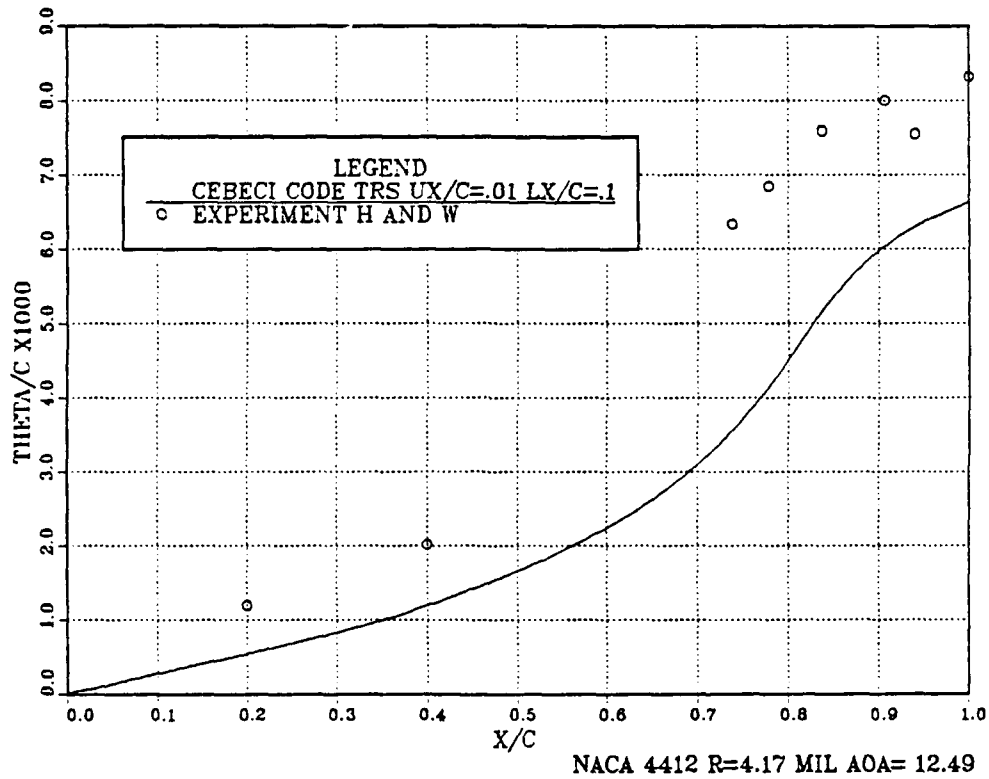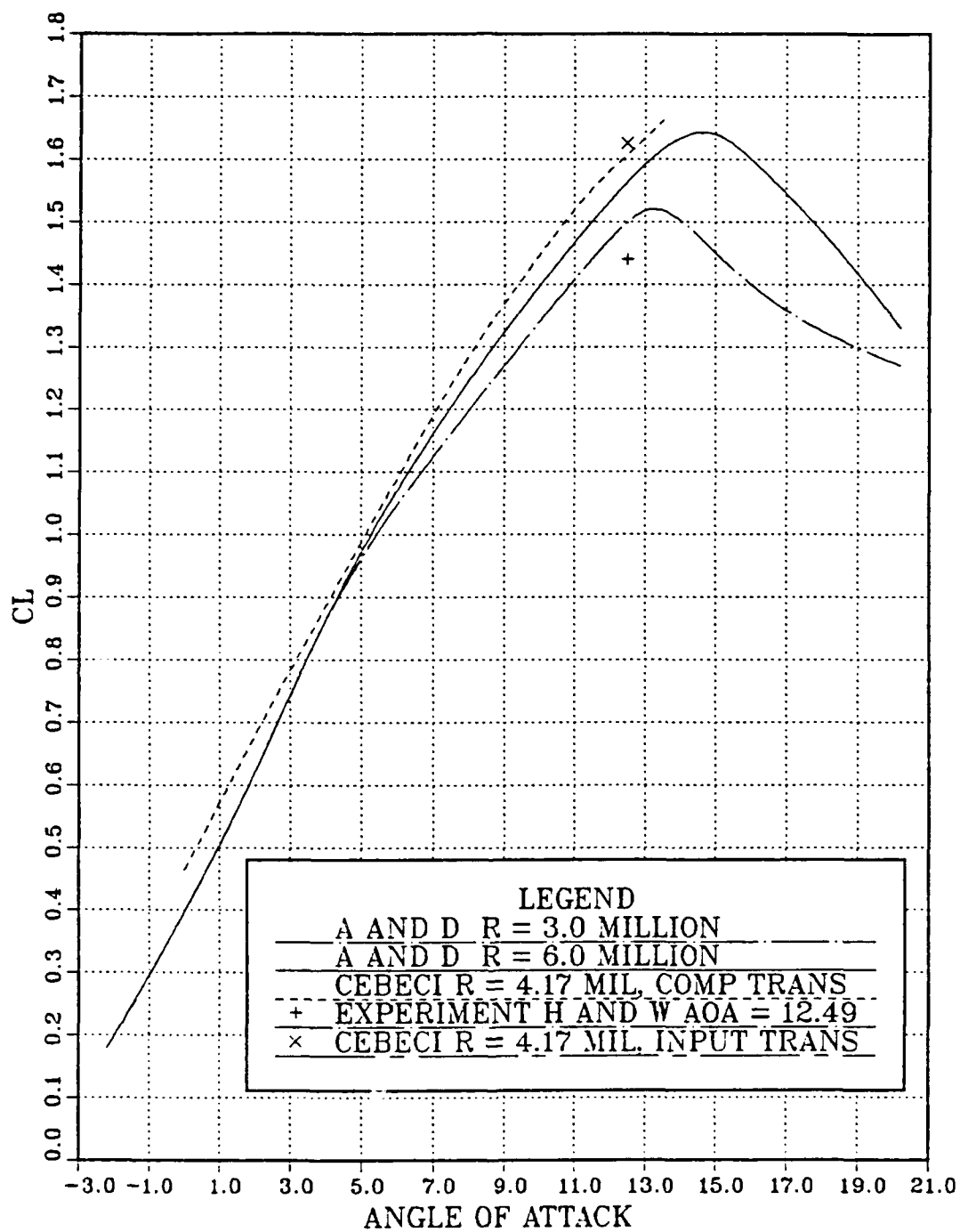Derived Transitions

UPPER SURFACE MOMENTUM THICKNESS

NACA 4412 R=4.17 MIL AOA= 12.49

Figure 7.48   Upper Surface Momentum Thickness, NACA 4412,
AOA = 12.49°, R = 4.17 Million, Computer
Derived Input Transitions

117

LIFT COEFFICIENT

NACA 4412

Figure 7.49   Lift Coefficients, NACA   4412

118

10]. The dashed line for the Cebeci code, Reynolds number equal to 4.17 million and computer derived transitions, should lie between the curves for Reynolds number equal to three and six million from Abbott and Doenhoff. However, it lies above the six million curve which further indicates an insufficient boundary layer development. With the input transition the code prediction for Reynolds number equal to 4.17 million and angle of attack equal to 12.49 degrees, was even higher. Of interesting note though, is that the Hastings and Williams prediction, Reynolds number equals 4.17 million and angle of attack equals 12.49 degrees, lies below the Abbott and Doenhoff values, possibly indicating an error on their part.

Figures 7.50 through 7.56 show the velocity profiles from x/c = .66 to the trailing edge. In all cases the Reynolds number was 4.17 million, the angle of attack was 12.49 degrees, and the upper and lower transitions were .01 and .11, respectively. U/U_e indicates the fraction of the velocity at the boundary layer edge, and η/Delta is the fraction of boundary layer thickness, where Delta, δ, is defined as the layer thickness where the velocity is 99% of the edge velocity.

As these figures indicate, as well as Figure 7.57, a Cebeci code velocity profile summation, the code does predict separation, but not the extent indicated by Hastings and Williams. If the lift coefficient curves, Figure 7.58, can
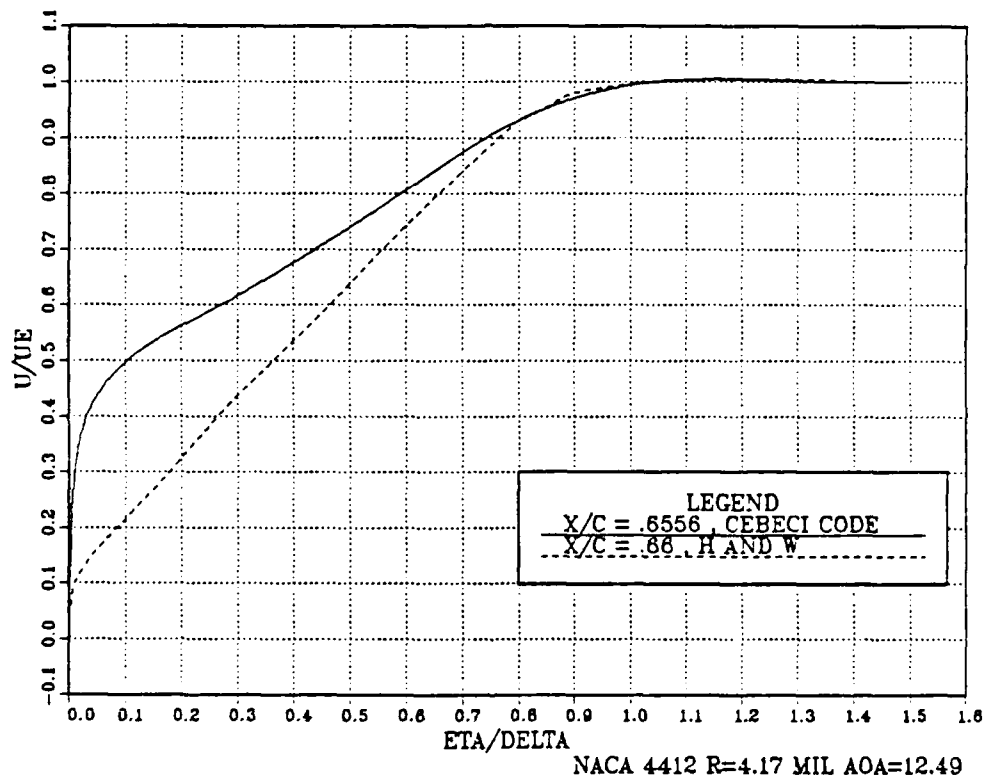
119

UPPER SURFACE VELOCITY PROFILE

NACA 4412 R=4.17 MIL AOA=12.49

Figure 7.50   Upper Surface Velocity Profile, NACA 4412,
              X/C = .66, AOA = 12.49°, R = 4.17 Million
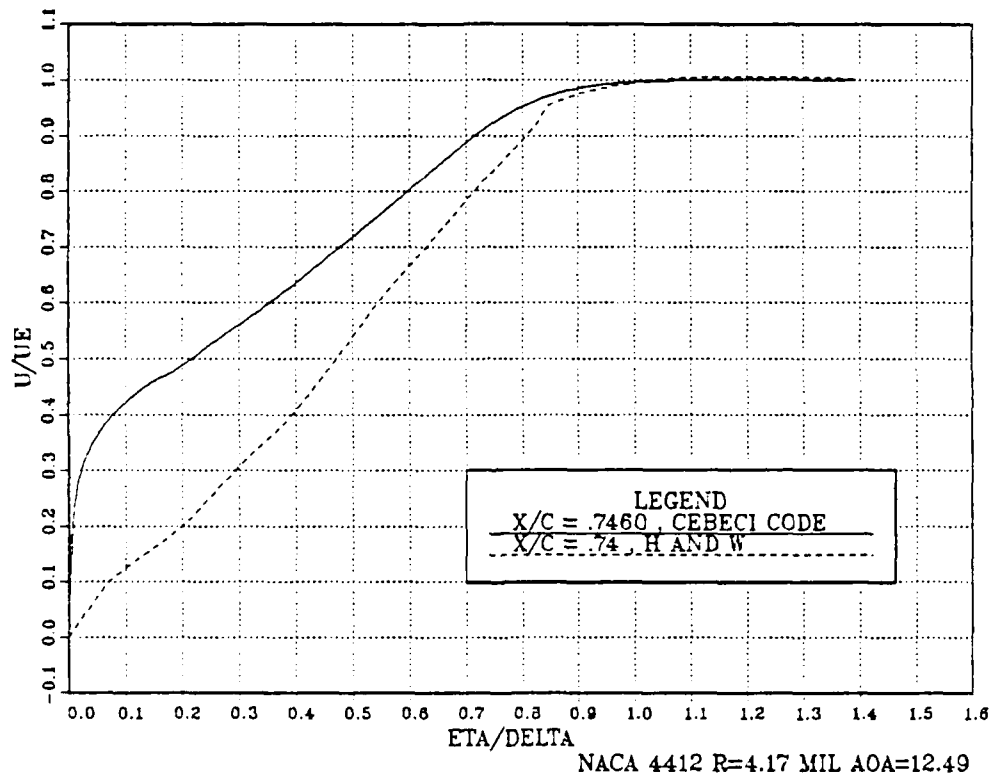
120

UPPER SURFACE VELOCITY PROFILE

NACA 4412 R=4.17 MIL AOA=12.49

Figure 7.51 Upper Surface Velocity Profile, NACA 4412,
X/C = .74, AOA = 12.49°, R = 4.17 Million

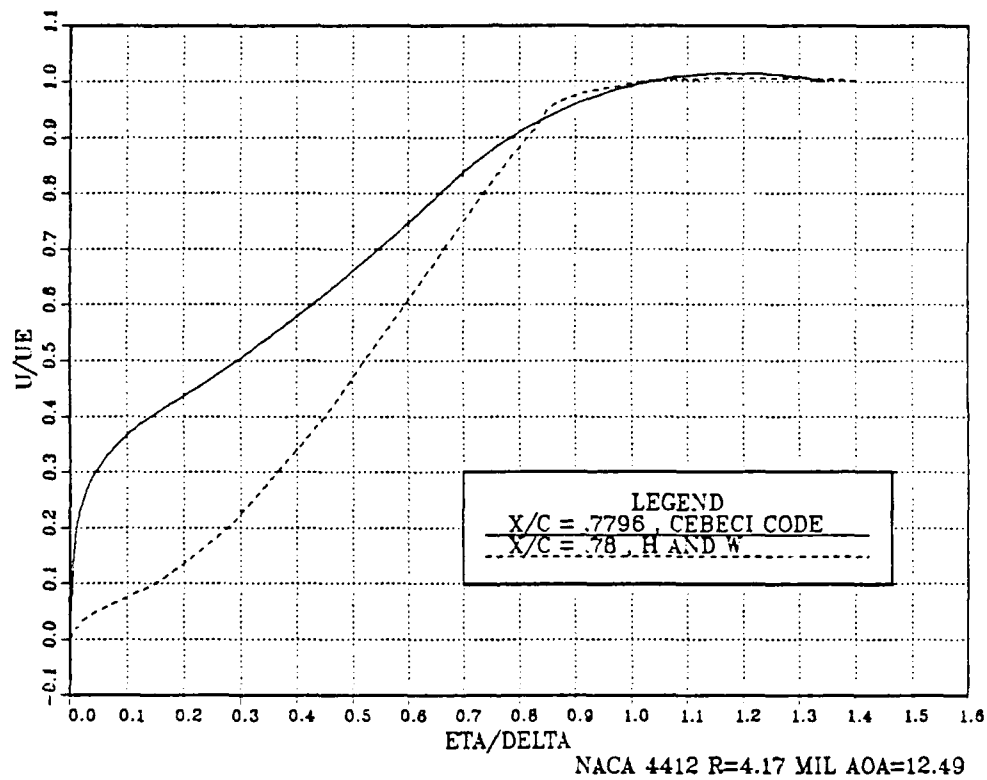121

UPPER SURFACE VELOCITY PROFILE

NACA 4412 R=4.17 MIL AOA=12.49

Figure 7.52 Upper Surface Velocity Profile, NACA 4412,
X/C = .78, AOA = 12.49°, R = 4.17 Million

UPPER SURFACE VELOCITY PROFILE

NACA 4412 R=4.17 MIL AOA=12.49
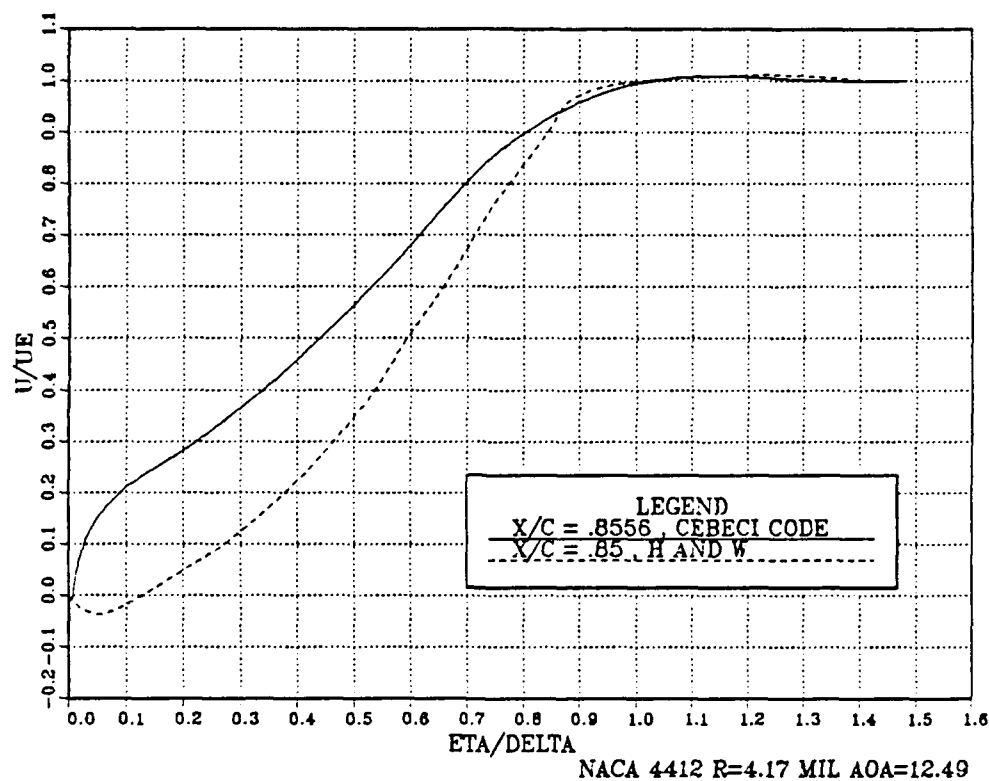
Figure 7.53   Upper Surface Velocity Profile, NACA 4412,
X/C = .85, AOA = 12.49°, R = 4.17 Million

UPPER SURFACE VELOCITY PROFILE
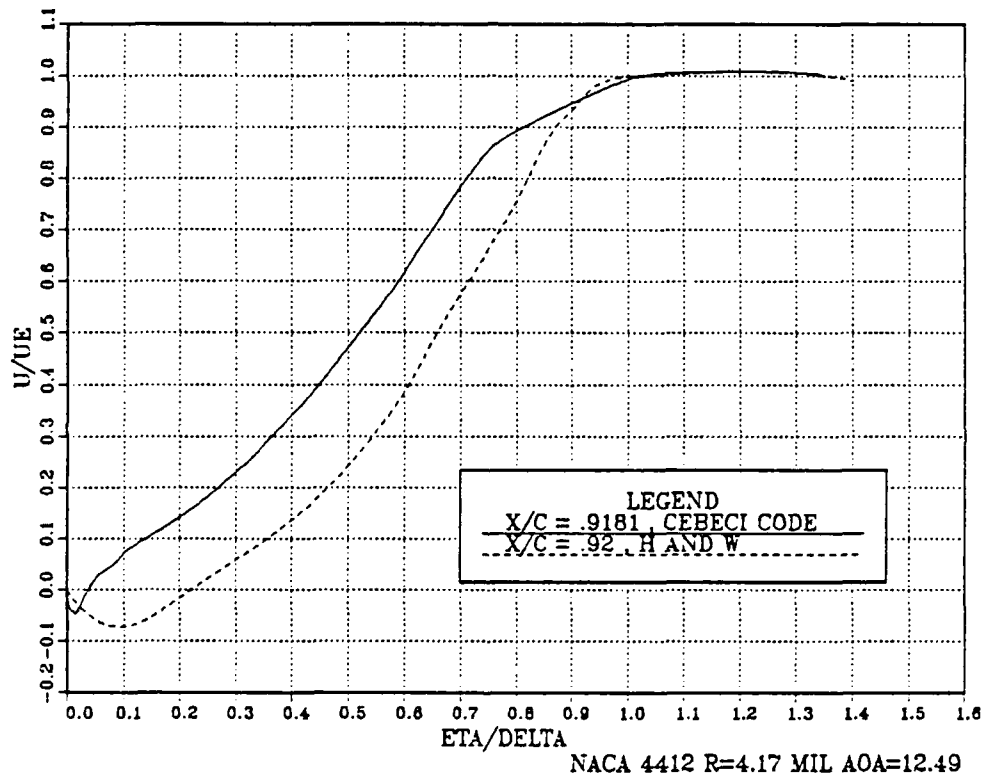

NACA 4412 R=4.17 MIL AOA=12.49

Figure 7.54   Upper Surface Velocity Profile, NACA 4412,
X/C = .92, AOA = 12.49°, R = 4.17 Million

124

UPPER SURFACE VELOCITY PROFILE

Figure 7.55   Upper Surface Velocity Profile, NACA 4412,
              X/C = .95, AOA = 12.49°, R = 4.17 Million
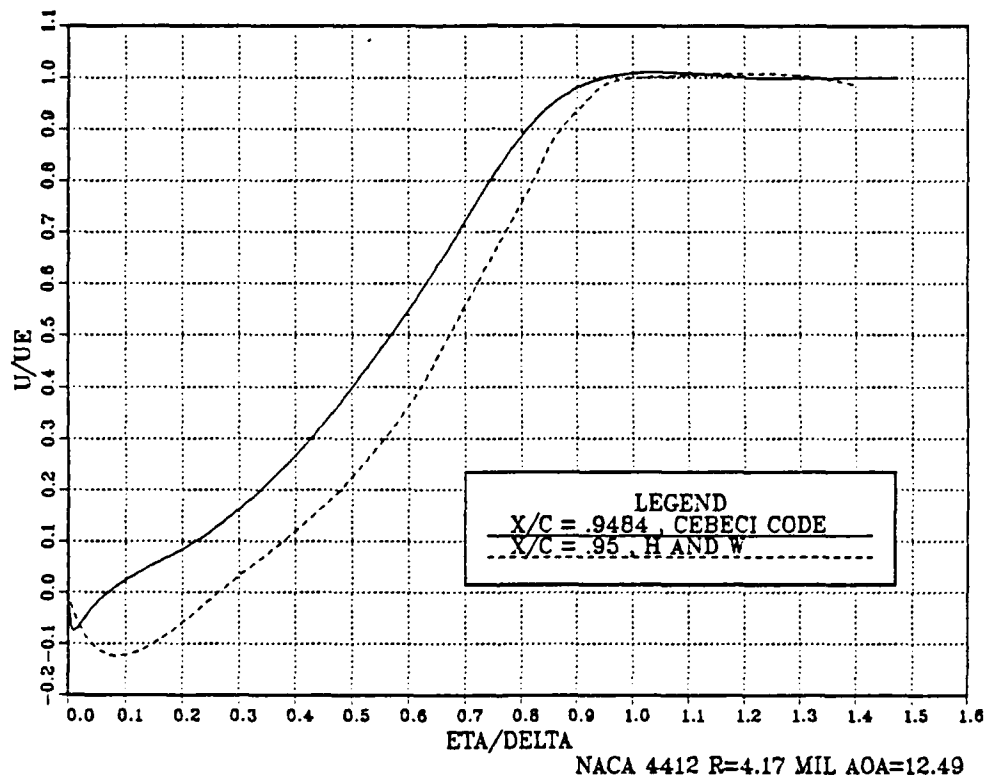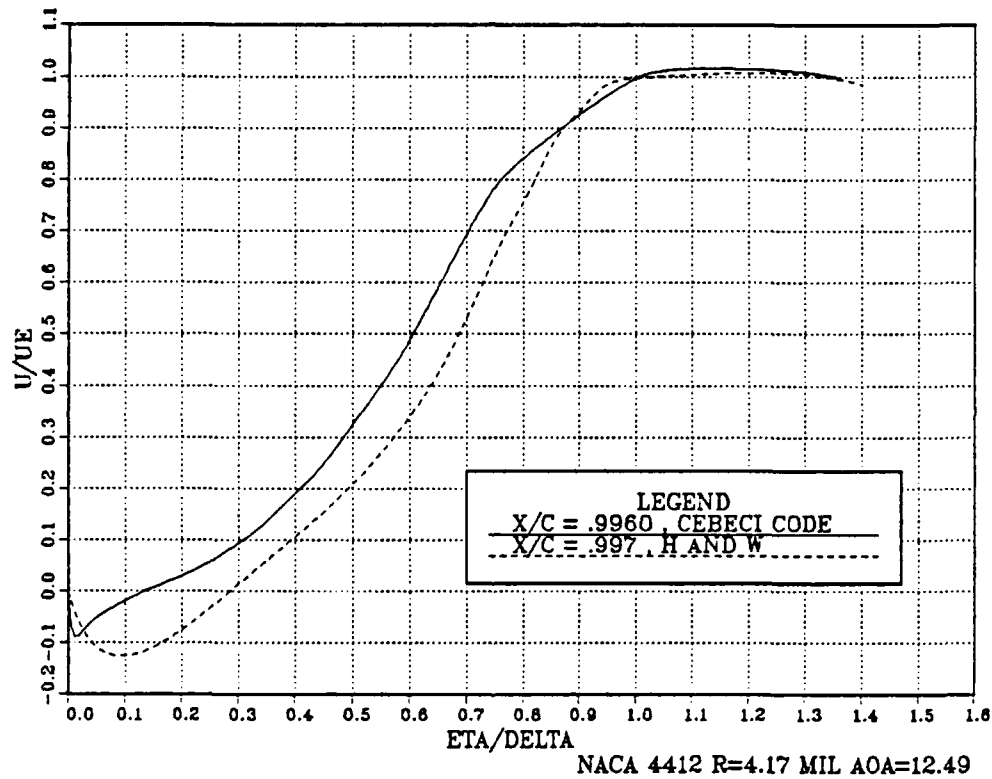
125

UPPER SURFACE VELOCITY PROFILE

NACA 4412 R=4.17 MIL AOA=12.49

Figure 7.56   Upper Surface Velocity Profile, NACA 4412,
X/C = .997, AOA = 12.49°, R = 4.17 Million
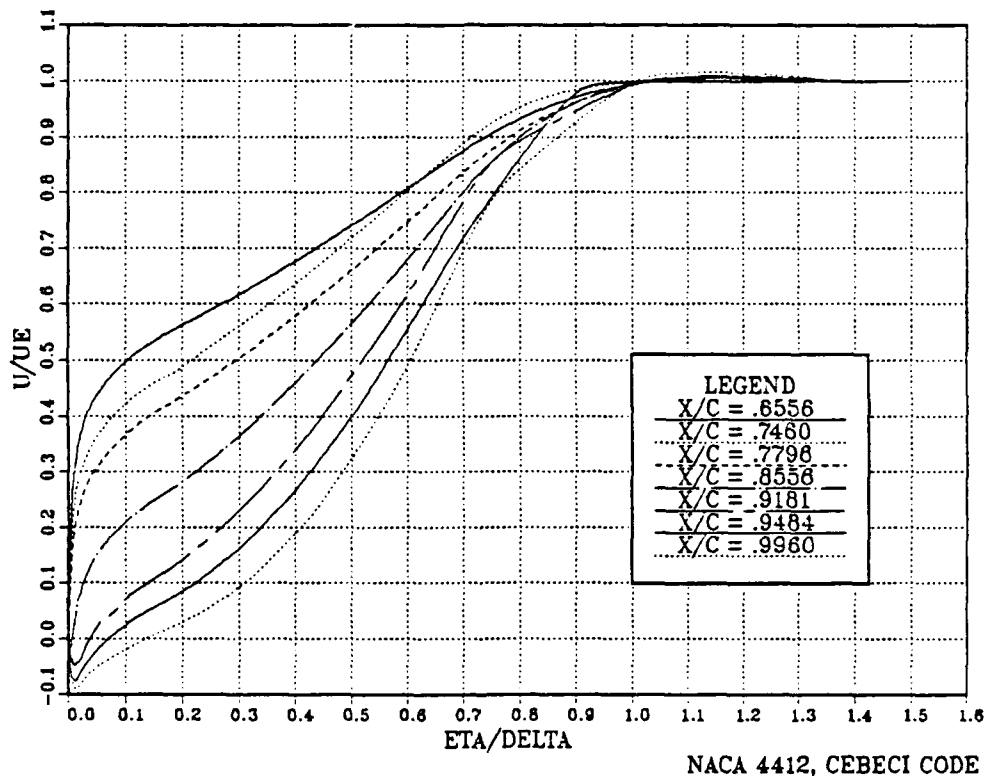
126

UPPER SURFACE VELOCITY PROFILES

NACA 4412, CEBECI CODE

Figure 7.57   Upper Surface Velocity Profiles, NACA 4412,
AOA = 12.49°, R = 4.17 Million

127

LIFT COEFFICIENT

LEGEND
INTERACTIVE THEORY C,C,C,H, & L
INT THEORY, MODIFIED TRANSITION
CEBECI CODE PROGRAM TRANS, 20 IT

ANGLE OF ATTACK
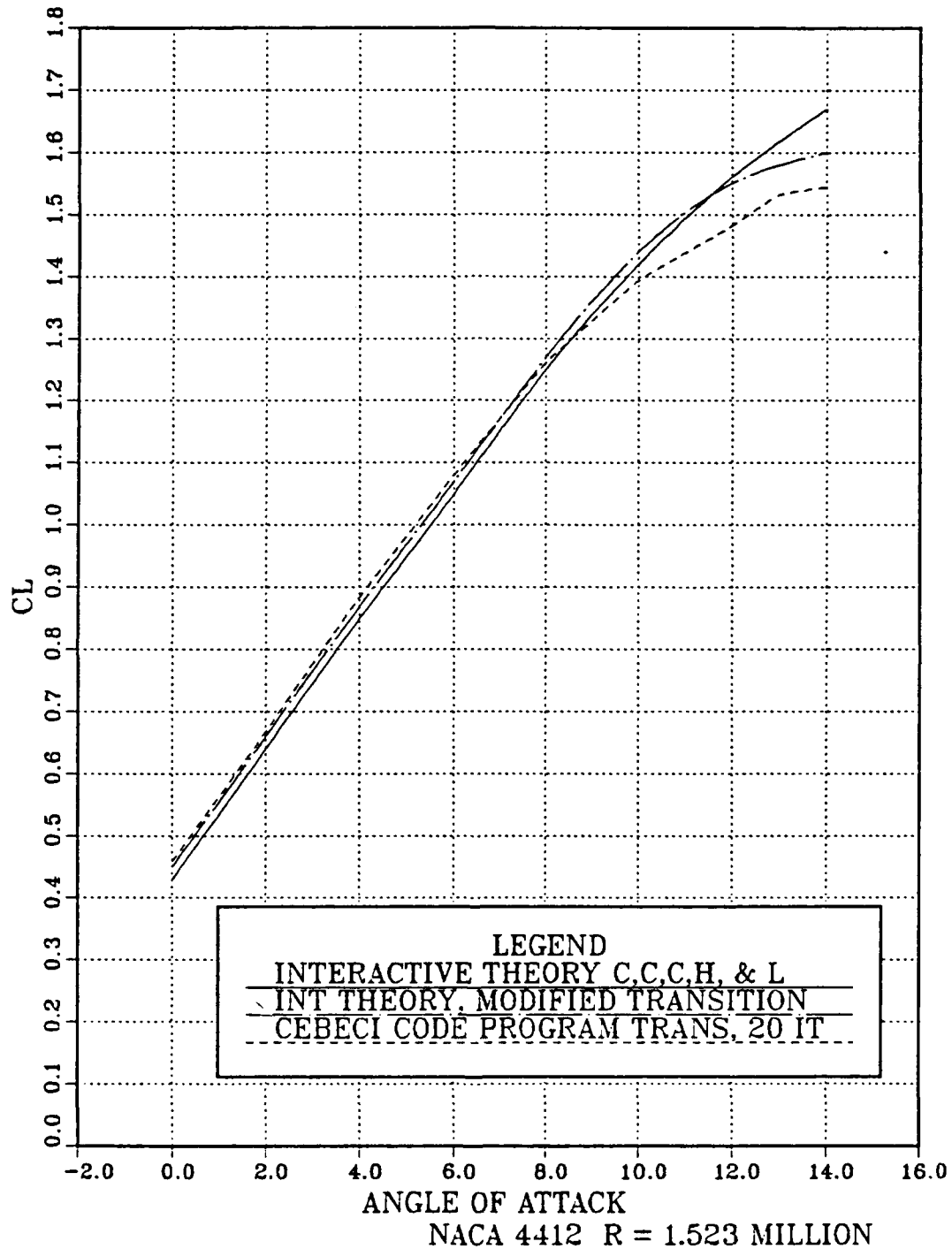NACA 4412 R = 1.523 MILLION

Figure 7.58   Lift Coefficient, NACA 4412, 20 Iterations,
R = 1.523 Million

be a reference, then it appears that the Cebeci code predicts an underdeveloped flow, too little separation, and Hastings and Williams show an overdeveloped flow, too much separation, for the given conditions.

To insure that the Cebeci Code was run correctly, certain results by Cebeci, Clark, Chang, Halsey and Lee [Ref. 1] were attempted to be duplicated. Figure 7.58 compares two curves from Figure 14, [Ref. 1], curves labeled interactive theory and interactive theory with a modified transition, with a curve obtained using the Cebeci Code with 20 iterations and computer derived transitions. Interestingly, the first and third curves of Figure 7.58, interactive theory and Cebeci Code, respectively, should be the same, but the two clearly are not above nine degrees angle of attack. Even more interestingly, the Cebeci Code lift curve in Figure 7.59 after only 10 iterations does match the interactive theory curve.

Figure 7.60 clearly shows the importance of using enough iterations to obtain a reasonably accurate solution.

Finally, Figure 7.61 shows a very good match between the pressure coefficients for set conditions of Figure 16, Cebeci et al [Ref. 1], and the Cebeci Code, 20 iterations.

D. FX 63-137

Computer results of the Wortmann FX 63-137 airfoil were compared to the test results of Brendel and Mueller [Ref. 11], which were conducted in the University of Notre Dame
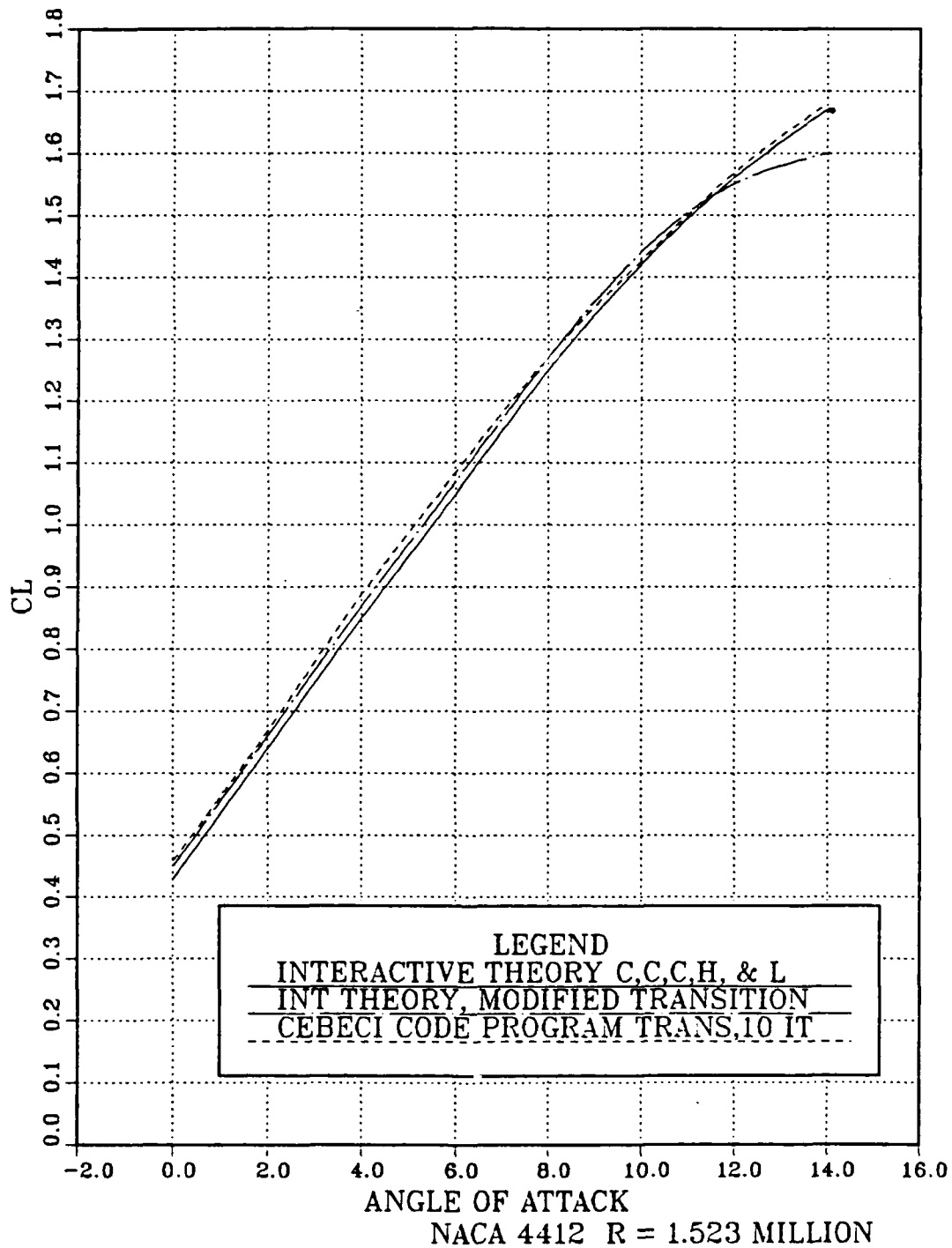
129

LIFT COEFFICIENT

ANGLE OF ATTACK

NACA 4412 R = 1.523 MILLION

Figure 7.59 Lift Coefficient, NACA 4412, 20 Iterations,
R = 1.523 Million

130

LIFT COEFFICIENT ITERATIONS
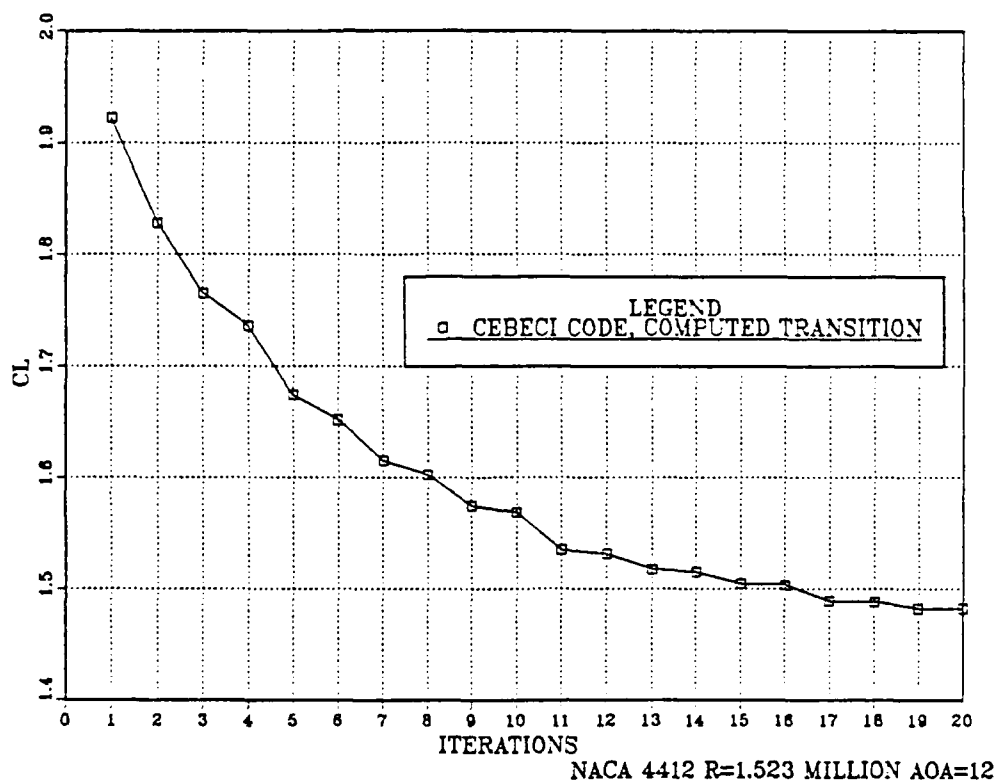
Figure 7.60   Lift Coefficient Versus Iterations,
NACA 4412, AOA = 12°, R = 1.523 Million

131

VARIATION OF CP WITH X/C
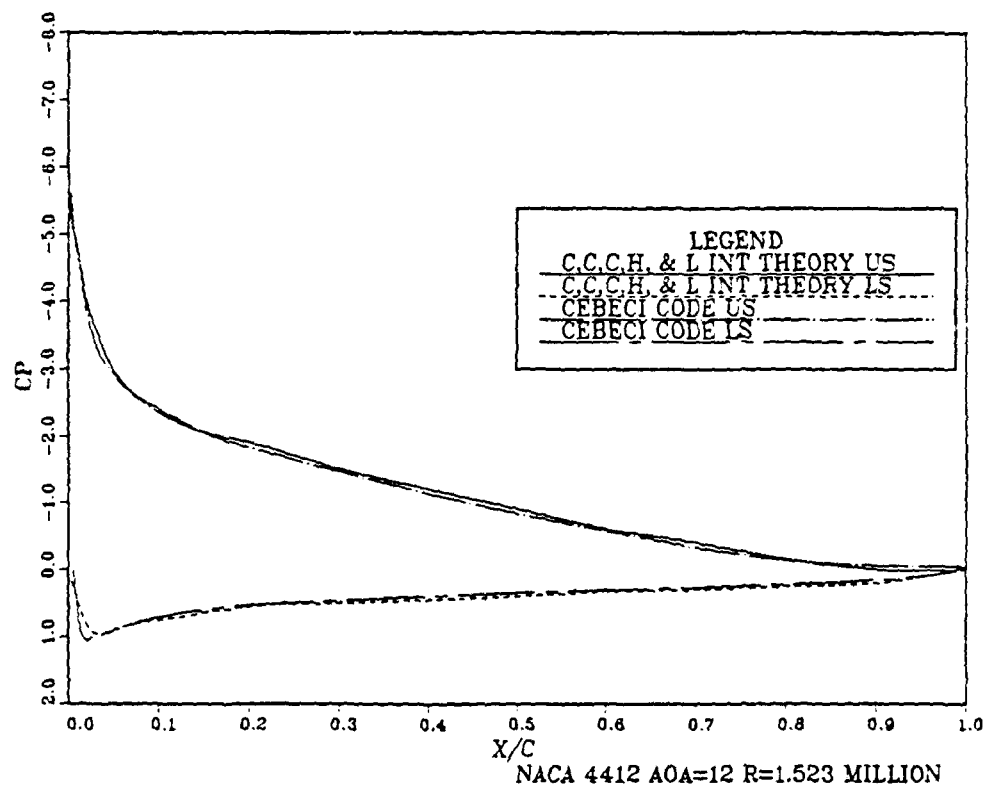

NACA 4412 AOA=12 R=1.523 MILLION

Figure 7.61   Variation of Pressure Coefficient,
NACA 4412, AOA = 12°, R = 1.523 Million

.61m x .61m wind tunnel. Two cast epoxy resin airfoil models with chords of .305m and spans of .4m were mounted in the center of the test section. Pressure was recorded on one model with 96 pressure taps connected through two scanivalves to an electronic manometer. Boundary layer velocity measurements were obtained on the other model using a constant temperature anemometer with a five μm diameter, single-sensor, hot-wire, boundary layer probe.

Using the Cebeci Code the FX 63-137 airfoil shown in Figure 7.62 was initially tested for section lift coefficients with a transition constant of 1200. Reynolds numbers of .28, .5 and .7 million were used, and the results, shown in Figures 7.63 and 7.64, were compared to those of Althaus and Wortmann [Ref. 12]. Interestingly, the Cebeci Code predicted low values for Reynolds numbers of .28 and .5 million, but for .7 million the lift coefficients were nearly identical to Althaus and Wortmann up to an angle of attack of 10 degrees.

As the purpose of Brendel and Mueller was to make boundary layer measurements at low Reynolds numbers, a computer comparison was unsuccessfully attempted for steady flow at a Reynolds number of 100,000 and an angle of attack of 7 degrees. With 20 iterations the Cebeci Code failed.

To understand why the code calculations ceased for this case, other computer runs were attempted for the same Reynolds number and angle of attack, but with fewer
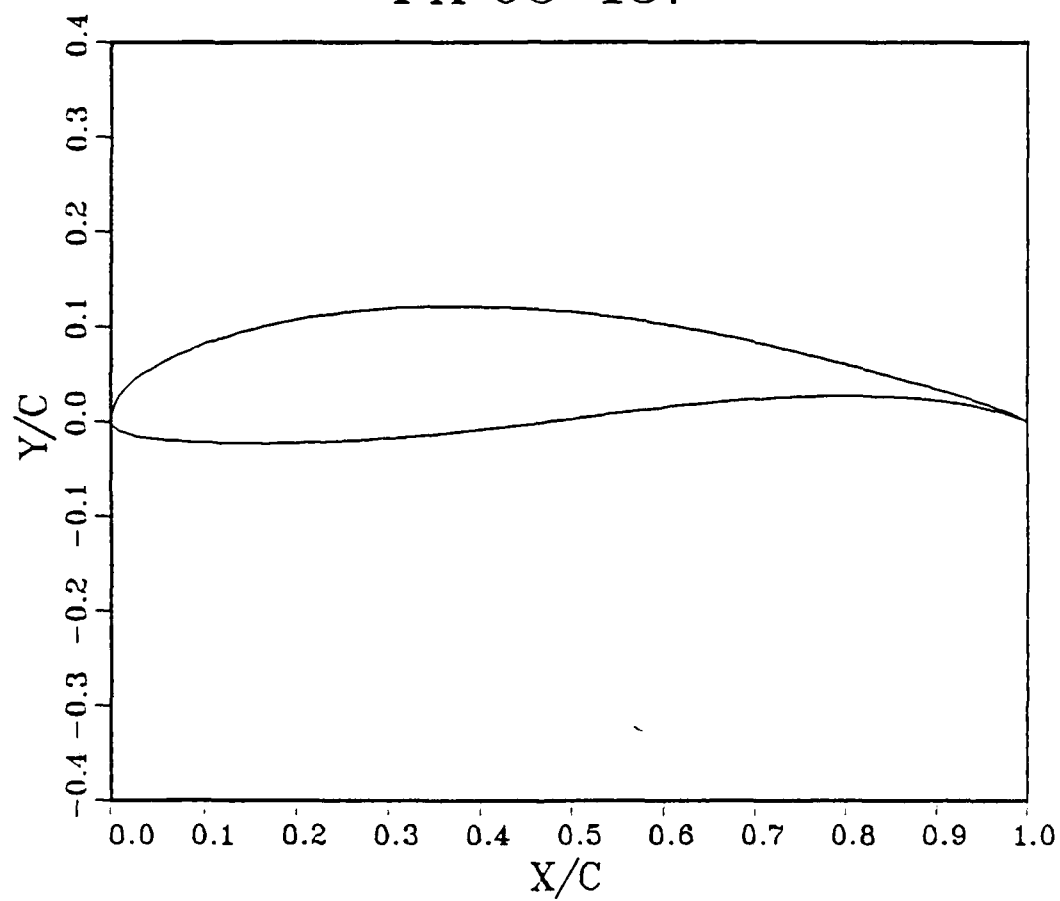
FX 63-137
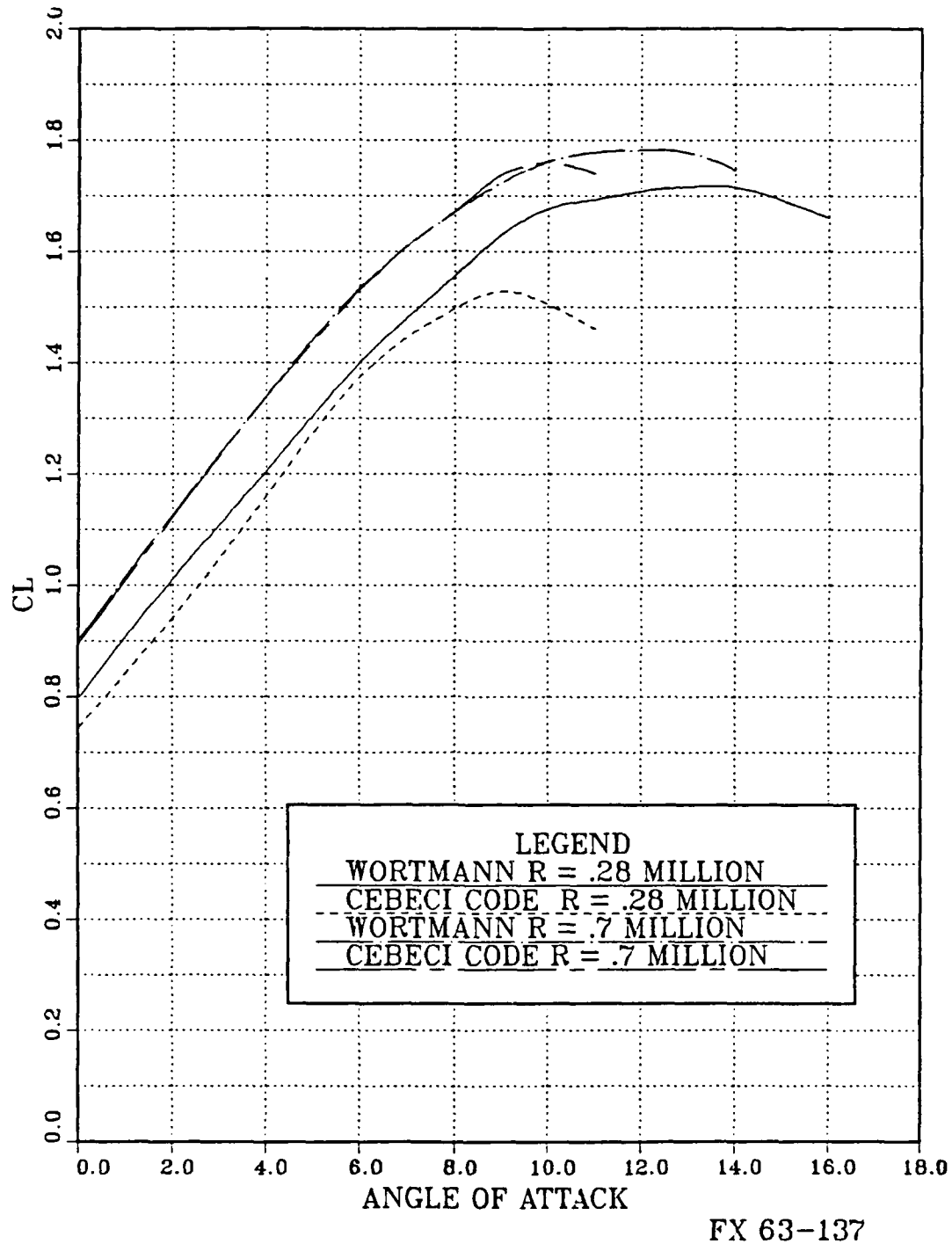

Figure 7.62   Wortmann FX 63-137

LIFT COEFFICIENT

FX 63-137

Figure 7.63   Lift Coefficient, FX 63-137, R = .28 Million, and .7 Million
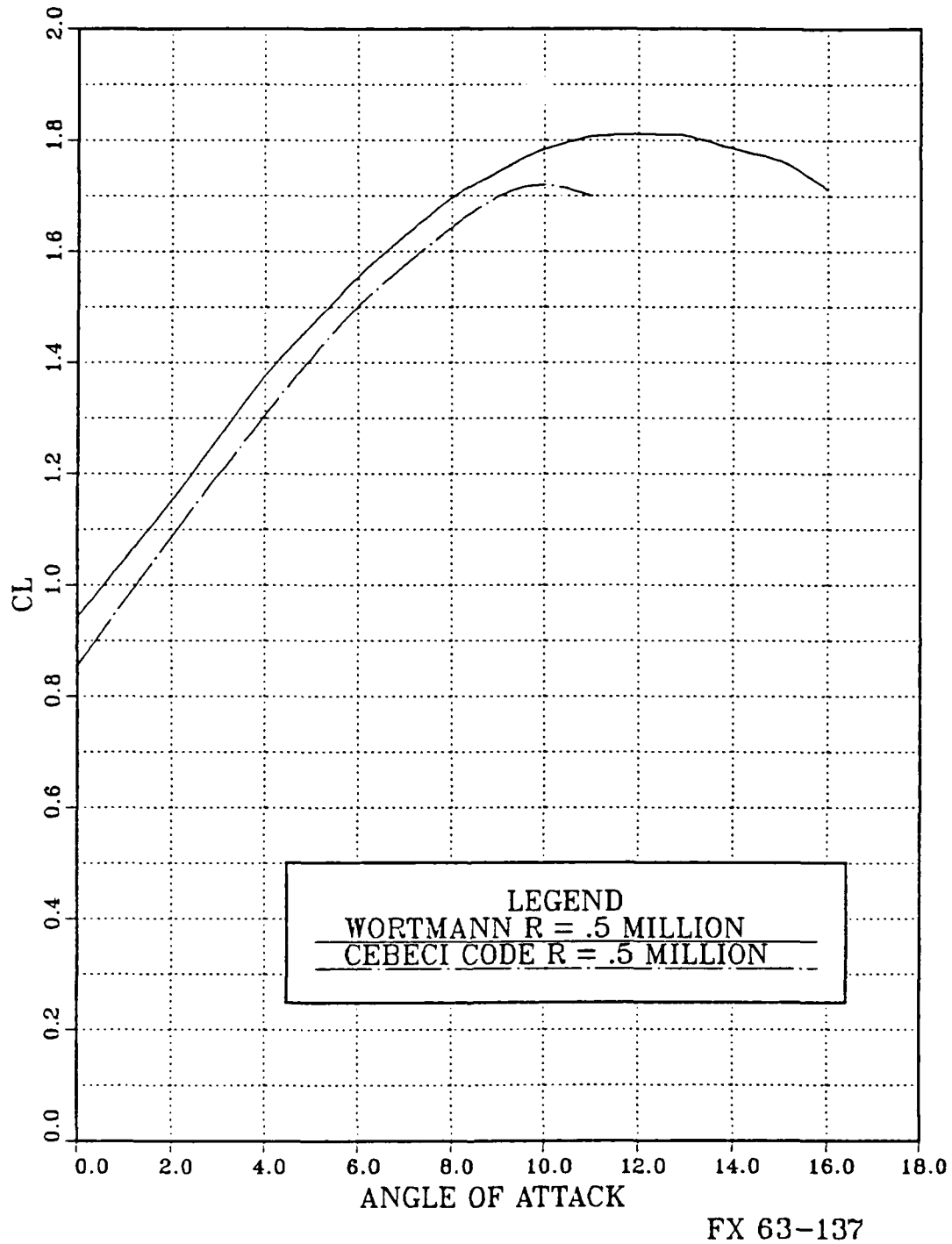
135

LIFT COEFFICIENT

FX 63-137

Figure 7.64   Lift Coefficient, FX 63-137, R = .5 Million

iterations. Figures 7.65 and 7.66 show the upper surface displacement and momentum thicknesses for steady flow and iterations of 2, 4, 6, 8 and 10. As can be seen in both figures flow calculations matched very well with experimental data up to approximately $x/C = .55$. After that point stall occurred and calculations ceased with more than 10 iterations. Brendel and Mueller experimentally derived separation to begin at $x/C = .34$, but reattachment was shown to occur at $x/c = .60$. Unfortunately the Cebeci Code could not predict reattachment for the prescribed conditions.

UPPER SUR DISPLACEMENT THICKNESS

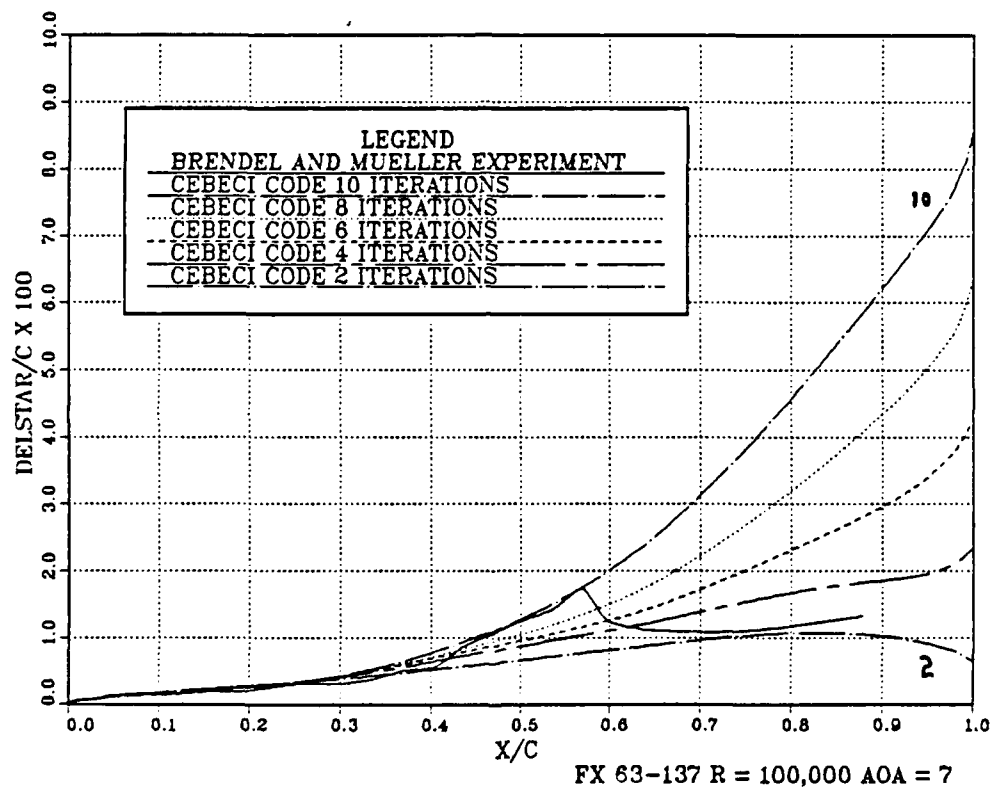
Figure 7.65   Upper Surface Displacement Thickness,
FX 63-137, AOA = 7°, R = 100,000

138

UPPER SURFACE MOMENTUM THICKNESS
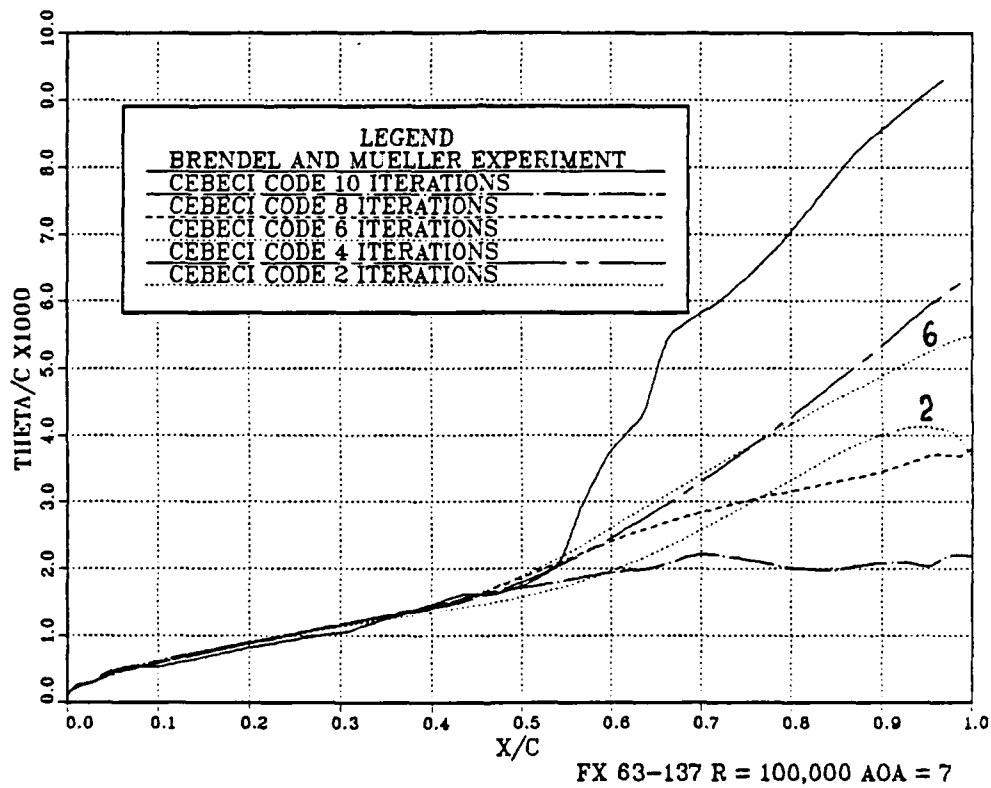

FX 63-137 R = 100,000 AOA = 7

Figure 7.66   Upper Surface Momentum Thickness, FX 63-137,
AOA = 7°, R = 100,000

139

VIII. CONCLUSIONS AND RECOMMENDATIONS

Cebeci's viscous/inviscid interaction program was applied to the analysis of steady, two dimensional, incompressible flow past four airfoils, the NACA 66_3-018, 0010 (modified), 4412 and the Wortmann FX 63-137. Detailed comparisons with the available experimental results show that for attached flows the essential features are correctly modelled, but that significant discrepancies are found in regions of flow separation. These discrepancies are possibly caused by the empirical transition modelling used in the present code. Future efforts therefore should be directed to the incorporation of transition calculations which permit the prediction of transition within a separation bubble, such as the application of the e^n-method proposed by Cebeci [Ref. 13].

LIST OF REFERENCES

1. Cebeci, T., Clark R., Chang K., Halsey N., and Lee K., "Airfoils with Separation and the Resulting Wakes," J. Fluid Mechanics., Vol. 163, pp. 323-347, 1986.

2. Zucker, R., "Aerodynamic Analysis," Naval Postgraduate School, Monterey, California, Course Notes, 1988.

3. Kuethe A., and Chow, C., Foundations of Aerodynamics, Wiley, 1976.

4. Subruto, P., Viscous/Inviscid Interaction Analysis of the Aerodynamic Performance of the NACA 65-213 Airfoil, Master's Thesis, Naval Postgraduate School, March 1987.

5. Rauscher, M., Introduction to Aeronautical Dynamics, John Wiley and Sons, Inc., 1953.

6. Krainer, A., Viscous-Inviscid Interaction Analysis of Incompressible Cascade Flows, Contractor Report, NPS-67-86-005CR, Naval Postgraduate School, Monterey, California, December 1986.

7. Lee, H., Contribution to the Analysis of High-Lift Airfoil Aerodynamics, Master's Thesis, Naval Postgraduate School, March 1986.

8. Gault, D. E., "An Experimental Investigation of Regions of Separated Laminar Flow," NACA Technical Note 3505, 1955.

9. Abbott, I., and Doenhoff A., Theory of Wing Sections, Dover Publications, Inc., 1958.

10. Hastings, R., and Williams, B., "Studies of the Flow Field Near a NACA 4412 Aerofoil at Nearly Maximum Lift," Aeronautical Journal, pp. 29-44, January 1987.

11. Brendel, M., and Mueller, T., "Boundary Layer Measurements on an Airfoil at a LOW Reynolds Number in an Oscillating Firestream," AIAA Paper 87-1332, June 1987.

12. Althaus, D., and Wortmann F., Stuttgarter Profilkatalog I, E. Hunold, Braunschweig, 1981.

13. Cebeci, T., "Essential Ingredients of a Method for Low Reynolds-Number Airfoils," to be published, California State University, Long Beach, California.

INITIAL DISTRIBUTION LIST

1. Defense Technical Information Center   2
   Cameron Station
   Alexandria, Virginia 22304-6145

2. Library, Code 0142   2
   Naval Postgraduate School
   Monterey, California 93943-5002

3. E. Roberts Wood, Chairman, Code 67   1
   Department of Aeronautics and Astronautics
   Naval Postgraduate School
   Monterey, California 93943-5000

4. M. F. Platzer, Code 67PL   10
   Department of Aeronautics and Astronautics
   Naval Postgraduate School
   Monterey, California 93943-5000

5. R. M. Howard, Code 67HO   2
   Department of Aeronautics and Astronautics
   Naval Postgraduate School
   Monterey, California 93943-5000

6. M. S. Chandrasekhara, Code 67CH   1
   Department of Aeronautics and Astronautics
   Naval Postgraduate School
   Monterey, California 93943-5000

7. S. K. Hebbar, Code 67HB   1
   Department of Aeronautics and Astronautics
   Naval Postgraduate School
   Monterey, California 93943-5000

8. John Mark Mathre   2
   421 Rolling Hills
   San Mateo, California 94403